

esa SCI(96)7

June 1996

KILOMETRIC BASELINE SPACE INTERFEROMETRY

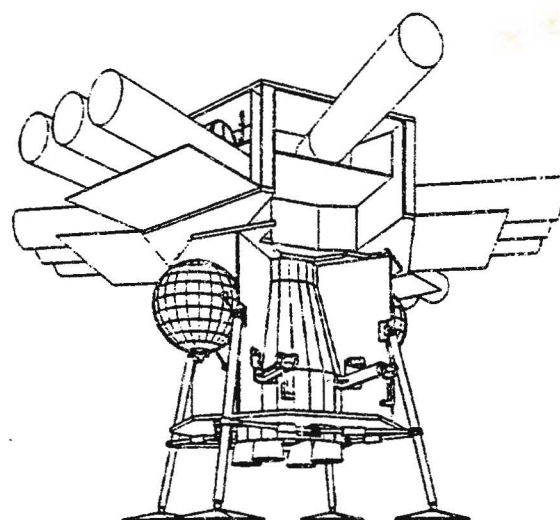
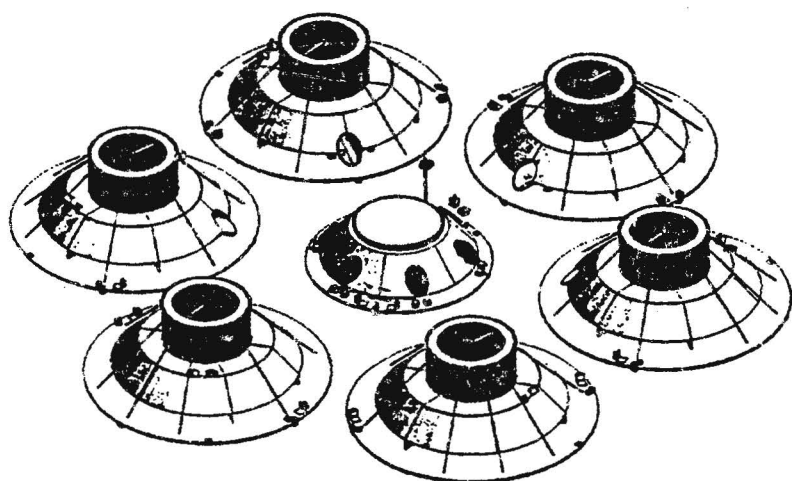
Comparison of free-flyer and moon-based versions

Report by the Space Interferometry Study Team

Pierre-Yves Bély, Robin J. Laurance, Sergio Volonte

Alan Greenaway Chris Haniff, Mario G. Lattanzi, Jean-Marie Mariotti

Jan E. Noordam, Farrokh Vakili, Oskar von der Lühé



european space agency
agence spatiale européenne

8-10 rue Mario Nikis 75738 Paris Cédex 15, France

TABLE OF CONTENTS

Foreword	1
Executive Summary	3
1. Introduction	5
2. Scientific potential	8
3. Scientific requirements	23
4. Ground vs Space	34
5. Strawman observing program	38
6. Implementation principles	41
7. Moon-based version	57
8. Free-flyer version	71
9. Comparison of the two versions	91
10. Technology development program	93
11. Conclusions	94
Appendices:	
A. Low thrust level propulsion	95
B. Parametric cost study	104
C. Exo-planet mission	106
D. Members of SWT and key MMS staff	110

FOREWORD

In its 1992 report to ESA *Mission to the Moon*, the Lunar Study Steering Group which had been established to investigate the scientific motivations to return to the moon identified optical interferometry with a baseline on the order of a kilometer as uniquely benefiting from the moon as a stable platform. In the following study phase devoted to the definition of a European view of Lunar exploration and exploitation, a dedicated group, the Interferometry Review Panel, was charged with the task of identifying the prime scientific objectives of interferometry emphasizing the rationale for Lunar-based facilities as opposed to ground based and space borne instrumentation. The moon as an astronomical platform is not without problems. The Interferometry Review Panel therefore recommended that a design study be performed to compare lunar-based and free-flying interferometers.

As a result of this recommendation ESA decided to conduct a preliminary design study of a simple two-element interferometer. This study, referred to as MOFFIT (MOon Free-Flyer Interferometer Trade-off study) was carried out from January to December 1995 under the guidance of the "Space Interferometry Study Team" with the technical work contracted out to Matra Marconi Space (MMS).

At the start of the study, the team took a fresh look at the scientific justification for kilometric interferometry, and felt strongly that the interferometer design and overall mission had to be rooted in a solid and realistic scientific observing program. This led to the conclusion that the science which could be accomplished with a two-element interferometer was very limited and that imaging was an essential capability for such a major facility. The baseline interferometer specifications were therefore modified to include additional apertures.

The present report summarizes the reflections of the Study Team and the results of the technical study performed by MMS. Technical details and supporting design documents can be found in engineering notes by MMS.

The ESA Directorate of Scientific Program staff responsible for the study were:

Pierre-Yves Bély	Study Scientist, Chairman
Robin J. Laurance	Study Manager
Sergio Volonte	Astronomy Missions Coordinator

The external experts members of the Space Interferometry Study Team were:

Alan Greenaway	Defence Research Agency (DRA), Malvern (UK)
Chris Haniff	Cavendish Laboratory, Cambridge (UK)
Mario G. Lattanzi	Osservatorio Astronomico di Torino (Italy)
Jean-Marie Mariotti	Observatoire de Paris (France)
Jan E. Noordam	National Foundation for Research in Astronomy, Dwingeloo (Netherlands)
Farrokh Vakili	Observatoire de la Côte d'Azur (France)
Oskar von der Lühse	European Southern Observatory, Garching (Germany)

The main contributors from Matra Marconi Space were Hervé Lambert, Bertrand Calvel and Ivan Lainé from Matra Marconi Space France, and Richard Scaddan, Paul Vangasse and Robert C. Parkinson from Matra Marconi Space Systems Ltd UK.

We have drawn heavily on numerous previous proposals for space interferometry and especially on the work of the preceding ESA space interferometry groups, (SIST report 1990, *Mission to the Moon* 1992, and IRP report 1994) which paved our way.

We are grateful to J. Rodriguez-Canabal, from ESA/ESOC Germany for his contribution concerning orbit selection, Nino Panagia, of the European Space Agency and Space Telescope Science Institute, for the definition of the supernova observing program, R. Morbidelli for his assistance with the reference star probability calculations, and to Sally Janda for invaluable support in the preparation of the manuscript.

We also thank Pierre Léna, Observatoire de Paris, Alain Léger from the Institut d'Astronomie Spatiale, Orsay, Steve Ridgway of Kitt Peak National Observatory, Richard Burg of the Space Telescope Science Institute, François Roddier from the University of Hawaii for their comments on the draft report.

EXECUTIVE SUMMARY

With an angular resolution 1000 times that of the Hubble Space Telescope, kilometeric baseline optical interferometry from space at visible and near infrared wavelengths has the potential to revolutionize astrophysics. In our own galaxy, interacting binaries of all types could be examined, the pulsation of Cepheids could be observed, and surface features on stars could be mapped directly. In external galaxies, beamed synchrotron jets, gas motions in broad emission line regions of quasars and active galactic nuclei in nearby galaxies could be imaged. The impact of the resulting discoveries on our understanding of physical processes in the universe could truly be extraordinary.

Most of these interesting objects have a relatively complex morphology, however, and an imaging capability is indispensable. To achieve a useful level of imaging a minimum of 6 sub-apertures is required. Some minimum subaperture size, on the order of one meter, is necessary to attain adequate sensitivity for the selected targets. This minimum telescope size is also required for operational reasons to permit the use of unresolved, and thus intrinsically faint, reference field stars for the interferometer optical pathlength control.

Some of the proposed observations could in principle be done from the ground using recently developed atmospheric turbulence compensation techniques. Indeed, a number of ground-based interferometers with baselines extending to several hundred meters already exist or are under construction. We show, however, that the sensitivity of ground-based instruments is fundamentally limited, and that moving out into space is essential.

The moon has long been regarded as a natural site for interferometry because of its supposed intrinsic stability. On the other hand, it is not without problems, since a lunar interferometer would require long delay lines and protection from the large temperature swings experienced during the lunar day/night transition. We have thus compared two versions of a kilometeric interferometer with equivalent science capabilities, one located on the moon and the other operating as a freely flying instrument. The most favorable locations for such instruments are at the equator near the limb for the moon-based version and at the 2nd Lagrange point of the sun-earth system for the free-flyer.

The study shows that the moon is not the stable space platform it is commonly thought to be, mainly because of tidal and meteoroid-induced seismic disturbances, and that both moon-based and free-flyer interferometers require essentially the same type of metrology control. Although both versions could attain the required scientific performance, the free-flyer is intrinsically advantageous because of its reconfiguration flexibility and its quasi-unlimited baseline length. Furthermore, the observational efficiency of the free-flyer is larger by a factor of approximately two, since the moon-based version cannot be operated during the lunar day because of excessive straylight.

On the logistical side, the study also shows that automatic deployment of the moon-based interferometer would be extremely difficult. Prior site preparation and man-assisted deployment appear to be essential. The lunar version would thus have to wait for a manned base, although that is not incompat-

ible with the phased approach proposed by ESA. The availability of human intervention on the moon would on the other hand permit maintenance and upgrading at the module level while in the case of the free-flyer this can only be done by replacing an entire spacecraft unit. The higher investment in a moon-based interferometer would thus result in a longer lifetime for the facility with continuous performance enhancement as a realistic possibility.

We have concluded that the free-flyer is better suited for an implementation in the near or mid-term future, but that the moon-based version should be considered in the long term in conjunction with a manned lunar infrastructure.

The study has shown the feasibility of constructing a space-based interferometer consisting of free-flying elements and the possibility of realizing such a mission with the Ariane 5 launcher in its extended version. This important result should be relevant to the preparatory studies of the IR Interferometer cornerstone candidate mission identified in the Horizon 2000 Plus program, ESA's recently proposed long term plan for Space Science.

INTRODUCTION

Higher angular resolution has always opened up new vistas in astronomy. Gains in resolution have been progressively realized by employing better and larger optics, by moving to better sites and, more recently, by compensating for atmospheric turbulence and by going into space (Figure 1.1). Diffraction-limited resolution is inversely proportional to telescope diameter, and while larger ground and space telescopes will undoubtedly be built in the future, order-of-magnitude gains in resolution must come from other techniques. Optical interferometry's ability to provide high angular resolution without relying on huge, filled-aperture telescopes has been appreciated since Fizeau (Fizeau 1868) and was demonstrated as early as 1921 by Michelson (Michelson, 1921). Drawing on many years of experience at radio wavelengths, optical interferometry has progressed rapidly in the past 20 years so that several ground-based interferometers with baselines approaching a kilometer are already working or under construction (Shao & Colavita 1992, von der L  he 1994).

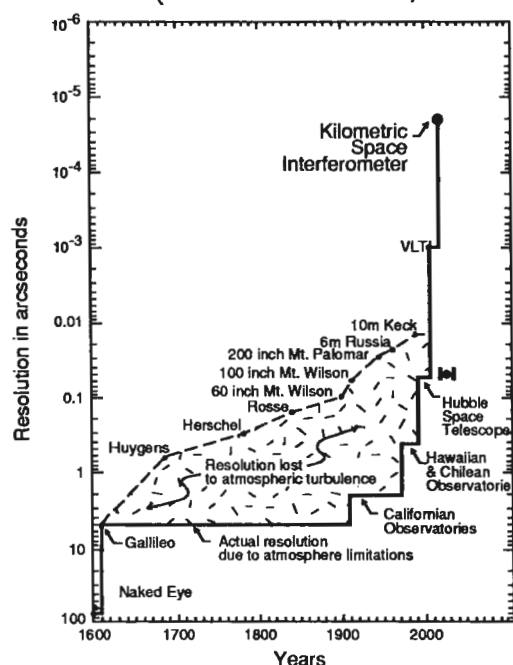


Fig. 1.1 The evolution of angular resolution in imaging optical astronomy. With a gain of three orders of magnitude beyond what can currently be achieved, kilometric baseline interferometry from space would open up an entirely new discovery space.

Optical interferometry with arrays of several separate telescopes represents the only practical way to achieve baselines in excess of a few tens of meters. These telescope arrays require sophisticated control systems in order to stabilize

the interferometric fringes and, indeed, the required technology has emerged only during the last decade or two. At present, there are several ground based multiple aperture interferometers under development and a few, like the Mt. Wilson and Calern interferometers, have already produced useful astrophysical results. Coherent combination of more than two telescopes, which is necessary for any level of imaging, has now been demonstrated and is just a year or two away from routine use (Baldwin et al 1996).

Going into space provides the same advantages for interferometry as for conventional telescopes, i.e. the elimination of the turbulent and partially opaque atmosphere. Space provides an enormous increase in resolution and sensitivity and an unlimited isoplanatic patch size. A number of connected-element space interferometers have been proposed (Traub et al 1980, Noordam et al 1987, Bély et al 1989, Nein & Morgan 1989), but their practical baseline limit is probably around 100 meters. Free-flying (separated) spacecraft have also been proposed (Labeyrie et al 1984, Stachnick et al 1984, Kulkarni et al 1994) but are widely expected to present daunting difficulties in station keeping at the wavelength scale. The moon, on the other hand, has long been considered a suitable platform for a space interferometer because it combines the advantages of space with the baseline stability conferred by firm ground (Burns 1989, Labeyrie 1992).

In order to assess the relative merits of these two approaches, i.e. a free-flying and a lunar-based interferometer, we have gone beyond a conceptual level and carried out a preliminary engineering study of these two configurations. In what follows, we present the results of this study as applied to a kilometeric baseline interferometer operating in the optical/near infrared wavelength range.

References

- Baldwin J.E., et al, *The first images from an optical aperture synthesis array: mapping of Capella with COAST at two epochs*, A. & A., Vol 306, L13-L16 (1996).
- Bély P-Y., C.J. Burrows, F. Roddier, G. Weigelt, *HARDI: High angular resolution deployable interferometer*, "New technologies for Astronomy", ECO Proc 1130, 1989.)
- Burns J., *A lunar Optical Ultraviolet-Infrared Synthesis Array (LOUISA)*, NASA Conf Publ. 3066, Burns Ed. 1989.
- Fizeau H., *Compt Rend Acad Sc* 66 p932, 1868.
- Kulkarni S.R., P-Y Bély, M. Colavita, A.B. DeCou, D.L. Jones, J.H. Krolik, C.D. Martin, H.A. McAlister, J.P. McGuire, T. Nakajima, X. Pan, S. Phinney, M. Shao, J.W. Yu, *SSI: Separated Spacecraft Interferometry*, Proposal to NASA Res. Ann. 94-15, 1994.
- Labeyrie A., B. Authier, J.L. Boit, T de Graauw, E. Kibblewhite, L. Koechlin, P. Rabout, G. Weigelt, *Trio: a kilometeric optical array controlled by solar sails*, Bull AAS, vol 16, 3, 1984.
- Labeyrie A., *Interferometry from the moon*, Targets for space-based interferometry, ESA Coll. SP-354, 1992.
- Michelson, A.A. and F.G. Pease, *Astr. J.*, 53, 249, 1921.
- Nein, M.E., S.H. Morgan, *Considerations for a Next Generation UV/Optical Space Telescope*, Next Generation Space Telescope Proc. Space Tel Sc. Inst., 1989.
- Noordam J.E., A.H Greenaway, R.S. lePoole, J.D. Bregman, *OASIS: Optical Aperture Synthesis in Space, a mission concept*, ESA Colloquium SP-273, Granada, 1987.

- Shao M. and M.M. Colavita 1992. *Annu. Rev. Astron. Astrophys.* 30, 457-498
- Stachnik R.V., K Ashlin and S. Hamilton, *SAMSI: A spacecraft array for Michelson spatial interferometry*, Bull AAS, vol 16, 3, 1984.
- Traub W.A. and H. Gursky, *Coherent optical arrays for space astronomy*, SPIE Vol 228, 1980.
- Von der L  he O., VISA – the sub-array mode of the ESO VLTI, in *VLTI: programmes astrophysiques*, INSU – CNRS Colloquium, J. Bouvier and F. Vakili (Eds.), Lyon, Oct. 1994, 20-36.

Bibliography

- Kilometric optical arrays in space, Cargese, ESA SP-226, 1984.
- Future Astronomical Observatories on the Moon, NASA Conf Publ. 2489, 1986.
- Optical Interferometry in Space, ESA SP 273, Granada, 1987.
- A lunar Optical Ultraviolet-Infrared Synthesis Array (LOUISA), NASA Conf Publ. 3066, 1989.
- Science Objectives and Architectures for Optical Interferometry in Space, Astrotech 21 Workshops, JPL D8541, 1991
- A proposed medium-term strategy for optical interferometry in space, ESA SP 1135, (SIST report), 1990
- Technologies for Optical Interferometry in Space, Astrotech 21 Workshops, JPL D8541, 1991
- Lunar Interferometry Study Team (LIST), interim report, 1993.
- Targets for space-based interferometry, ESA SP-354, 1992
- ESA Lunar Study Phase 2, Report of the Interferometry Review Panel, 1994.

SCIENTIFIC POTENTIAL

The potential of high angular resolution has long been recognized. Here we review the prime scientific targets and establish the corresponding instrumental requirements.

The sub-milliarcsecond angular resolution provided by a kilometric interferometer working in the optical domain has the potential to revolutionize astrophysics. It would provide resolutions 1000 times better than the current standard set by the Hubble Space Telescope in the optical, and 10 times better than what can be achieved by radio VLBI. At this resolution, stellar spots could be detected on nearby main sequence stars, features on the order of an astronomical unit in size could be distinguished at the center of our Galaxy, and structures as small as a few hundreds of astronomical units could be studied in nearby galaxies.

Begelman and Krolik (Begelman & Krolik 1991) have captured the importance of very high angular resolution for observations of various classes of astrophysical sources and phenomena in a classic graph, which is reproduced in Figure 2.1.

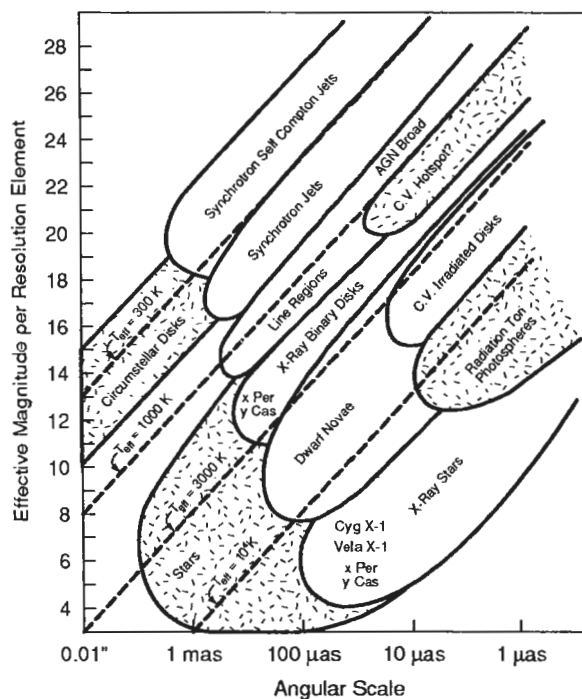


Fig. 2.1 The resolution and sensitivity required for studying several classes of astronomical objects (from Begelman & Krolik 1991). A baseline on the order of a few kilometers (100 μ arcsecond resolution in the visible) is required for the study of most of these objects.

Their figure clearly shows that the number of accessible targets increases dramatically when the resolution achievable exceeds about 1 milliarcsecond,

and the gain is maximized for resolutions in the range of 0.1 to 0.01 milliarcseconds. This is a strong impetus for adopting a maximum baseline length of a kilometer or more.

Their figure also highlights the importance of good sensitivity for high resolution imaging to be successful. Fortunately this sensitivity requirement is rather modest, less than 20th magnitude per pixel at 0.1 milliarcsecond resolution.

An implied message from their graph is that visibility amplitude measurements alone, such as can be obtained with a two element interferometer, will not be adequate. Most of the scientifically interesting and accessible targets are expected to have relatively complex morphologies, and thus a reasonable level of imaging capability will be required to ensure useful unambiguous interpretation.

Finally, two other parameters, not directly incorporated in this graph but of equal importance in defining the merit of any interferometric instrument, will be the dynamic range attainable in any map and the speed at which variable targets can be imaged. As we will see later, the dynamic ranges required for typical science programs will be in the range 10–1000. The imaging speed required will depend on the time scale of the phenomena of interest and could be as short as a day.

Aside from probing new spatial scales and, with it, new physical phenomena, kilometeric baseline interferometry offers a second path for new discoveries. Presently we are restricted to our own galaxy for a detailed understanding of many astrophysical phenomena (for example stars, supernovae, the interstellar medium, star forming regions, globular clusters). With several orders of magnitude improvement in resolution we would be able to conduct these same studies in the Magellanic Clouds. Similarly, galaxies in the nearby group would become equivalent to the Magellanic Clouds, and galaxies in Virgo equivalent to the local group (Figure 2.2).

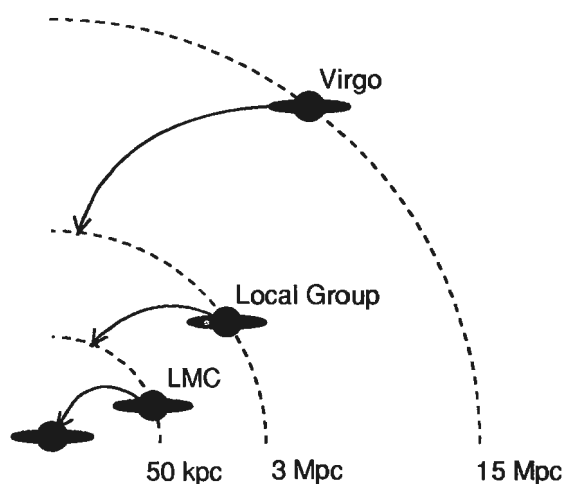


Fig. 2.2 With three orders of magnitude over the resolution currently achieved, kilometeric space interferometry would permit the comparison of statistics and physical processes in other galaxies to those that we are currently limited to. This is an essential step in verifying the universality of the phenomena we have studied so far.

Large numbers of questions asked and answered locally could thus be extended to new environments. For example, is star formation the same in Virgo galaxies as it is locally? Does binarity play the same role in the Magellanic clouds as it does in the Galaxy? History has shown that it is risky to infer general properties from the first measurements of a prototype of a class of systems. Ease of measurement does not guarantee universality. We must test knowledge

we acquire locally against conditions in more distant galaxies, and this is what a kilometric space interferometer will allow us to do.

In the following sections we discuss what might be the prime targets for a kilometric baseline space interferometer, and establish the corresponding observational requirements for each type.

2.1. Young Stellar Objects

Despite considerable research activity, both from a theoretical and an observational point of view, final elucidation of the physical status of Young Stellar Objects (YSOs) is still under debate. In particular, the canonical picture of a T Tauri star, with its dust and gas accretion disk and its highly collimated jets, has been deduced only through indirect evidence (Figure 2.3).

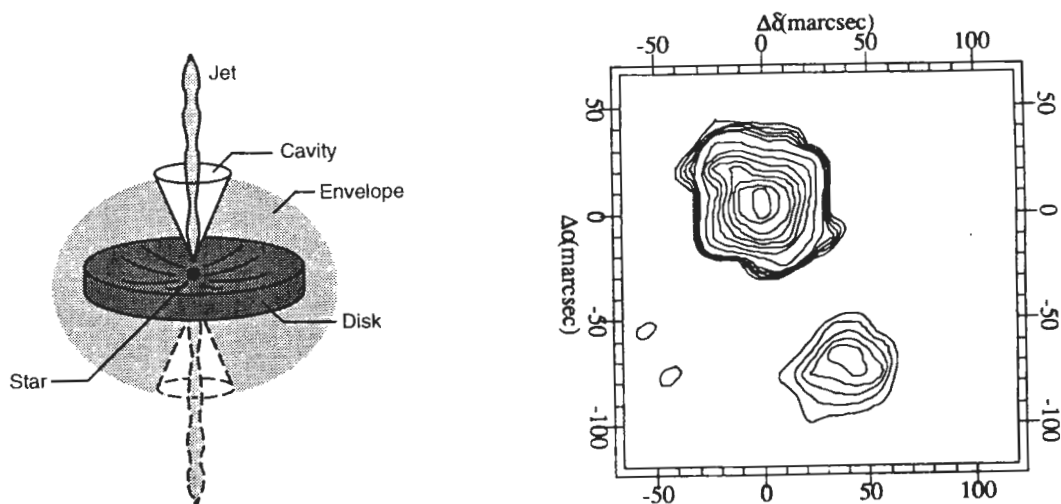


Fig. 2.3 Model of a young stellar object (left) and actual H alpha map of the T Tauri star Z CMa (right). The map which was obtained by combination of speckle-interferometry and blind deconvolution, is representative of the best imagery that can be obtained from the ground. Verifying a model such as shown at left requires sub-milliarcsecond resolution, only obtainable by kilometric baseline interferometry. The companion in Z CMa is 2.3 magnitudes fainter than the main T Tauri star, and demonstrates the crucial importance of a high dynamic range imagery. (Figures courtesy of Malbet, 1994 for the model, and Thiebaud, 1995 for Z CMa.)

Given the typical dimensions of these systems, direct detection of YSO disks and jets requires very high angular resolution, a resolution that can only be achieved by interferometry. At $2.2\ \mu\text{m}$ a 1 km interferometric array would have a resolving power of 0.5 milliarcseconds, i.e. ~ 0.07 AU at the distance of the closest concentrations of YSOs in Taurus/Auriga (150 pc). This would be sufficient to image the inner parts of the accretion disk, close to the stellar surface, as well as the base of the jets. At greater distances from the central star, voids and instabilities in the disk could be detected. Close young stellar binaries could also be resolved and monitored during their orbits, thus leading to mass estimations for their components. With a 5 km baseline, the same detailed studies could be undertaken on more distant star forming regions, such

as the Orion complex, allowing examination of the differences in star formation processed in very different physical environments.

2.2. Individual stars

2.2.1 Hot stars

Early-type stars of spectral class O, B and A have been privileged targets for ground-based interferometry (Mourard et al, 1994). However, most of them, even the brightest ones ($m_v < 4$), remain unresolved with decametric baselines and, as such, have been used as interferometric calibrators. Typically, a main sequence, $m_v = 2$, B0 star has an angular diameter on the order of 0.5 milliarcsecond, a difficult task for ground based interferometry, but well within reach of a kilometric space interferometer.

The advantages of interferometric observations from space, using a long baseline instrument are threefold. First, ground-based interferometers cannot routinely be operated at wavelengths shorter than 450 nm due to the severe limitations imposed by atmospheric turbulence. Interferometry at the wavelengths of UV spectral lines from ionized Carbon, Silicon, Oxygen and Magnesium which are characteristic of the hot polar wind of early-type stars can only be done from space.

Second, with kilometric baselines and resolutions of tenths of a milliarc-second, hot stars within 1 kpc could be resolved in the visible. A number of the closest ones, more than 20, could be imaged with a few pixels across the photospheric disk. It would become possible to directly detect non radial pulsations of high degrees ($l = |m| > 5$) which presumably modulate the surface brightness by up to 10%. Similarly, numerous other programs could be tackled including studies of local magnetic activity, star spots, differential rotation and variations in local effective temperature and gravity as a function of stellar latitude.

Finally, with such high angular resolution, it would become possible to begin examining the envelopes and shells of Be stars. These objects are surrounded by equatorial disks which extend over 50 stellar radii from the central star, i.e. between 1 to 5 milliarcseconds for the closest ones (Figure 2.4). With 0.1 milliarcsecond resolution, local inhomogeneities in the envelope, for example clumps or resonance density waves, could be detected, as could massive companions crossing the equatorial disk. This type of program demands a high dynamic range, on the order of 100:1, and an extensive imaging capability since these systems are intrinsically asymmetric.

Spectroscopy is also vital. Because of radiative transfer effects and fast rotation, the observational manifestations of early-type stars are strongly governed by kinematic effects. In this regime, velocity diagnostics, provided by the doppler effect, are very important. The required spectral resolution, however, is quite moderate, on the order of a few thousand.

2.2.2 Supermassive stars

Determination of the maximum permissible mass for stellar objects is one of the outstanding problems of star formation theory (Trimble, 1991). Masses greater than $60 M_\odot$ are predicted by theory, but this number is highly controversial and the problem is ripe for observational clarification. Many candidates for very massive stars, in excess of $100 M_\odot$, have been resolved upon closer inspection into superpositions of a number of smaller ones. As an example, high

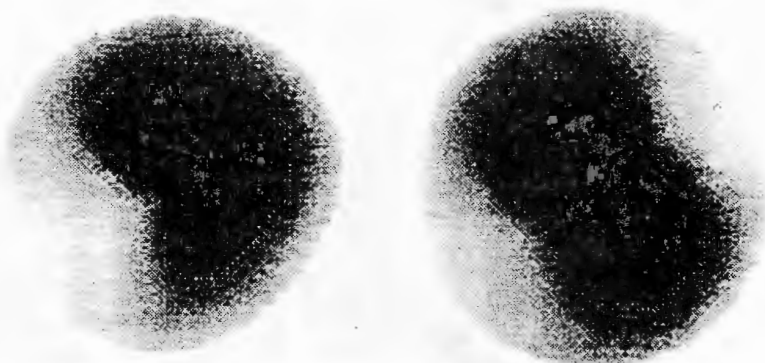


Fig. 2.4 Simulated example of interferometric Doppler imaging of a Be star envelope in the H_α emission line (γ Cassiopeia; image courtesy of P. Stec, 1995). The wavelength is 6558 Angstrom at left, and 6562 at right. A kilometer interferometer would permit the detailed analysis of the envelope.

angular resolution observations have confirmed the *binary* or *multiple* nature of one of the most massive objects of the recent past, the R136 cluster-core in the LMC (Weigelt et al 1991, Lattanzi et al 1994). The mass of R136a1 now appears to be about $60 M_\odot$, with a main sequence progenitor estimated at $80 M_\odot$ (Lattanzi et al. 1994). The remaining candidates for supermassive stars status ($M \geq 100 M_\odot$) are Melnick 42 and Kudritzki's star, both located in the LMC.

Currently, one of the best measurements in this area have been obtained with the interferometric guiding sensors on the Hubble Space Telescope which have an angular resolution of $0.''015$ at visible light. This corresponds to a linear resolution of about 1000 AU in the Magellanic Clouds. A 5 kilometer baseline space interferometer operated at visible and near infrared wavelengths would provide a resolution close to 1 AU at the distance of the LMC. Theories of binary system formation predict an essentially flat distribution of component separation from fractions of an AU up to several hundreds of AUs. A kilometer baseline interferometer would thus be pivotal in closing the current gap in parameter space between the regions probed by spectroscopy and by ground based interferometry.

2.2.3 Main sequence stars

One important area of research highlighted by ground based interferometrists is the measurement of main sequence stellar radii and hence the determination of effective temperatures. This fundamental program has, however, only been targeted by a single ground-based instrument (SUSI). This is primarily because very long baselines are required (at least 1 km) to assure satisfactory sampling of all main sequence types. A kilometer array in space offers the possibility of both far higher precision and the observation of a significantly larger sample of stars by virtue of the enhanced resolution, but also thanks to much improved sensitivity.

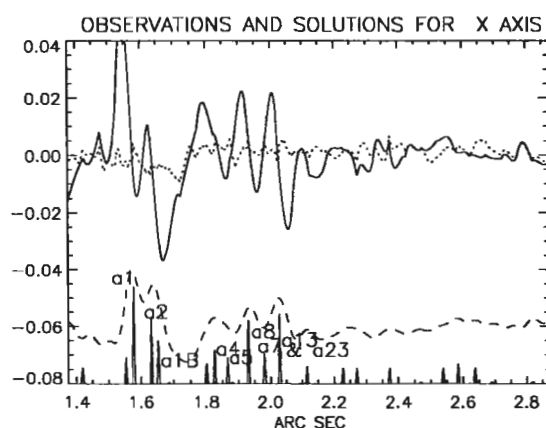


Fig. 2.5 Normalized visibility fringe trace (thick curve) of R136a obtained with the X-axis interferometric guiding sensor on the Hubble Space Telescope (Lattanzi et al. 1994). The dotted line is the curve of the residuals, the dashed line is the profile generated from the deconvolution of the visibility curve. The position and relative amplitude of the spikes on the abscissa represent the individual stellar components as derived from a direct signal reconstruction technique. The height of the spikes is proportional to the relative brightness of the components. Only the sharpest features are identified.

2.2.4 Surface Activity of Giants

Stellar surfaces show a wealth of phenomena which are important for the general understanding of the hydrodynamics of magnetized plasmas. The scales of these processes cover the range from the size of the star over the pressure scale height and the mean free path of the photons in the photosphere (of order 10^6 meter) to the inner scale of turbulence which is determined by the viscosity of the plasma (of order centimeter). Observing these processes with an interferometer will require very long baselines.

Figure 2.6 shows the contributors to the fringe visibility magnitude for a relatively quiet solar-type star and for an active giant (von der Lühe, Solanki & Reinheimer, 1995). The contributors to the visibility signal are the sharp edge of the stellar disk, sunspots and active regions, and convective surface phenomena such as solar granulation. The baselines required for observing activity signatures are on the order of hundreds of meters and therefore already a target for a ground-based interferometer. A kilometric space interferometer would contribute by mapping a larger sample of stars or by resolving less frequent (and therefore more distant) peculiar stars. Surface convection can probably be successfully observed only with a kilometric array. The observing program would concentrate on statistical properties of convection, such as mean size and shape of granules, and therefore only require visibility magnitude information for a few baselines.

Surface activity observed with an interferometer can reveal crucial information on the processes which generate magnetic fields in the interior of cool giants (von der Lühe, Schüssler, Solanki & Caligari 1994). The generation of magnetic fields by dynamos is a fundamental astrophysical process which influences the structure and physical characteristics of many objects such as stars, accretion disks, and even galaxies. However, the underlying magneto-

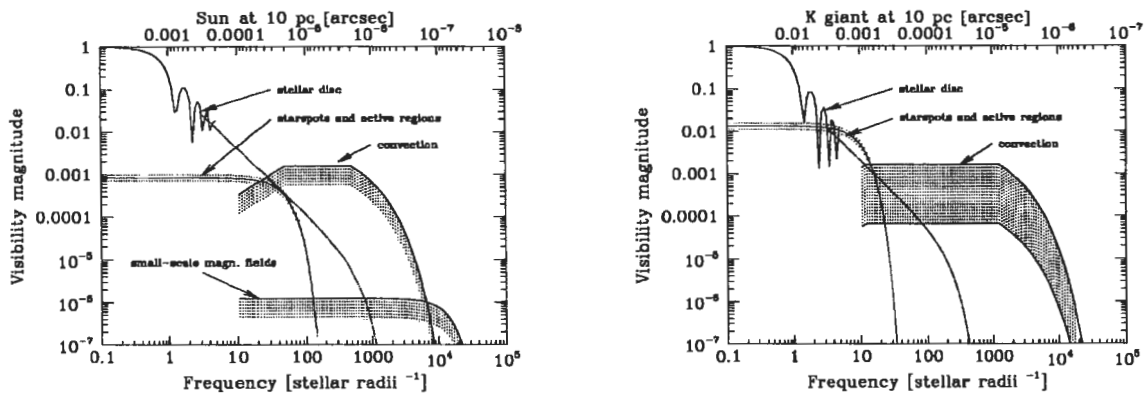


Fig. 2.6 Contribution to the visibility magnitude of stellar surface phenomena for solar-type stars (left) and magnetically active stars (right) as a function of angular frequency. The contributions include the sharp edge of the stellar disc, stellar granulation (convection), and magnetic phenomena such as star spots and flux tubes. The scale on the top shows the corresponding angular scale for the star seen from 10 pc distance.

hydrodynamic mechanisms are still not well understood. Investigations of the dynamics of magnetic structures on stellar surfaces provide crucial insight because they form the connection between observable surface fields and generally observationally inaccessible dynamo regions within or below the outer convection zones of cool stars.

2.2.5 Cepheids

Cepheid variables are the most reliable primary distance indicators, and are of crucial importance for the measurement of both galactic and extragalactic distance scales. Some 50 Cepheids lie within 1 kpc but the distance of only a few of them were measured astrometrically by Hipparcos. The distance of Cepheids is generally inferred from the Period-Luminosity or Period-Luminosity-Color relationships. Direct measurements of changes in the angular radius of a Cepheid combined with radial velocity measurements from spectroscopic observations would lead to a more reliable distance determination. Expected variations of angular radii of local Cepheids (≤ 1 kpc) is in the range of 10 to 100 μ arcsec and need to be measured with accuracies better than a few percent. This is well within the capabilities of a kilometric space interferometer.

Although the pulsation mechanism of Cepheids is thought to be well understood, theories of stellar evolution and pulsation disagree significantly on the mass estimates for these stars. The best determination of Cepheid masses will be obtained from the orbits of Cepheid binaries, which will become possible with kilometric interferometry. Interferometric observations could also resolve controversies relating to the cluster membership of certain Cepheids, where radial velocity and ZAMS fitting have given inconsistent distance estimates.

2.2.6 Cool evolved stars

Despite much theoretical work, detailed knowledge of the fundamental processes governing the behavior of cool evolved giants and supergiants is still relatively poor. In particular, physical models for mass loss, convection, stellar pulsation and even the radial stratification of diffuse stellar atmospheres have

yet to be tested against observational data. Although some progress has been made in these areas using interferometric techniques on single large telescopes, the limited resolutions (~ 20 mas) available with single aperture telescopes means that only a small number of the closest such prototypes can be usefully studied. A kilometric array with resolutions at the sub-mas level would permit exploration of all of these objects out to a distance of 1000pc, thereby permitting statistical studies to be undertaken for the first time.

With an imaging capability providing maps of at least 10×10 pixels and with spectral resolutions in the range 100–1000, numerous problems could be addressed. These would include detection of surface features, the precise measurement of their sizes, multiplicities and temperatures, and the definition of their characteristic evolution timescales. The relationship between surface asymmetries and the extensive mass loss seen in evolved giants is as yet unclear. Milliarcsecond imaging at near infrared wavelengths would provide the first detailed look at hot dust close to the stellar surface where grain condensation and acceleration presumably takes place, while observations at longer wavelengths would probe the larger circumstellar envelope structure and its properties.

Another scientific program could be to measure and monitor changes in the wavelength-dependent diameters of these stars, in particular for the Long Period or Semi-Regular variables. Current models place only weak constraints on the magnitude of these size variations, though they are likely to be in the milliarcsecond range. Powerful tests of these dynamical theories will come from spectrally resolved images which will isolate different layers in the stellar atmosphere, and which offer the possibility of directly monitoring the propagating shock fronts in the stellar atmosphere.

2.2.7 Supernovae

Supernovae (SN) represent the explosive death of low mass (type Ia) and moderate and massive stars (types Ib/c and II). In all cases, the explosion injects highly metal-enriched material (at least $1 M_{\odot}$) and a conspicuous amount of kinetic energy (about 10^{51} ergs) into the surrounding medium. Supernovae explosions are thus crucial events that determine many aspects of galaxy evolution, i.e. most of the visible Universe. This is why a large effort is being devoted to the study of supernovae and their related phenomena (Panagia, 1986,1996).

Unfortunately SN explosions are relatively rare events with only a few occurring in the Galaxy per century, and so most of them are observed in relatively distant galaxies. Since supernovae are bright objects (e.g. at the Virgo cluster an SNIa is around 12th magnitude at maximum light and an SNII about 14th or brighter) photometry and spectroscopy have provided us with a wealth of valuable information about the time evolution of the emission and about the stratification of the chemical abundances. On the other hand, direct information about spatial structure is lacking because, even with expansion velocities of several thousand kilometers per second, their apparent size typically remains below 1 milliarcsecond and so cannot be studied with ordinary techniques at optical wavelengths. The only supernova for which expansion has been studied is SN 1987A, and this only because of the proximity of the LMC and the availability of the HST (Figure 2.7). Radio VLBI experiments which can reach resolutions of 1 milliarcsecond or better have been able to study the expansion of a handful of SNe (e.g. 1979C, 1986J, 1993J), but since the radio emission arises from the interaction of the SN shock front with circumstellar material, radio observations typically tell us more about the nature of the SN circumstellar environment than about the supernova itself.

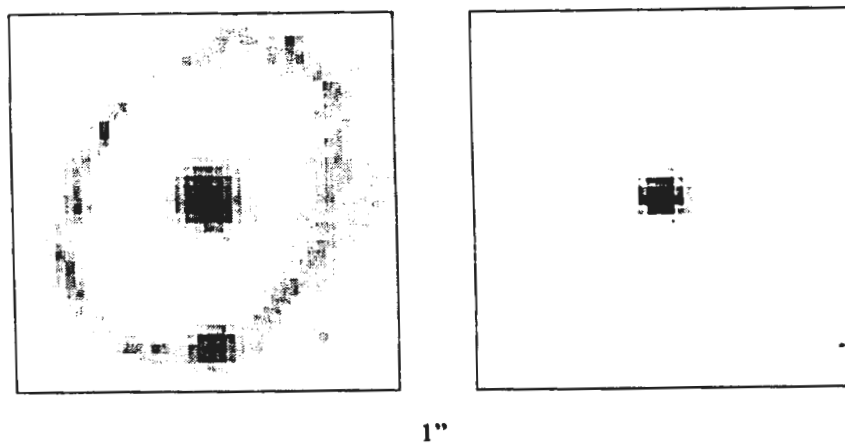


Fig. 2.7 An image of SN 1987A and its circumstellar ring obtained in January 1995 with the PC chip of the HST-WFPC2 in the V filter (left hand frame). The pixel size is $0.048''$. The supernova appears extended, with a FWHM diameter of about $0.3''$, whereas both the 20th magnitude star projected on the ring and the comparison star displayed in the right hand frame (same total flux as SN 1987A) are unresolved (FWHM $< 0.09''$).

The importance of studying the spatial structure of supernovae resides in the fact that they offer a unique opportunity of investigating the nature of the explosion and, by following their structural evolution, of clarifying the complex mechanisms that govern the later evolution of the expansion.

In the first few weeks after an SN event the atmosphere of a supernova will be expanding at a velocity of about $10,000 \text{ km/s}$ and, therefore, at the time of maximum light will have attained an absolute size of approximately 100 AU. A year later the atmosphere will be roughly 1000 AU in size and about 3-5 magnitudes fainter. Thus, at the distance of the Virgo cluster we would expect an SN to appear at 13 ± 1 magnitude at maximum light and to have an apparent size of 6 micro-arcsecs, whereas a year later its size would be around 60 micro-arcsecs and its magnitude about 17th. We note that the flux decay in the infrared would be considerably slower because both cooling of the gas and dust condensation in the ejecta tend to shift the peak of the SN emission from the optical to the infrared.

SN expansions are ideal targets for a kilometric optical/near-infrared interferometer. Observationally, their size is well matched to the interferometric resolution and scientifically, the study of their structure will uniquely clarify the fundamental problem of the chemical and dynamical evolution of galaxies.

Since SN expansions could be followed interferometrically for at least a year and the absolute expansion velocity of the SN atmosphere can be accurately measured via spectroscopy, the interferometric study of an SN expansion would also provide geometric distance estimates accurate to better than 10%.

It is of interest to note that every year approximately 2 SN explosions are discovered in the Virgo cluster alone. With a total collecting area of several square meters, interferometric imaging could be performed on targets at distances up to 3 times greater, so that the number of SN events would be in the range of 20 to 60 per year. This would permit excellent flexibility in any observing program, although satisfactory resolution of these more distant events would only be achieved several months after the explosion itself.

2.3. Exo-Planets

Infrared detection and spectroscopy of terrestrial exo-planets can only be achieved from space, but probably not from the Moon. The issue here is not really the angular resolution – only baselines of tens of meters are needed – but the high sensitivity required. Earth-like planets are best detected and analyzed spectroscopically between 10 and 16 microns. In that wavelength range, observations from the ground are not possible, but even from space where instrumental thermal emission can be eliminated by cooling the optics to about 60 K, observations are very difficult because of the strong zodiacal light background. Detection requires either very large apertures at 1 AU from the sun or placing the interferometer at least 3 astronomical units from the sun where the zodiacal background is reduced by 2 orders of magnitude.

Because of the large apertures that would be required on the moon (8 meter diameter), the distant orbit required for the free-flyer version ($> 3AU$), and the need for a special array configuration and instrumentation, such a program would deviate too much from the frame of our comparative study and we did not include it in our strawman program. However, it appears that the free-flyer scheme would offer a very advantageous solution for this exciting program and we briefly explore this possibility in Appendix C.

2.4. Gravitational lensing of stars

Gravitational lensing of background objects by galactic stars has raised considerable interest since the first positive detections of such events in the direction of the Large Magellanic Cloud and, more recently the Galactic bulge. Several continuous surveys are now monitoring these events, for which the rate of discovery is now estimated at several tens per year. These photometric surveys are able to measure only two quantities per event, namely its duration and maximum amplification, while the problem is determined by three unknowns, the distance of the deflector, its mass, and the impact parameter. As a consequence, photometric data can only provide statistical results. In the general case, the image of the background object is split into two images by the lensing phenomenon. At maximum amplification, the distance between these two images is approximately equal to the so-called Einstein radius. For a 0.1 solar mass star lensing an LMC background star, the angular size of the Einstein radius is about 2 milliarcseconds at a distance of about 200 pc from the sun. In practice the impact parameter is derived from the measurement of the relative motion of the two images of the lensed star. Separation of the two components and measurement of their relative brightness is thus well within the capability of a kilometric interferometer, the only condition being that the interferometer be pointed at the event on rather short notice, within a few days after the photometric alert. By following the evolution of the splitting of the lensed images, one can easily derive the impact parameter, yielding a complete solution for the fitting of the event and the mass of the deflector. This would be extremely valuable since, by nature, such an event is unique for a given star. The full characterization of such proper motion (i.e. the derivation of its modulus and direction) would, however, require the availability of two reference stars. Lensing of a background bulge star is an even more interesting case since these observations could permit the detection of very low mass objects close to the main deflector, e.g., exo-planets. Estimations show that if all the lensing stars have planetary systems similar to ours, the probability of detecting exo-Jupiters could be as high as 20% per event. The Einstein radius associated

with a 0.001 solar mass planet would be 32 solar radii which translates into 25 micro-arcseconds at 6 kiloparsecs. The event could thus be resolved using a 5 kilometer baseline, and provide a direct estimate of the planet mass. We note however that the operational requirements are very severe since in this case the event lasts only a few hours. The observations should be attempted at visible wavelengths to benefit from maximum angular resolution.

2.5. Interacting binaries

Binary stars or multiple systems can be found throughout the whole HR diagram. Often they appear as hierarchical structures comprising widely spaced pairs whose components are themselves multiple, though on much smaller scales. In favorable circumstances (i.e. when the systems are double-lined spectroscopic binaries), long baseline interferometry would permit a complete determination of the component masses and distances. The direct measurement of fundamental stellar parameters such as masses, radii and luminosities would provide a unique testing ground for theories of stellar formation and evolution. For other systems, in which only a single component can be detected spectroscopically, it should still be possible to derive useful estimates of stellar masses. This is especially important for OB stars where the bright primary generally masks the emission lines from the fainter secondary.

2.5.1 Algol-type binaries

Among interacting binaries, Algol-type systems involving mass transfer from a sub-giant onto a main-sequence dwarf represent the most quiescent category. Despite this they are still expected to exhibit moderate mass flow and an excited gas stream from the more evolved to the main-sequence companion. The Algol system itself would be resolvable at the milliarcsecond level, so that with kilometric baselines one could begin to investigate properties such as mass loss, dynamical evolution and accretion in at least a small sample of targets. The typical orbital timescale for these systems is on the order of a few days. Rapid reconfiguration of the interferometric array is thus essential, indicating that these objects may not be observable by a moon-based interferometer which relies on lunar rotation for image synthesis.

2.5.2 Accretion and related phenomena in close binaries

From an astrophysical standpoint, multiple systems involving compact companions represent an exciting challenge for interferometric observations. In these systems mass flow via Roche lobe overflow is more vigorous, resulting in the formation of an accretion disk where infalling material can slowly release its angular momentum and eventually sink into the potential well of the compact companion. Systems with white dwarf components, so called cataclysmic variables, offer the best opportunity for identifying the accretion disk itself. Here the optical emission from the system is dominated by the disk and the hot spot where the accretion flow impinges on the disk.

These objects can only be imaged with a space-based interferometer. Interferometers on the ground cannot be sensitive enough nor sufficiently large to provide useful data. With 50 μ arcsec resolution a number of the nearer accretion binaries should be resolvable. Measurements of the orbital motion which, as mentioned above, can lead to mass estimates for the component stars would be particularly useful in terms of assessing theories of stellar collapse. More exotic phenomena, for example tidal distortion, apsidal rotation and mass

exchange, will undoubtedly be present, but direct measurement of these may have to wait for even larger arrays.

2.6. Galactic center

The galactic center is a prime target for long baseline space interferometry using differential astrometry. Within a few months the orbital motions of the group of stars closest to the Galactic Center could be ascertained, thus allowing direct measurement of the mass of the central core.

2.7. Active Galactic Nuclei

Active galactic nuclei require a sub-milliarcsecond resolution for studies of regions close to the core of the active region. At a distance of 10 Mpc a resolution of 0.5 milliarcsecond translates into 0.02 pc, or about one light-month. Although the central engine will remain unresolved at this scale, its immediate surrounding (the broad and narrow line regions and the regions of hottest dust) could be studied in details. It is likely that the optimal observing wavelengths would be in the infrared where extinction is lowest.

2.8. Gravitational waves

Recent results (Fakir 1995, Makarov 1995) have shown that gravitational pulses (waves) generated by special classes of close binary stars would result in the perturbation of the angular distance between a gravitational wave source and an angularly close background star. With a maximum baseline of 5 km and a metrology control system capable of ~ 5 nm accuracy, a kilometric space interferometer would have an astrometric angular accuracy of $\sim 0.2 \mu\text{arcsec}$. Figure 2.8 shows the detectability potential of such an instrument for periodic gravitational wave sources. Gravitational wave “wobbling” could be followed down to a time resolution on the order of 1 second depending on the apparent magnitude of gravitational waves source and background star.

Among candidate targets known to date, V Pup appears to be just above the detection threshold of a kilometric interferometer. Target availability may thus be the limitation to the practical application of astrometric gravitational waves detection. However, the gravitational effect employed by the technique is proportional to the impact parameter, i.e. the angular distance between the light source and the source of gravitational waves. In the case of binary stars made of two neutron stars an effect at the $0.1\text{--}1 \mu\text{arcsec}$ level requires impact parameters of the order of $\sim 8 \times 10^{-5}$ arcsec or smaller at 1 kpc. Eclipsing triples made of neutron-neutron binaries and a third component as the light source could thus be ideal candidates. No such eclipsing variables are known to date, but their discovery by ground based means or space astrometry survey missions such as GAIA (Lindegren and Perryman 1995) would permit a kilometric space interferometer to bring a decisive solution to one of the most intriguing predictions of General Relativity still defying experimental proof.

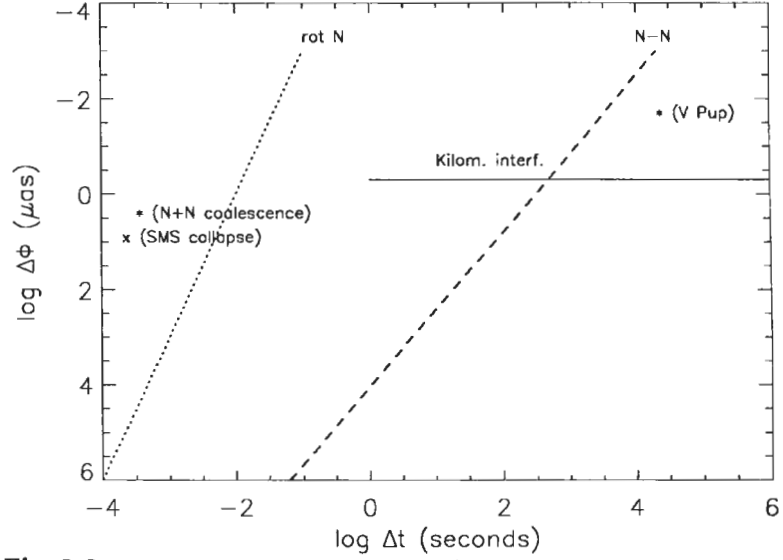


Fig. 2.8 This figure, adapted from Makarov (Makarov 1995) plots the angular resolution versus the time scales of various gravitational waves events. Fast events ($\Delta t < 1$ s) like rotating neutron stars of different degree of asymmetry represented by the dotted line marked 'rot N', are clearly beyond an imaging interferometer time resolution capability. Coalescence of two neutron stars (the asterisk marked 'N+N'), and the collapse of supermassive stars (the x marked 'SMS Collapse') are also too fast. But for time scales $\Delta t \geq 1$ s, a space kilometeric interferometer would cover a large portion of the dashed line which represents the location of binaries made of two one- M_{\odot} neutron stars of different periods (the upper limit of the astrometric accuracy of a kilometeric interferometer is shown by the horizontal solid line).

2.9. Astrometry

Direct measurement of absolute parallax and proper motion needs *global* astrometry which is not possible with the type of interferometer studied here. Global astrometry can only be accomplished with a very large field or a multiple line-of-sight system and requires a very specific design. Improvements in this domain which, as the Hipparcos mission has beautifully demonstrated, is best studied from space, will have to wait for the implementation of concepts like GAIA.

On the other hand the interferometer concept studied here would be capable of extraordinary high precision *narrow field* astrometry. Although limited in scope, narrow field astrometry permits the determination of relative parallax and proper motions for a wide range of objects. With a 5 km baseline and proper metrology, the optical path length difference between the target and the surrounding reference stars to $\lambda/100$ at 500nm, the *astrometric* angle β between the reference stars and the target could be measured at the 0.2 μ arcsec level. This has the potential to provide parallaxes accurate to within 1% at the distance of the Magellanic Clouds (~ 50 kpc) and to within 10% at distances of 500 kpc! With this level of accuracy and a limiting magnitude of 18, the parallax of all Cepheids in our galaxy could be determined. With a limiting magnitude of $V \simeq 20$, internal dynamics in the Magellanic clouds, M31 and other local group galaxies could be studied, and the relative motion in quasar pairs and proper motion of most galactic and globular cluster could be observed.

Besides the direct (geometric) parallax technique just described, there

is another model-independent way of measuring astronomical distances, i.e., through a combination of spectroscopic (photometric) and astrometric orbital data of resolved binary stars (*orbital parallaxes*).

Direct (astrometric) parallaxes, are limited by the availability of faint background stars "bright" enough to be suitable also as reference stars. In this respect, orbital parallaxes are the natural complement of the direct method, for, long baseline interferometers can resolve very close binary systems up to considerable distances, and therefore contribute to the derivation of accurate orbital parallaxes. With a space-borne interferometer the measurable distances could be extended by three orders of magnitude to the distance of M31 (> 500 Kpc). Thus, the calibration of the first, crucial, rungs of the cosmic distance scale would be done directly, with no need to resort to indirect methods like main sequence fitting of clusters HR diagrams. A Capella-like binary with two G-type giants located in the Magellanic Clouds would have a V magnitude of about +19.0, well within the reach of the space interferometer. At a distance of 50 kpc, a 1 km baseline would be capable of resolving this binary as long as its period is no shorter than 1.8 years. For M31, at a distance modulus of $\sim +24$, sufficiently luminous binaries with appropriately long periods (corresponding to orbital semi-major axis of 10-15 AU) could be resolved, and an orbital parallax of about $2 \mu\text{arcsec}$ (the distance to M31), with a precision of 10%, would be within reach. Naturally, the long periods required to resolve the most distant binaries add a requirement on the minimum mission duration for the free-flyer option.

References

- Begelman & Krolik, Workshop Proceedings: Science objectives and Architectures for Optical Interferometry in Space, pp17, Pasadena, CA, 1991.
- Bouvier J. 1994. ASP. Conf. Ser. 64, 151
- Donati J.F. et al. 1992. A&A 265, 682
- Evans N.R. and R.W. Lyons 1994. AJ 107, 2164
- Fakir, R. 1995, ESA-SP 379, p.113
- Gieren W.P. et al. 1994. AJ 107, 2093
- Jacoby G.H. et al. 1992. PASP 678, 599
- Lattanzi, M.G. et al. 1994, ApJ, 427, L21
- Lefevre E. et al. 1994. A&A 283, 483
- Lindgren and Perryman, GAIA, ESA SP 379, 23, 1995
- MacAlister H.A., in High Angular Stellar Interferometry, eds. J. Davis and W. Tango, 3-1.
- Makarov, V.V. 1995, ESA-SP 379, p.117
- Malbet, F, *Disques circumstellaires autour des étoiles jeunes*, Programmes astrophysiques pour le VLTI, PNHRAA, ENS Lyon, J. Bouvier and F. Vakili Ed, 1994.
- Mennesson B. and J.M. Mariotti, *Array Configurations for a Space Infrared Nulling Interferometer dedicated to the Search for Earthlike Extrasolar Planets*, to be submitted, 1996.
- Mourard D. et al., proceedings of IAU Colloq. 135, ASP Conf. Series, McAlister & Hartkopf eds. and Vakili et al., proceedings of IAU Sympos. 162, 1994, Kluwer Academic Publishers, Eds. Balona et al.
- Pan X.P., M. Shao, and M.M. Colavita 1993. IAU Symp. 158, Eds. J.G. Robertson & W.J. Tango, 413

- Panagia N., "Observations of Supernovae", 1986, NATO ASI on "High Energy Phenomena in Collapsed Objects", 1987, F. Pacini ed., D. Reidel (Dordrecht-Holland), p. 33-49.
- Panagia N., "Supernovae", 1996, Invited Review Talk at the XXIV International Cosmic Ray Conference, Rome (Italy), August 28 - September 8, 1995, *Nuovo Cimento*, February 1996, in press.
- Pier and J. Krolik, *Ap J* 418:673, 1993
- Rodono M. 1992. *IAU Symp.* 151, 71
- Shu F.H. et al. 1990. *ApJ* 358, 495
- Stee P. 1995 *A&A*.
- Thiebaut, 1995, *JOSA*, A 12,3
- Trimble, V. 1991, *PASP*, 104, 1
- von der Lühe, O., Suchsüssler, M., Solanki, S., Caligari, P. (1994) "Observation of Surface Activity on Cool Giants with the VLT Interferometer," in J. Walsh & J. Danziger (Eds.) *Science with the VLT*, Springer 1995, pp. 94-99.
- von der Lühe, O., Solanki, S., Reinheimer, Th. (1995) "Observing stellar surface structure with the ESO VLT Interferometer" in *Proc. of the IAU Symposium 176, Stellar Surface Structure*, K. G. Strassmeier (Ed.), in press.
- Weigelt et al. 1991, *ApJ*, 378, L22

SCIENTIFIC REQUIREMENTS

Most of the prime targets for high angular resolution observations have complex morphologies which require imaging capability, a large dynamic range, and adequate sensitivity. Since the associated phenomena are often variable on relatively short time scales, the time needed to synthesize an image is a factor. We summarize here the performance that would be expected from a major kilometeric space interferometric facility.

Having reviewed which targets are prime candidates for high angular resolution and delineated the performance which can be expected from ground based observatories, we now establish the general capabilities that a space instrument should have.

3.1. Spatial resolution

The detailed analysis of the prime targets made in the previous chapter confirms what the Begelman and Krolik graph suggested, namely that there is a strong threshold in performance requirement at about 1 milliarcsecond. Indeed, except for the very specific exo-planet search and imaging of globular cluster cores, most programs would not be successful unless the resolution is 10 to 100 times better than that (0.1 to 0.01 milliarcsecond). Assuming one works in the visible, this implies the use of baselines of up to 5 km.

3.2. Imaging

Although a few of the scientific programs outlined in the previous chapter can be addressed with a simple two-element interferometer, the majority of them require some sort of imaging capability. The themes of accretion, in- and outflow, pulsation, and surface phenomena that underlie many of the most exciting programs are all expected to exhibit some degree of asymmetry. The ability to image, and hence dispense with the usual assumptions of circular and axial symmetry, will be one of the most powerful aspects of an imaging interferometer.

Satisfactory interferometric imaging is obtained when the spatial frequencies of the source are well sampled all the way to the resolution limit. This condition implies that the number of fringe visibility measurements made with various baselines must be sufficient or, expressed in the spatial frequency domain, that the Fourier plane (also referred to as uv -plane after the commonly used coordinates u and v) is well "covered".

The number of visibility measurements depends on the number of array elements, on how many array reconfigurations will be used and, in the case of the moon, on how many exposures will be taken during the lunar day to benefit from the lunar rotation source/array geometry changes. Because of cost and launch constraints, the number of individual apertures of a space

interferometer is necessarily limited, and it was not obvious that an entry level interferometer could be at all useful. Although this issue has been well studied for radio arrays, the sources and array parameters are different than at radio wavelengths. We therefore performed imaging simulations directed towards some of the specific targets identified in the previous chapter to explore the imaging quality obtainable with a small number of array elements.

We used 3 source models: a resolved stellar disk with a small number of dark spots on the surface, a cluster of unresolved stellar objects, and a cluster of resolved overlapping Gaussians emulating a more complex source distribution. Three array geometries were studied: a 6 element linear configuration, a 10 element Cornwell ring (Cornwell, 1988), and a VLA-type 'Y' array also comprised of 10 elements. In all cases the arrays were assumed to be rotated with respect to the source so as to achieve adequate uv -plane coverage for faithful imaging. We concentrated on the effects of the density and uniformity of the uv -plane sampling and its effects on phase retrieval, and did not address other related issues such as sensitivity. The results are shown in Figure 3.1. For the linear configuration 6 rotations of the array have been assumed, whereas for the other two geometries only 3 rotations were used. In each case the total number of independent uv -points measured was 135. Apart from the image of the resolved star obtained with the Cornwell ring, the reconstructions are extremely good in all three cases.

In general, all three arrays performed similarly, but the results obtained with the ring array were not quite as good. For a small number of array elements, as used here, this type of configuration provided relatively poor short-baseline uv -plane coverage and proved unsuitable for imaging the resolved stellar disc model. Clearly, a straightforward solution to this problem would be to expand or contract the array during the observation. As expected, for a given number of visibility data, the array with the larger number of elements provided slightly better image quality.

Not surprisingly the results of the simulations were consistent with a number of rules of thumb established in radio VLBI where similarly sparse arrays have been used for imaging for many years. These can be summarized as follows:

- Assuming quasi-uniform uv -coverage with a maximum baseline u_{max} and a sampling interval Δu , the field of view and resolution will be limited to $\sim 1/\Delta u$ and $\sim 1/u_{max}$ radians respectively
- The number of picture elements in a map should scale approximately as $(u_{max}/\Delta u)^2$.
- With an m telescope interferometer one should be able to map areas of sky containing on the order of $\leq [m(m-1)/2]^2$ filled pixels.

These rules of thumb, which have been verified in practice using ground-based instruments such as the 7 antennae Merlin radio array, are summarized in quantitative terms in Table 3.1. This table is based on realistic estimates for the maximum source dimensions for which imaging might be envisaged.

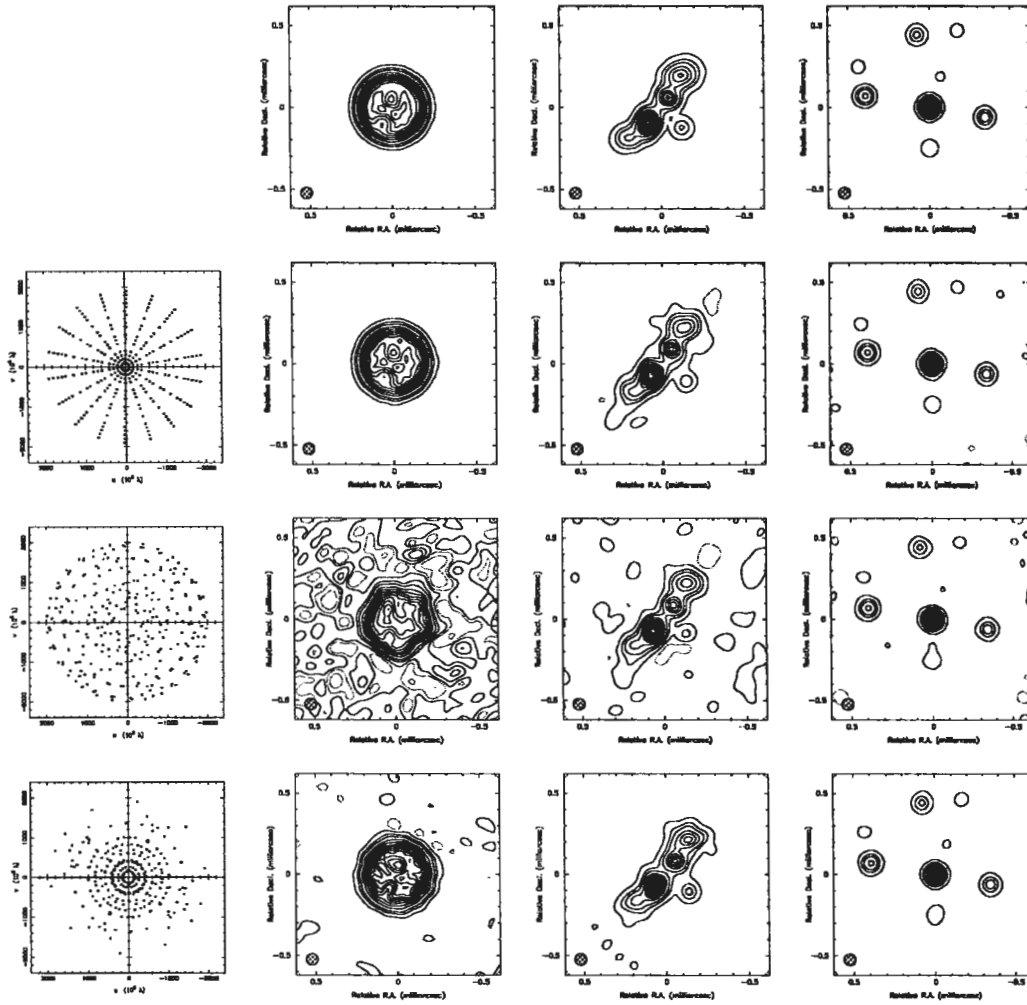


Fig. 3.1 Simulation of imaging with a sparse interferometer at optical wavelengths. The three test objects, a spotted stellar disk, a cluster of resolved overlapping Gaussians, and a stellar cluster, are shown on the first top row. The reconstructed images are shown below, each row corresponding to the performance of a different array, respectively a 6-element linear array, a Cornwell 10-element array, and a 10-element 'Y' array. The uv -plane coverage for each configuration is shown at the left of each row.

Table 3.1 Imaging scenarios

Number of telescopes	Number of baselines	Max dimension of box source [†]	Max dimension of linear source [†]
4	6	≤ 10	≤ 20
6	15	≤ 20	≤ 50
8	28	≤ 40	≤ 90
10	45	≤ 60	≤ 150

[†] The unit of length used is the size
of the synthesized beam.

It seems then that the requirements for imaging extended sources containing even moderate numbers of filled pixels are really quite severe, since the results presented in the above table are based on 12 hour observations, i.e. half a day of earth rotation synthesis. For a space based array, the rate at which the uv -plane can be traversed will, in principle, be much faster, but it must be recognized that a similar density of sampling along the uv plane tracks will still be required.

3.3. Sensitivity

It is not possible to set a sensitivity requirement for a synthetic aperture system independently of other observational parameters. This is best appreciated by determining the total integration time required to accomplish the desired map of an object with a given dynamic range. The time required will be a function of the number of array reconfigurations needed to construct the map, and of the minimal signal-to-noise ratio needed to extract the dynamic range.

In the observed interferometric pattern, the signal corresponding to a given baseline (i.e. a uv point in the Fourier plane) is proportional to the energy in the corresponding 'cosine square' fringes. This energy is a function of the brightness of the source at that spatial frequency within a given solid angle, divided by the number of baselines. For a non-redundant array (an array where no two baselines are the same), the number of baselines is $m(m-1)/2$ where m is the number of telescopes in the array. The fact that the fringe visibility is inversely proportional to the number of baselines can be easily understood if one assumes that the fringes for each baseline are measured independently by splitting the flux collected in each sub-aperture and pairing it with every other subaperture. The detected source photons in each subaperture, (N_s/m) , is thus split $m-1$ times, so that the recombined flux for each pair is $2N_s/m(m-1)$. This result is also true when the fringe visibility for a given baseline is extracted from the whole interferometric pattern.

The signal corresponding to a given baseline is thus equal to

$$S = \frac{2N_s}{m(m-1)} |O(\xi)| \frac{1}{2\pi} \int_0^{2\pi} \cos^2 \theta d\theta, \quad (1)$$

where $O(\xi)$ is the normalized Fourier transform of the source brightness distribution, and the mean value of \cos^2 integral, which is equal to $1/2$, represents the average energy in the fringes at maximum visibility.

Taking the instrumental factors into account, this equation becomes

$$S = \eta \frac{n_s}{(m-1)} |O(\xi)| \frac{\pi D^2}{4} \Delta\lambda T QE t, \quad (2)$$

where n_s is now the source flux per unit time, unit bandpass and unit area, D is the diameter of each array element, $\Delta\lambda$ the wavelength bandpass, T the optical transmission of the system, QE the quantum efficiency of the detector, η is the interferometric efficiency (the ratio of the actual fringe visibility to that given by a perfect interferometric system) and t is the exposure time.

The background noise for that measurement over one pixel consists of the flux coming from the rest of the source within the acceptance angle of the system (the diffraction limit of the individual telescopes), the natural and instrumental backgrounds (zodiacal light, straylight, mirror thermal emission), and detector effects. Neglecting detector effects, the total number of photoelectrons at the detector is:

$$\frac{2(n_s + n_b)}{(m-1)} \frac{\pi D^2}{4} \Delta\lambda T QE t, \quad (3)$$

where n_s and n_b are the fluxes from a solid angle corresponding to the map size per unit time, unit bandpass and unit area from the observed source and from the natural and instrumental background respectively and the $2/(m-1)$ factor has the same explanation as for the signal.

With the noise equal to the square root of the total detected photoelectrons, the signal-to-noise ratio of the fringe measurement is:

$$\text{SNR}_f = \sqrt{\frac{(\eta n_s |O(\xi)|)^2}{2(m-1)(n_s + n_b)} \frac{\pi D^2}{4} \Delta\lambda T QE t}. \quad (4)$$

Now, one has to satisfy two conditions:

- a. the SNR for each fringe measurement (uv -point), must be at least 2; this is the condition for the phase closure technique to be useful (see 6.2.4). We will use a value of 3.
- b. the dynamic range in the final map must be good enough to satisfy the observer's requirement, a condition that can be translated to first order by having the completed map signal-to-noise at least equal to the desired dynamic range.

For a uniform source, and a map size with a total number of pixels of \mathcal{P} pixels, $|O(\xi)| \sim 1/\mathcal{P}$, so that the time required to reach an SNR of say 3 with a given configuration of the array is

$$t_{\mathcal{F}} = \frac{9\mathcal{P}^2 2(m-1) (1 + \frac{n_b}{n_s})}{\eta^2 n_s \frac{\pi D^2}{4} \Delta\lambda T QE}. \quad (5)$$

Assuming a non redundant array, each configuration supplies $m(m-1)/2$ baselines or uv -points in the Fourier plane, from which 2 degrees of freedom must be subtracted to match subsequent frames. For an extended object imaged over a map of \mathcal{P} non-zero pixels, the required number of reconfigurations will thus be,

$$N_{cf} = \frac{2\mathcal{P}}{m(m-1)-4}. \quad (6)$$

Hence, the condition a) above requires that the *total* integration time be:

$$t_{int} = \frac{2\mathcal{P}}{m(m-1)-4} \frac{9\mathcal{P}^2 2(m-1)(1 + \frac{n_b}{n_s})}{\eta^2 n_s \frac{\pi D^2}{4} \Delta\lambda T QE}. \quad (7)$$

Again, assuming a non redundant array, and non redundant reconfigurations, the total number of *uv*-points in the final map is equal to the number of baselines per configuration, i.e. $m(m-1)/2$, times the number of reconfigurations. Since the signal-to-noise ratio of the entire image is equal to the signal-to-noise of the individual baseline measurement times the square root of the number of *uv*-points in the final map, condition b) leads to the equation:

$$DR = \text{SNR}_{image} = \text{SNR}_f \sqrt{\frac{m(m-1)}{2} \times \frac{2\mathcal{P}}{m(m-1)-4}}, \quad (8)$$

where *DR* is the dynamic range. Assuming again that $|O(\xi)| \sim 1/\mathcal{P}$, the corresponding *total* integration time is then:

$$t_{int} = \frac{2 DR^2 \mathcal{P} (1 + \frac{n_b}{n_s}) (m(m-1)-4)}{m \eta^2 n_s \frac{\pi D^2}{4} \Delta\lambda T QE} \times \frac{2\mathcal{P}}{m(m-1)-4}. \quad (9)$$

Satisfying conditions a) and b) together requires taking the maximum of the results of equations 7 and 9. Taking into account array reconfiguration overhead, the total observation time for an observation can be thus expressed as follows:

$$t_{obs} = \frac{4\mathcal{P}^2(1 + \frac{n_b}{n_s})}{\eta^2 n_s \frac{\pi D^2}{4} \Delta\lambda T QE} \text{MAX}\left(\frac{9\mathcal{P}(m-1)}{m(m-1)-4} \text{ or } \frac{DR^2}{m}\right) + \frac{2\mathcal{P}}{m(m-1)-4} t_{setup}, \quad (10)$$

where t_{setup} is the time overhead required for array reconfiguration and the associated pointing star and reference star acquisition if applicable.

This final equation gives the respective influence of the dynamic range, number of pixels in the map and bandpass and shows how these parameters can be traded off against each other to best respond to the scientific problem and source under study. This is the basic equation that we will use in the establishment of the mission scientific program (Chapter 5), the comparison of space to ground based interferometers, and the comparison of the free-flyer and moon-based space interferometers.

One notes that, to first order, and assuming that the prevalent condition is due to the dynamic range in the map and not the minimum SNR condition for individual maps, the observing time is proportional to:

$$t_{obs} \sim \frac{\mathcal{P}^2 DR^2}{n_s m D^2} \quad (11)$$

where m is the number of telescopes in the array, D their diameter, n_s the source flux, DR the desired dynamic range, and P the number of pixels in the final map.

3.4. Spectroscopy

In many research programs, high resolution imaging makes sense only when accompanied by spectral resolving power. This is because higher spatial resolution typically allows one to look at local physical processes which are so complex that spectral resolution is needed to understand them. The observable effects of mechanisms such as magnetic fields, star flares, wind, shocks, pulsation, rotation, etc.. can be correctly interpreted only if some spectral resolution is simultaneously used with imaging.

At spectral resolutions of 30,000 and beyond, the Doppler imaging technique can be extended to spatial interferometry for studying fine structures or velocity fields. It must be emphasized that Doppler imaging techniques are often limited by particular properties of the target such as the inclination of the stellar rotation axis with respect to the line of sight, and can produce ambiguous "star images". The addition of spatial information to spectroscopy completely eliminates these ambiguities and brings new insight regarding physical processes.

Spectroscopy at spectral resolution ranging between a few 1,000's and 30 000 combined with a spatial resolution of 0.02 milliarcsecond, can be an extremely powerful tool for studying the dynamics of stars and extra-galactic objects such as AGNs.

In conclusion, it appears essential that the science instrument package include some spectroscopic capability with spectral resolution ranging from 10 to 30 000.

3.5. Spectral coverage

Constructing and operating a space observatory extending to the ultraviolet is very demanding, with problems ranging from contamination issues to optics quality and very tight positioning tolerances. Since the identified science programs do not specifically emphasize a specific need for the ultra-violet band, we have, at least for the purpose of the technical study, relaxed the instrument tolerances and specified a spectral coverage starting at only 0.4 micron.

The visible range, on the other hand is the preferred domain for high angular resolution. As long as the optical pathlengths can be controlled at the required tolerances, the visible region offers optimal use of the maximum available baseline.

In the near-infrared, ground-based instruments are penalized at shorter wavelengths ($\lambda \sim 1\mu\text{m}$) by atmospheric turbulence and at longer wavelengths ($\lambda > 3\mu\text{m}$) by the thermal emission of the atmosphere and optics. Extending the wavelength coverage of the proposed interferometer beyond the visible appears desirable. The near infrared is a window onto the warm Universe: it corresponds to black-body temperatures ranging from 300K to 3000K, i.e. to the thermal emission of warm dust and gas up to the photosphere of cool stars. Many of the targets that we have identified would benefit from observation in the near-infrared. Some targets, such as YSO disks and dust shells around stars, can only be observed in the near to mid-infrared. Since cooling moderately large optics cryogenically would not be practical, how far the wavelength range can be extended in the infrared is determined by the lowest

temperature to which the optics can be passively cooled. Figure 3.2 shows the background flux for a typical space interferometer with optics at 60, 80 and 100 degrees K. Since a temperature of 80 degrees appears reachable, both in free space and on the moon, we have specified that the thermal instrumental background should not be more than the zodiacal light at 6 microns, with the optical system spectral range extending to 12 microns.

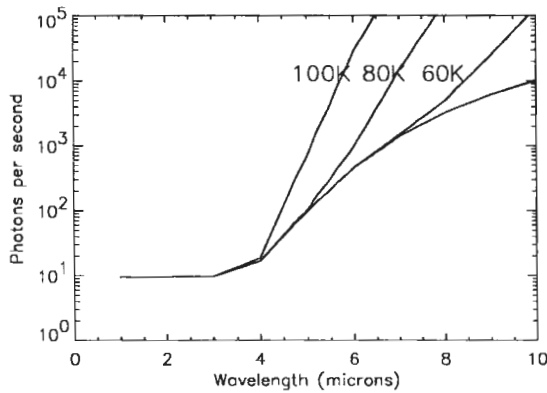


Fig. 3.2 Background flux from zodiacal light and thermal emission of the optics for a typical space interferometer. The interferometer is composed of six 1-meter diameter elements. The background flux is calculated for diffraction limited pixels ($\lambda/2D$), 3% mirror emissivity, 100% bandpass, 60% throughput and 90 % detector QE.

3.6. Astrometry

Narrow field astrometry, the only astrometry possible with the interferometer concept under study, relies on measuring the angle between the target and neighboring reference stars. Ideally, at least two reference stars should be used to fully constrain the position of the target under investigation. The field of a kilometric baseline imaging interferometer is necessarily small, typically on the order of the Airy disk of the sub-apertures i.e. around $0.1''$, while the bright enough reference stars are typically found within a few arcminutes from the target. Optical schemes could in theory be developed for a larger field (ref chapter 6), but would be unmanageable: at the scale required to match the high angular resolution achieved, a reference star at 2 arcminutes from the target would be 15 meters away in the focal plane. The solution lies in field multiplexing, i.e. in capturing small patches of the sky around the target and reference stars, and feeding the corresponding beams into the same optics all the way to the recombining optics. But this results in a fairly complex optical system, and after engineering analysis we have decided to limit field multiplexing to two channels, one for the target and the other for the reference star which is at all time required to cophase the array.

Having only one reference star does not preclude astrometry, however. Figure 3.3 shows the principle of *relative* parallax determination using a single reference star. The target object (S) and the line joining the location M_1 of the array orbiting around the Sun (\odot) and its location after 6 months (M_2) define the plane in which the parallax effect takes place, while the reference star (S_0), in the *same* plane, defines the direction with respect to which the parallactic effect becomes measurable through the *observed* angles α_1 and α_2 . The absolute parallax π_{abs} of the target S is $\pi_{abs} = \pi_{rel} + \pi_0$, where $\pi_{rel} = (\alpha_2 - \alpha_1)/2$, and π_0 is the trigonometric parallax of the reference star. Since a reference star is needed for every observation, two visits of any galactic target at 6 months interval automatically provide its parallax relative to the reference star. If the reference star is sufficiently faint (distant), the bias π_0 is close to zero, and

such a measurement essentially provides the absolute parallax of the target. We note also that π_0 might also be provided by a post-Hipparcos mission such as GAIA, and that the interferometer concept studied here could then become an efficient absolute parallax "machine".

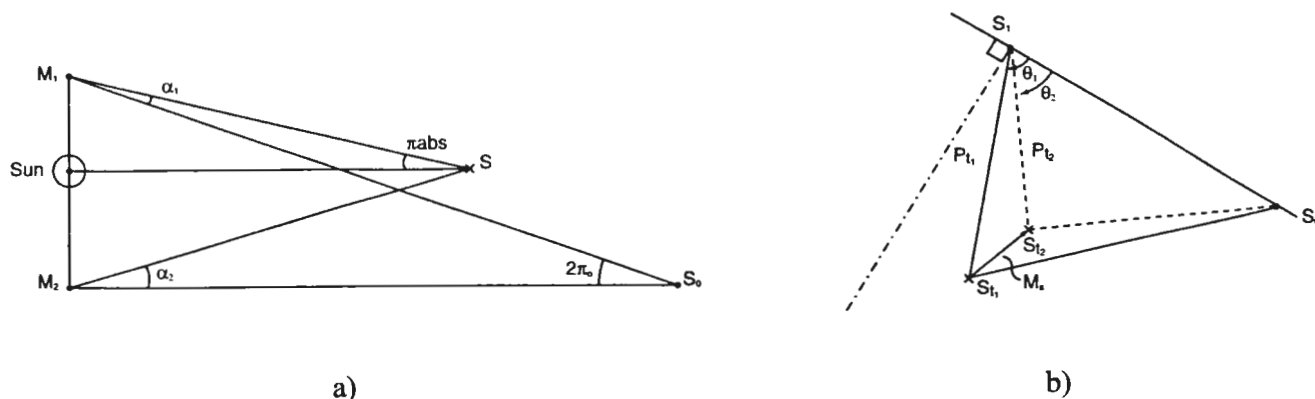


Fig. 3.3 a) Geometric principle of parallax determination. S is the parallax object and S_0 the reference star (following Lindegren and Perryman, 1994). See text for explanations. b) Two reference stars (S_1 and S_0) would provide the target proper motion (S_{t1} and S_{t2})

With only one reference star, i.e., without the 'fixed' direction materialized by two reference stars (S_1 and S_0 in Fig.3.3b), only the proper motion component along the target-guide star direction is measurable. Highly accurate one-dimensional proper motions would still be quite valuable for some of the scientific problems discussed in the previous section (e.g., cluster kinematics); however, issues like the direct determination of the mass of lensing MACHO's would have to be left out as important driver of the scientific program.

Parallaxes good to 1% at the distance of the Magellanic Clouds (~ 50 kpc) and to 10% up to 500 kpc require accuracies of $0.2 \mu\text{arcsec}$. A sensitivity analysis of a 2-element free-flyer option shows that to achieve the spatial coherence of $\lambda/100$ at 500 nm (i.e., ~ 5 nm) with a guide star within 5 arcmin from the line-of-sight, the station keeping requirements (which would contribute to the external optical path length) on the two most critical axes are of the order of a few microns, which appear feasible. Therefore, achieving a 5-nm control on the *internal* optical path, again a challenging but not impossible requirement, would provide a *guiding system* capable of keeping the *astrometric* angle β between the reference star and the target at the required $0.2 \mu\text{arcsec}$ level at maximum baseline (5 km).

It is important to note, however, that such a program requires access to the same target at six months interval, and thus an *instantaneous* sky coverage large enough to allow the pointing of these directions more than 90 degrees away from the one opposite to the sun. This is a condition which is very difficult to meet for the free-flyer version and also for the moon-based version, although to a lesser degree. In view of this instantaneous sky coverage problem and

of the stringent metrology requirement described above, we have not retained astrometry in our strawman scientific program. Alternatives to the present sun shield design in the free flyer option should be given further consideration in future studies in an attempt to regain the parallax astrometry capability.

3.7. Temporal resolution

At the level of resolution considered, some of the identified prime science targets can change on a time scale of hours and days due to physical processes, target rotation or proper motion. This will set a limit on the allowed accumulated exposure time and on the time allocated for sub-aperture reconfiguration. For complex maps requiring a large number of uv -points, the moon-based interferometer could need up to a lunar night (14 days) and is thus fundamentally limited in time resolution. The free-flyer on the other hand is not and we have specified, as a goal, a temporal resolution of 1 day or less.

3.8. Field

At the very high resolution afforded by the interferometer, field is not an issue. A "science field" limited to the Airy disk of the individual sub-aperture (0.15 arcsecond in the visible) will already require a large number of separate baselines for adequate sampling (on the order of a 100), and is large enough to be scientifically valuable. In practice the field will be limited by observing time which necessarily limits the number of reconfigurations possible and the spectral resolution. Additional problems may arise due to the fact that at optical wavelengths, unlike the case in the radio, the fields of target sources may be very densely populated.

3.9. Sky coverage

For all prime targets considered, the number of candidates is larger than the number that can possibly be studied during a mission lifetime of about 5 years. A limited sky coverage should therefore not be scientifically restrictive. Supernovae and gravity lensing events are targets of opportunity, but their expected frequency is sufficiently large to be also accommodated by a limited instantaneous sky coverage. Hence sky coverage, whether instantaneous or cumulated, is not a major issue (except for single reference star astrometry as explained above). As a guideline we have specified a 10% instantaneous coverage and 60% cumulated coverage over the entire duration of the mission. An additional condition is that the Large and Small Magellanic clouds, the Virgo cluster and the galactic center which contains a large fraction of the prime targets be accessible at least some time during the year.

3.10. Protection against straylight

As in any space optical system, it is important that the optics be well baffled against off-axis bright sources such as the sun, bright earth and the moon. An additional condition specific to interferometric arrays is that each element be protected from the light reflected, diffracted or diffused by the other elements.

Adopting a guideline similar to that set for the instrumental thermal emission discussed above, straylight from these sources should be negligible compared to the zodiacal light level.

3.11. Summary of Requirements

In summary, Table 3.2 lists the scientific performances deemed essential for a kilometric baseline space interferometer.

Table 3.2 Desired scientific requirements

Resolution	0.02 milliarcsecond (in V band)
Imaging	maps of up to 30 x 30 pixels [†]
Limiting magnitude	up to $m_v=30$ per res. elem. [†]
Dynamic range	up to 100 [†]
Spectral range	0.4 to 12 μm
Spectral resolution	up to 30,000 [†]
Temporal resolution	< 1 day*
Field	0.1 arcsecond
Astrometry	0.2 mas (excluded in this study)
Instrumental thermal background	< zodiacal light at 5 μm
Straylight	< zodiacal light
Instantaneous sky coverage	$\geq 10\%$
Cumulated sky coverage	$\geq 60\%$

[†]interdependant parameters - maximum values shown.

* not applicable to the lunar interferometer which relies on moon rotation for aperture synthesis.

Although the above summary table gives the range of the main desired performance parameters, we have seen that some of these parameters cannot be set in absolute terms because they are interdependent. The exact characteristics and operational conditions of the interferometer will thus have to be a compromise based on the types of sources to be investigated. At the same time, the scientific capability of a space interferometer should sufficiently surpass what could be achieved from the ground to make a space mission worthwhile. These issues are the subject of the following chapters.

References

- Cornwell, T.J., 1988, "A novel principle for optimization of the instantaneous Fourier plane coverage of correlation arrays", IEEE Tr., AP-8,1165.
 Lindegren and Perryman, GAIA, ESA SP-379, 1995
 Lindegren and Perryman, 1994, Internal report submitted to the ESA Horizon 2000+ Survey Committee

GROUND VS. SPACE

The sensitivity of a space-borne or terrestrial interferometers depends on source brightness and complexity and on the waveband considered. In the ultraviolet, atmospheric limitations preclude ground based observations. On the other hand, thanks to adaptive optics, a ground-based interferometer equipped with 8-meter class individual telescopes will easily surpass a small aperture space interferometer in the near infrared. A space interferometer regains the advantage in the visible and the thermal infrared where it is about 4 magnitudes more sensitive. The scientific program of a space interferometer must be selected to favor these domains of uniqueness.

Space observatories are orders of magnitude more expensive than their ground based counterparts. It is therefore vital to tailor a space instrument to a domain where it can be expected to deliver first rate science that could not possibly be approached by ground instruments now or in the near future.

There are secondary issues such as *uv*-plane coverage and sky coverage. But these factors are not decisive. We will thus limit our comparison to the main issue: sensitivity. This subject of sensitivity in ground-based and space interferometers has been treated by many authors (e.g. Ridgway 1992, Colavita and Shao 1991, Beckers 1991, Roddier 1988, Greenaway 1992). In what follows, we will review the determining factors at play and quantify the comparison in the particular case of the interferometer under study.

In the ultra-violet and at various wavelength bands between 1 and $10\mu\text{m}$, the opacity of the atmosphere precludes observations from the ground. The ultraviolet region is without doubt a unique domain for space. The completely open near infrared domain which has been only partially charted from the ground should also offer tremendous opportunities for new science. To be conservative, nevertheless, we have based our comparison only upon the difference in sensitivity between ground and space instruments operating in spectral regions accessible to both.

As a basis for the comparison we will assume that the terrestrial interferometer consists of an array of 8m diameter telescopes while the space interferometer elements are only about 1 meter in diameter. We will also assume that both interferometers have the same number of elements, say 6, over the same baseline length and that the same source is observed. Finally we assume that adaptive optics is used to correct the terrestrial instrument.

4.1. Atmospheric turbulence limitations

Adaptive optics is already being used very successfully for the correction of the wavefront distortions caused by the earth's turbulent atmosphere and continued progress is expected. For the purpose of this comparison, we have assumed an adaptive system consisting of 40 actuators on the diameter, and presumed that the wavefront distortions to be corrected are precisely known

and exactly reproduced by the adaptive system with a delay of 2.5 millisecond. A traditional measure of adaptive optics performance is the Strehl ratio of the formed image. This ratio indicates the fraction of the telescope collecting area that contributes flux to the diffraction-limited image 'core' used for interferometric measurements. We have used standard relationships (Parenti 1992) to compute the Strehl ratio that adaptive systems could be expected to achieve based on a modified Hufnagel-Valley turbulence profile and a Bufton wind profile to characterize conditions at a good astronomical site. The results of the calculation are shown in Table 4.1. Although adaptive mirrors with more actuators are likely to be available, the assumption of perfect wavefront matching with a delay of only 2.5 millisecond is likely to mean that the Strehl ratios shown in this table are quite optimistic.

In addition to wavefront distortions which are presumed to be corrected by an adaptive optics system, the atmosphere imposes random overall phase shifts on the wavefronts and as a result the detected fringe systems are unstable. Due to this instability the fringes must be detected in a short integration time if they are not to be unacceptably blurred. Values for this maximum integration time calculated with the atmospheric models mentioned above are shown in table 4.1. These maximum possible integration times are quite small and will not be improved by the use of adaptive optics. In the V-band for example, the integration time, τ , does not exceed 20 milliseconds even under excellent atmospheric conditions.

This limited integration time is the key disadvantage of the terrestrial instrument compared to its space counterpart. As we will describe in Chapter 6, reference stars in the field of view can be used to keep the space interferometer cophased over arbitrarily long integrations times. The sensitivity of the space interferometer is therefore limited only by the time allocated to the observation, or by considerations such as detector saturation. For the terrestrial counterpart, on the other hand, a large number of frames must be averaged to improve sensitivity. In theory, the overall signal to noise ratio will increase as the square root of the number of independent frames averaged, provided that each independent measurement is from the same mean and variance. In practice, variations in systematic effects and noise sources (atmospheric seeing, detector characteristics) will limit the ability to average many frames of data reliably. To be conservative in this comparison we have nevertheless assumed that these effects would be under control and have not imposed a limit on the number of frames to be averaged. It remains that each frame corresponds to a different and unknown phase because of atmosphere induced piston errors. As we will discuss in a Chapter 6, the technique of phase closure can be used to recover most of the phase information, provided that the data is not too noisy. Experience indicates that a signal to noise ratio greater than 3 in the closure phase measurements is needed for such a procedure to be viable. Beyond detector noise which may be the current limitation, it is this condition that fundamentally limits the sensitivity of the terrestrial interferometer.

4.2. Efficiency issues

Even in those spectral regions where the atmosphere is transparent there will be some loss due to scattering, which will reduce the optical efficiency of the terrestrial interferometer.

In addition, it is more difficult to obtain and keep good reflectivity on surfaces exposed to terrestrial conditions. Because of the large number of reflections between the primary mirror and the interferometric detection plane,

this amounts to a significant loss. We have assumed here that the reflectivity losses in a terrestrial instrument would be twice that of a space instrument. The efficiency factor, shown in Table 4.1 is the product of this factor of 0.5 for reflectivity loss with atmospheric transmission figures taken from Allen (Allen 1976).

Table 4.1 Ground interferometer atmospheric limitation

Band	λ μm	Fried parameter cm	Strehl ratio	Integration time seconds	Efficiency factor
U	0.365	9.4	0.05	0.012	0.166
B	0.440	11.8	0.13	0.015	0.200
V	0.550	15.4	0.27	0.020	0.250
R	0.700	20.5	0.45	0.027	0.333
I	0.880	27.1	0.60	0.035	0.500
J	1.26	41.6	0.78	0.054	0.500
H	1.65	57.6	0.86	0.075	0.500
K	2.22	82.2	0.92	0.11	0.500
L	3.60	147	1.00	0.19	0.500
M	5.00	217	1.00	0.28	0.500
N	10.60	536	1.00	0.70	0.500

4.3. Background fluxes

In the visible and near infrared, the cooling of detectors and improvement in read-out electronics in the near future may be presumed to eliminate the detector-associated background flux. At these wavelengths the emission from instrument surfaces may also be neglected. Thus, the only significant background flux is the zodiacal light and the atmospheric emissions in the case of the ground-based instruments. At these wavelengths, the atmosphere produces approximately 20 times the zodiacal flux level (Allen 1976). However, the flux level is not high enough to have a significant effect on the observations of the relatively bright objects targeted for high spatial resolution.

Beyond 5 microns the detectors must be cryogenically cooled to prevent thermal noise in the detectors from dominating detection. Assuming that both the ground-based and space-based detectors are cooled to 1°K or below, the detector flux will be ignored here. As for the natural backgrounds, zodiacal flux can be approximated by a black body at 265 K with an emissivity of $6 \cdot 10^{-8}$, and atmospheric emission by a black body at 260 K and emissivity of 0.08. The mirror thermal emission has been estimated on the basis of a temperature of 80 K and emissivity of 0.03 for the space instrument, and 270 K and 0.10 respectively for the terrestrial instrument.

4.4. Result of the ground vs. space comparison

The values from table 4.1 have been combined with background flux discussed above to produce the sensitivity comparisons shown in Figure 4.1. This figure demonstrates the enhanced sensitivity of a space interferometer in most wavebands.

At around 2 microns, the sensitivity of a space interferometer is inferior to what can be obtained from the ground with a large telescope interferometer.

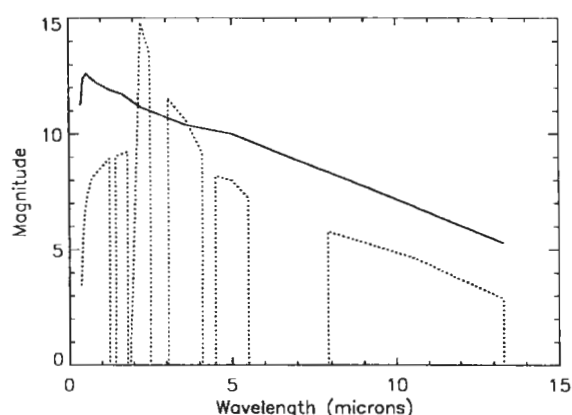


Fig. 4.1 Comparative limiting magnitude of space (solid) and ground-based (dotted) observations with a 6 element interferometer in 1000 seconds. The sub-aperture diameter is 1 and 8 meter for the space and ground based instrument respectively. The band-pass is that attributed to each ground-based spectral band. The space based instrument is about 2 magnitude more sensitive in all bands except in the K-band (2.2 microns) where the large ground telescopes equipped with adaptive optics are essentially unaffected by the atmosphere. (The ground based performance curve is based on very simplified atmospheric transmission.

At all other wavelengths, however, the space instrument is vastly superior. The difference in sensitivity is about 4 magnitudes. Translated into observing time, this means that the space interferometer is about 40 times faster for the bright targets (generally the case in the visible) to 1600 times faster for background limited cases (mostly near and mid infrared). A typical observation from space taking a total of 10 hours would simply not be possible with a ground based instrument. On the other hand, it may be wasteful to use a space instrument for making large maps of bright targets. Such observations require a large number of reconfigurations, and the corresponding overhead will strongly diminish the advantage of the space instrument.

In conclusion, we see that the space interferometer offers unique sensitivity at all wavelengths except around 2 microns where observations should be reserved to ground instruments, except in very special cases, such as when very long baselines are required or for complex objects, where the better *uv*-plane coverage of the space instrument provides a clear advantage. Although very efficient, the space instrument should not be wasted on the brightest targets when ground instruments could make the corresponding observations in a longer but still reasonable time.

References

- Allen C.W. *Astrophysical Quantities*, Univ. of London, Athlone Press, 3rd Ed. 1976.
- Beckers J M, *Exp. Ast.* 2, p57, 1991.
- Colavita M. and M. Shao, *Limiting magnitudes of ground and space interferometers*, Workshop Proc. Science objective and architectures for optical interferometry in space, JPL, 1991, Series 1, p143.
- Greenaway A. H., *Comparative aspects of Earth and space-based interferometry*, ESA SP-354, 1992.
- Parenti R R, *Adaptive optics for astronomy*, Lincoln Lab. J. 5(1992)93-113.
- Ridgway, S. T. *Visible and infrared imaging from space* Targets for space-based interferometry, ESA SP-354, 1992.
- Roddier F, *Interferometric imaging in optical astronomy*, Physics Report, 1988.

STRAWMAN OBSERVING PROGRAM

The imaging, spectroscopic and operational requirements of a very diluted interferometer depend heavily on the type of target to be observed. We establish here a balanced observing program upon which the interferometer design and operation can be rooted.

The main characteristics of an interferometer, particularly the number and size of individual subapertures and the spectral bandwidth, are driven by scientific requirements which often conflict. For example, given a total collecting area and a maximum resolution, sensitivity is favored by a small number of large apertures, while detailed imaging of a bright extended object would be better done with a large number of small apertures. Each observing situation has its particular optimal configuration.

In order to find a practical instrumental compromise we have established a strawman observing program based on the prime targets described in Chapter 3. This observing program was determined in an iterative manner by testing scientific desiderata against realistic capabilities and mission lifetime. This process was facilitated by formulating each type of target requirement in a computer program allowing for the testing of different instrumental parameters. The strawman program that we arrived at is shown in Table 5.1.

We intended to have a balanced share between the various scientific research themes, with about 70% dedicated to galactic targets and 30% to extragalactic research. Although the selection of the scientific program elements is somewhat subjective and a function of current research interests, it is broad enough to be generically representative.

A brief explication of each of the research goals and of the corresponding observational parameters is given below.

Star disks: Disk diameters are determined by measuring the visibility amplitude as a function of baseline length. This is best done in the visible to benefit from the highest resolution. The smallest measurable diameter is 20 microarcseconds which is half the interferometer resolution at the maximum 5 km baseline in the visible.

Supermassive binaries One simply searches for duplicity with a single visibility measurement at the longest baseline. Most candidates are to be found in the Magellanic Clouds and the smallest linear separation to be probed is 1 AU. The dynamic range need not be high as only stars of approximately equal magnitude are of interest. The bandpass is that of a typical wide-band filter.

Star surfaces (solar type): About 10 pixels across the surface are required to image spots and active regions. A high dynamic range on the order of 1:100 or better is also needed.

Star surfaces (magnetically active): One would expect to see a few big dark star spots with a contrast range of 50:1. Supergiants can be 10 mas in diameter, which is easily resolved.

Stellar surfaces (convection): The intent is to measure the granulation size power spectrum. This requires a very high dynamic range (100-1000) and

sufficient spectral resolution to resolve line profiles.

YSO disk: One would look for the near to mid infrared emission and resolve the question as to whether it is a disk or not. There will not be any sharp boundaries. The bandpass can be fairly broad.

YSO jet: The intent is to determine the direction of the jet relative to the disk and determine the jet velocity field. High spectral and spatial resolutions are required.

Globular cluster core: The intent is to detect stars and motions of stars in the continuum working at 1 micron for higher spatial resolution.

Galactic Center: The intent is to simply detect and astrometrically measure the position of stars to determine their orbital motion. One would expect 10 to 25 stars of $m=12.5-17.5$ in a 0.1 arcsecond field of view. This is best done at 2 microns which is the shortest wavelength that can be seen. Although this would be within the sensitivity range of a large ground interferometer, only a space based interferometer would have the required astrometric accuracy.

Cepheids: One would expect to see diameter changes of order 10% of a uniform disk in a few days. This is measured by sampling the visibility amplitude as a function of baseline length. The disk size is 50 solar radii, which at a distance of 1 kpc is partially resolved with a 3.5 km baseline. The magnitude is in the 10-15 range. A high spectral resolution (1000) is required in order to correlate spatial with spectral data.

Contact binaries: The size is expected to be about 5 solar radii. At a distance of 100 pc ($mv=10$) the entire system fits into 5-10 pixels of 40 μ as. The V-band is required in order to obtain the highest spatial resolution. Since the orbital period is about 6 hours, the best strategy is to stay at the longest baseline of 5 km while the system rotates.

Cataclysmic binaries: One needs to distinguish two unresolved sources a giant and a white dwarf. The accretion disk would not be resolved (1 μ as), but its doppler shifted lines can be seen with a resolution of 500.

AGN Broad Line regions. One would expect to see a compact (unresolved) continuum core, an obscuring torus and a halo of hundreds of clouds. But this halo would not be separately distinguishable. Low spectral resolution is needed to study the broad (10,000 km/s) lines. Highest possible spatial resolution (5 km, V-band) needed for spectral line mapping. The dynamic range required is about 1:100 for cloud halo.

Extragalactic supernovae (out to Virgo cluster): The intent is to look at the expansion of the SN itself, not the echo ring. This is best done in the V-band, because short wavelengths are visible sooner after the explosion, and the expansion is more rapid. At the distance of the Virgo cluster, an expansion of from 6 to 60 μ as is resolved with 5 km in V-band.

Gravitational lenses: One would follow the lensing events of stars in the galactic bulge first detected by ground surveys. The expected size of the Einstein-ring is 1 mas for solar mass objects, and 100 μ as for 0.01 solar mass. The limiting magnitude for a background star is 20th.

Gravitational waves: Detection is provided by monitoring the wobbling of a third component around a degenerated system. Useful resolution is at 80 μ as, the magnitude difference less than 5 magnitude, and a minimum of 5 visits are required.

Table 5.1 Target parameters

Target	Typic. size (mas)	Map size	Dyn range	Mag. limit	Wave- length (μ m)	Band- pass	Phen. timesc.	Number objects	Number visits
Star disc	0.40	9	20	20	0.55	0.0100	days	100	1
Supermass binar	0.04	4	100	16	0.55	0.0100	days	10	10
Star surface - active	1.00	100	100	10	0.70	0.0200	days	10	10
Star surface - convec	0.08	16	200	12	0.55	0.0020	days	10	3
Star surface - solar	0.80	400	100	5	0.70	0.0100	days	10	5
Star surface - magnet	1.40	64	100	15	0.70	0.4000	days	10	5
Dust Shells	30.00	49	40	6	5.00	0.0002	years	20	10
YSO Jet	2.00	49	10	10	2.22	0.0001	days	20	10
YSO disc	5.00	49	30	12	10.60	0.0500	years	20	5
Globular Cluster	12.00	16	100	17	0.88	0.1000	months	20	5
Galactic center	20.00	36	40	13	10.60	0.2000	years	1	40
Cepheids	0.20	64	40	10	0.70	0.0010	days	50	5
Contact binaries	0.24	64	50	10	0.70	0.0010	hours	10	10
Cataclysmic binaries	0.12	16	50	18	0.55	0.0200	hours	10	10
Gal Gravit. Lenses	1.00	16	10	19	2.22	0.1000	weeks	50	10
AGN BLR	0.25	25	100	16	0.55	0.0500	weeks	50	1
Extr. Gal. SN	0.12	9	60	18	0.55	0.0100	weeks	40	5
Subst Grav. Lenses	1.00	16	80	19	0.88	0.2000	weeks	30	5
Grav Waves	1.00	25	100	18	0.55	0.5000	days	20	5

IMPLEMENTATION PRINCIPLES

We describe our philosophy for the design of the interferometer, select its general parameters and present the main options that are common to both the moon-based and free-flyer versions

6.1. Optical pathlength control

Without doubt, the most important problem in optical interferometry is the control of the optical pathlength from each sub-aperture so that the beams from each sub-aperture are recombined in phase. In this section we establish the optical pathlength tolerances and describe the approach adopted for controlling their stability requirement.

6.1.1 Optical pathlength control tolerances

For zero-mean random optical pathlength fluctuations, the mean expected fringe visibility after an elementary exposure will be reduced from unity to $1 - \Delta\Phi^2/2$, where $\Delta\Phi$ is rms phase fluctuations. For our allocated loss of 1%, $\Delta\Phi$ must be less than 0.14 radians, i.e. a path error of $\lambda \Delta\Phi/2\pi$ or $\lambda/44$ rms. At visible wavelengths, this represents about 15 nanometers.

Absolute positioning of the individual interferometer elements to this accuracy is unlikely to be achievable using purely passive means. In the case of a moon-based interferometer, seismic activity and tidal effects will create unpredictable motions at least one order of magnitude larger. For the free-flyer scheme, inertial stability to 15 nanometers during an integration period of, say, 5 minutes would require differential accelerations of less than 10^{-13} m/s² (displacement = $\frac{1}{2}\gamma t^2$). Such a low gravity gradient can only be found at distances of several astronomical units from the sun, an option we have not considered here because of the obvious power, communication and launching difficulties associated with operating an interferometer in such a location.

The optical pathlengths between each subaperture and the beam recombiner must be controlled actively. Controlling pathlengths to 10 nanometers is easily achieved by moving small optical elements in the transfer beam, but corresponding metrology is difficult. The determination of the distance between the recombining hub and a subaperture with nanometer accuracy is certainly possible using traditional laser ranging. However, laser ranging will not detect transverse displacement to the level required (Figure 6.1).

An innovative solution, proposed by Kulkarni et al (1994), consists in locating the recombining hub out of the plane of the interferometer subapertures, and in launching counter-rotating laser beams between the apses of the 3-dimensional body thus formed. This constitutes a giant "pyramidal laser gyro", and permits the rotational motion of the cluster to be measured to very high precision using the Sagnac effect. The feasibility of this approach is currently being studied by S. Kulkarni and his group.

Our approach is to capitalize on the availability of unresolved reference stars in the telescope field of view. By monitoring the fringes from a reference star, the positioning tolerances on the interferometer elements are relaxed by several orders of magnitudes. A schematic outline of this approach is shown in Figure 6.2, where the target is assumed to be in the plane perpendicular to the subaperture plane. The "internal optical pathlengths" (AO and BO) of the target and reference star are common except that the reference star beam of the right leg goes through a delay line (Δ_{rs}) to compensate for the external path difference. If the subaperture A moves to A' , this is sensed by the reference star fringe tracking system and compensated by a vernier delay line system, Δ_c , which is common to both the reference star and target beams.

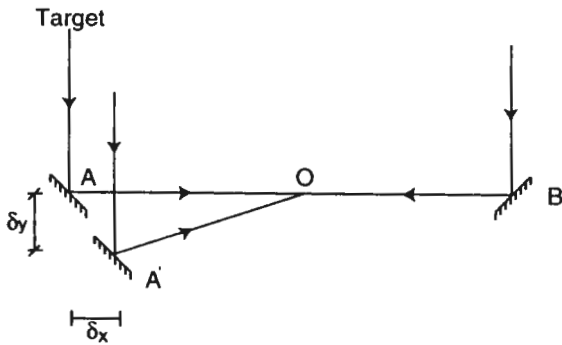


Fig. 6.1 For absolute control of optical pathlengths, the position of each subaperture must be determined to about 10 nanometers. Measuring the longitudinal displacement (along the x axis) to this accuracy by traditional laser ranging may be achievable, but measuring the transverse motion (along y) which corresponds to an angle of order $10 \text{ nm} / 2.5 \text{ km} = 4 \cdot 10^{-12}$ radians as seen from the recombining hub is not yet feasible.

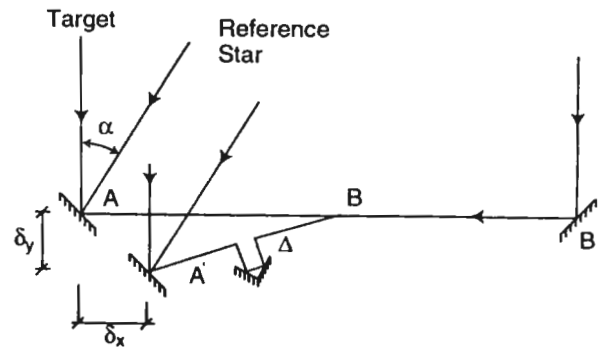


Fig. 6.2 Optical pathlength control with an unresolved reference star. The use of a vernier delay line common to both the target and the reference star beams relaxes the interferometer elements positioning tolerances by several orders of magnitude (see text).

If δx and δy are the longitudinal and transverse displacements of the subaperture A , the fringe tracking system will adjust the vernier delay line by Δ so that,

$$-(1 + \alpha)\delta x + (1 - \frac{3}{2}\alpha^2)\delta y + \Delta = 0$$

where α , the reference star to target angle has been assumed to be small, typically a few arcminutes. This delay correction in turn leads to a compensation on the target beam given by:

$$-\delta x + \delta y + \Delta$$

which is not quite zero. The resulting error for the target beam is:

$$\delta OP = -\alpha\delta x + \frac{3}{2}\alpha^2\delta y$$

For this error to be less than 15 nanometers rms, and with α approximately 2 arcminutes, one need only control δx and δy to within $18\mu\text{m}$ and 20 mm rms respectively, where we assume that the two directions of motion are independent and give each equal budget allocation. Satisfying this level of metrology with laser ranging is very straightforward.

6.1.2 Optical pathlength control

As outlined above, cophasing of the subapertures is accomplished by monitoring the fringe patterns produced by an unresolved reference star in the field of the individual telescopes. Below we determine the magnitude of the nominal reference star and establish what sampling rates are possible as a function of the sub-aperture diameter.

Reference star

In order to guarantee satisfactory cophasing of the interferometer the reference star will need to display a high apparent fringe visibility, even at very long interferometer baselines. A 5 km interferometer operating at visible wavelengths will have a resolution of typically $20\ \mu\text{arcseconds}$. Thus to ensure apparent fringe visibilities of at least 90%, the reference star will need to subtend an angle of no more than about $10\ \mu\text{arcseconds}$.

Published star count tables indicate that the majority of stars in the solar neighborhood are dwarfs later than K5 with diameters of about $0.7 D_{\odot}$. Therefore, stars from this group would be usable as reference stars only if they are more distant than about 400 parsecs, which corresponds to an apparent magnitude of ~ 18.5 or fainter. At such a distance the red dwarfs would appear quite faint ($V \geq 17.0$). Based on this condition and traditional star count statistics, a field of 2.5 arcminutes in radius is required to find at least one such suitable reference star at the galactic poles with 95% probability.

We have confirmed this estimate with a detailed statistical analysis using the digitized plate archive available at the Space Telescope Science Institute. This was done for two representative directions: one close to the North galactic pole (NGP) ($l = 162^\circ, b = 87^\circ$), and the second (N081) along the galactic anticenter at $l = 136^\circ, b = -2^\circ$. The NGP catalog contains BVR_C photographic photometry for 15413 stars down to $V=18.5$ and covers a region of $4^\circ \times 5^\circ$ square degrees. The N081 field covers a square area of 2° on a side and lists 27266 objects down to $V=18.0$ (Spagna et al. 1995 and references therein). The photographic photometry is good to 0.1 mag for both magnitudes and colors, and the relative positional accuracy is better than $0.2''$. The angular resolution on the photographic plates utilized for the two surveys is $\geq 4''$. This is too coarse for this analysis to address properly the issue of frequency of 'spoiler' stars (i.e. extended objects with a star-like appearance at this scale).

The calculations were based on 1000 random pointings within each of the two regions above. For each pointing both the differential counts, $dN(r)/dr$ (where r is the elongation from the target) and the integrated counts, $N(r)$, up to r_{lim} (the maximum permitted elongation) are computed. Finally, the relevant statistics are produced by averaging over the 1000 random pointings.

Figure 6.3 shows the histogram of the frequency of pointings with a given number of suitable (18.5 magnitude or brighter) reference star within 2.5' elongation for the NGP field. The sample mean and standard deviation are 3.7 and 2.0 stars, respectively. Using Poisson statistics, the calculated probability of finding at least *one* reference star within 2.5' from the target and down to

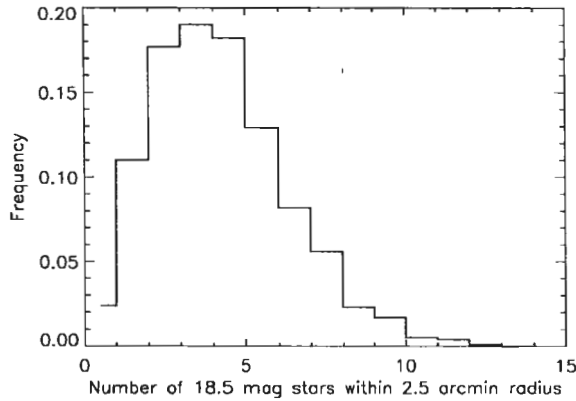


Fig. 6.3 Histogram of the frequency of pointings with a given number of 18.5 magnitude reference stars with an elongation less than 2.5 arcminutes at the north galactic pole.

$V=18.5$ is 97.5% for the NGP and 100% for the galactic plane field N081 ($V \leq 18.0$).

We then analyzed our star lists to evaluate the typical distance of an 18.5 magnitude reference star. The relatively faint reference star magnitude limit puts the average distance toward the NGP to safe values. The galactic plane field required a more careful analysis because it is affected by 'heavy' reddening (more than 4 mag/kpc). A simple de-reddening iterative procedure (which uses the observed $V-R_C$ as the un-reddened starting value) was used to estimate the average spectral types. The results of our investigation show that the N081 field contains, typically, K7V–M0V stars at an average apparent magnitude of $V=16.3$. Their typical distance is therefore 400 pc, which corresponds to an apparent diameter of $\sim 13 \mu\text{arcsec}$ and indicates that they would also be unresolved.

We conclude that the field required to find an unresolved star with at least 95% probability is 2.5 arcminutes in radius, and that the star magnitude will be 18.5 in the worst case.

Fringe tracking

Whatever fringe tracking system is used to cophase the array, the resulting precision of fringe measurement will scale linearly with the apparent fringe visibility and as the square root of the number of photons detected (assuming photon noise limited detection). Under general conditions, the error in the phase measurement is given by

$$\Delta\phi \sim \frac{1}{V\sqrt{N}}$$

where V is the apparent fringe visibility, N is the total number of photons detected in a single interferogram, and $\Delta\phi$ is in units of radians. For a multi-aperture interferometer, the apparent visibility will be inversely proportional to the number of sub-apertures for a completely unresolved reference source, so that the phase measurement error can be rewritten as:

$$\Delta\phi \sim \frac{m}{\sqrt{N}}$$

where m is the number of interferometer elements and N is the number of photons detected per array element per integration time. It is straightforward

to recast the above equation, setting the allowable phase error to $\lambda/44$, to derive the minimum acceptable sub-aperture diameter for a given reference star brightness, optical bandpass, efficiency and integration time. Figure 6.4 gives the sub-aperture diameter required to provide adequate phase measurement as a function of the integration time. The maximum integration time which can be afforded depends upon the interferometer disturbance level and the characteristics of the complementary sensors. For both the moon-based and the free-flyer schemes, we will show later that this maximum integration time must be 10 seconds, which indicates that the sub-aperture size should be around 1 meter.

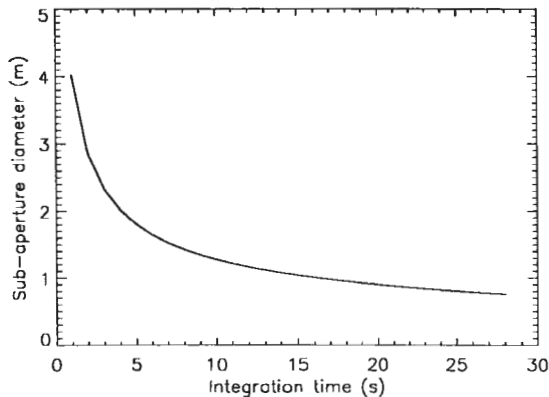


Fig. 6.4 Sub-aperture diameter required as a function of reference star fringe tracker integration time. The calculation is done for an 18.5 magnitude star and a fringe tracker operating in the visible with an overall efficiency of 10% and a bandpass of 300nm. The measurement error is $\lambda/100$, which gives a margin of safety of 2 compared to the specified pathlength control tolerance.

6.2. Aperture synthesis

Imaging with a multi-aperture interferometer is realized by making *sequential* measurements of fringe visibility for various configurations of the array. Each sub-aperture spacing provides a spatial frequency component of the source. Small sub-aperture spacings produce large fringe spacings, i.e. low-frequency components, while large sub-aperture spacings supply the high angular resolution information. Once sufficient measurements of the visibility function have been made by re-arranging the interferometer elements, a map of the source can be constructed using straightforward Fourier inversion complemented by image restoration techniques to compensate for missing frequencies. This is called aperture synthesis, in the sense that the reconstructed image is equivalent to that which would have been obtained with a filled aperture of a diameter equal to the largest interferometer baseline.

The quality of the reconstruction depends mainly on the number of visibility measurements, their signal-to-noise ratio, and their distribution in the measurement space (the so called *uv*-plane coverage). In the following sections we describe how we have selected relevant interferometer parameters and operational modes in order to satisfy the requirements of the proposed science program.

6.2.1 Number and size of subapertures

The interferometer mapping capability is a function of the number of sub-apertures and array reconfigurations. The required array reconfigurations in turn drive the overall observation time. But observing time is also a function of the sensitivity to be reached and is controlled by the size of the sub-apertures.

For a given mission time, the optimal number and size of sub-apertures are clearly a function of the particular science program to be undertaken. For example, mapping of complex but bright sources would be best done with a large number of small apertures, while simple faint sources would push for a small number of large apertures.

To determine the optimal number and size of sub-apertures which best serve our strawman program, we have conducted a parametric study with the assumption that the program had to be accomplished over 5 years for the free-flyer and 10 years for the moon-based version. The result is summarized in Figure 6.5 which gives the interdependence of the size and number of sub-apertures. From the pure science capability point of view considered here, we see that the sub-aperture size could be as small as 60 cm or less provided that the number of sub-apertures is large enough (say 10). However, as we have seen above, the need to use unresolved and thus faint stars for cophasing the array imposes a 1 meter minimum size.

Another operational constraint which we will examine later is the need for a sufficient number of sub-apertures (6 or more) in order to provide good phase recovery in the likely case where array cophasing cannot be perfectly maintained over the full duration of observation.

Adding these two operational conditions to the scientific capability requirement fairly constrains the problem: the sub-aperture size should be around 1 meter and the number of sub-apertures 6 or 7.

Clearly, this optimum set of instrumental parameter depends on the science program. Significantly changing the relative importance of the various types of targets would affect the result. To complement this purely observational parametric study, we have also examined the influence of the sub-aperture number and size selection on overall project cost. The details of this trade-off cost study are given in Appendix B and summarized in Figure 6.6. The cost reduction that one could have expected for a larger number of identical smaller units does not materialize because the subapertures are not allowed to go below the size of 1 meter. As a consequence, there is no reason to expand the array beyond 6 elements on the basis of cost.

In summary then, the unit telescope size should be at least 1 meter to permit cophasing on unresolved reference stars, and the number of telescopes should be at least 6 to allow for adequate phase closure and rapid coverage of the uv -plane. While increasing the number of telescopes would enable a greater scientific program to be undertaken, it would also cost more. Consequently, we have baselined both the free-flyer and the moon-based interferometers on 6 apertures of 1 meter diameter.

6.2.2 Array configuration

Most of the targets in our strawman program require detailed mapping. With a limited number of array elements, this can only be accomplished by rearranging the locations of the elements with respect to the source over time. Without re-configuration, the range of spatial scales that the instrument will be sensitive to will be inadequate for a useful science program. On the moon this capability is naturally provided by the lunar rotation, but for the free-flying concept some form of mobility of the individual interferometer elements is essential.

We also note that, with few exceptions, targets in our strawman scientific program require that the uv -plane be covered as uniformly as possible.

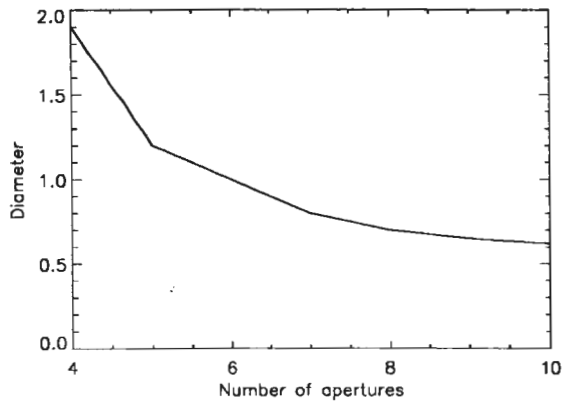


Fig. 6.5 Sub-apertures diameter required as a function of the number of sub-apertures to accomplish the reference mission. The mission duration is assumed to be 5 years for the free-flyer, and 10 years for the moon-based scheme because of its lower observing efficiency.

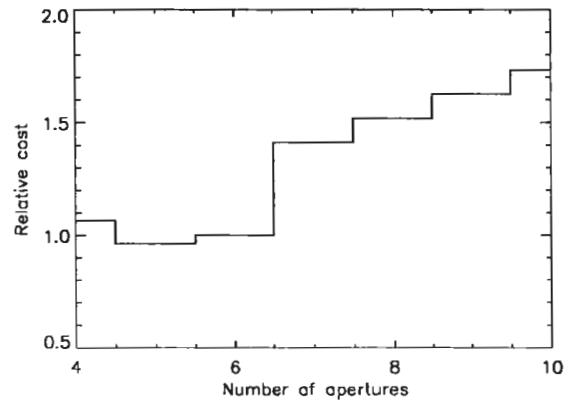


Fig. 6.6 Relative cost of a moon-based and a free-flyer interferometer as a function of the number of telescope units needed for a mission completion rate of at least 100 %. The sub-aperture cannot be less than 1 meter to permit cophasing on a reference star. With this condition, the science program that can be accomplished with more than 6 telescopes is greater than the baseline strawman program. The discontinuity beyond 6 sub-apertures is due to the extra launch required.

A final condition is that the array be non redundant, i.e. that no two baselines, whether or not they belong to a given configuration, be equal and parallel. This is to maximize the uv -plane sampling.

Beyond these general considerations, selection of the appropriate configuration strongly depends on environmental conditions and operations. Further details of specific implementations preferred for the lunar and free-flyer options will be described later on.

6.2.3 Fringe visibility error budget

A prime concern in any interferometric telescope is the expected magnitude of internal coherence losses. Coherence losses have two main repercussions. First, they lead to a loss in the instantaneous signal-to-noise of the measured data, and can thus severely limit the fundamental sensitivity of the instrument (visibility losses, the factor η in the sensitivity formula of section 3.3, counts as the square in the sensitivity). Second, a loss in visibility, if non systematic and therefore not calibratable, might be incorrectly attributed to the source and compromise the overall reliability of the imaging process.

In the table below we have attempted to define an error budget for expected coherence losses in the instrument from a variety of causes. We have classified these losses in systematic errors, random common path errors, and non common path errors. Systematic effects will be calibrated out using observations of known unresolved targets, and their main drawback will be to reduce instrument sensitivity. Random effects on the reference star and target common paths only reduce the instrument sensitivity. By far the most dangerous effects are those that do not affect the target and reference star by the same amount since they directly affect the interferometer cophasing performance. The most demanding instrumental requirement will thus be to minimize differential drifts between the reference and target optical pathlengths.

Table 6.1 Fringe visibility degradation budget

Factor	Systematic	Random common path	Non common path
Optical pathlength equality	1 %	1%	-
Optical pathlength vibration	1 %	1%	-
Optical pathlength drift	1 %	1%	1%
Fringe tracking	1 %	-	1%
Polarization effects	3 %	-	-
Unequal intensity	0.1 %	-	-
Optics quality	10%	-	-
Tracking errors	1 %	-	-
Detector resolution	0.5%	-	-
Calibration errors (10% of system.)	-	-	2%
Total	18.6%	3%	4%

6.2.4 Phase closure

Thanks to the use of a reference star the interferometer will, in principle, be cophased at all times during observations. Because of long observing times and extensive baseline changes, however, it is likely that phase errors will creep in during observations. Some of the corrupted phases can be recovered with the phase closure technique when the interferometer is composed of more than three sub-apertures used simultaneously. This procedure allows high-fidelity imaging to be performed under conditions where absolute knowledge of the array geometry is not known for a complete observation, or where unknown perturbations disturb the array between measurements.

The phase closure technique relies on the fact that phase errors attributable to individual telescopes, for example those associated with ambiguities as to their location, will cancel out when summed over triplets of baselines that correspond to closed triangles of telescopes (Pearson and Readhead, 1984). The sum of the measured fringe phases around a closed loop of baselines is immune to such errors and supplies an element of information solely about the source. Clearly the larger the number of such independent triangles of baselines the greater our knowledge of the source. This is depicted graphically in Figure 6.7 which shows the fraction of the source amplitude and phase data recoverable as a function of the number of array elements m . This fraction, which is equal to $(m-2)/m$ for the phase and $(m-3)/m$ for the amplitude, increases rapidly for small values of m , but beyond a value of about 10 the rise is relatively shallow. In radio astronomy, six or seven apertures are usually considered adequate for useful imaging. We have followed that guideline here.

It is important to recognize that this ability to image in phase-unstable conditions does not come free. The overall noise level is increased slightly. For a point source, the increase is $\sqrt{(m-1)/(m-2)}$ where m is the number of sub-apertures. This is a small factor, however, when n is large. More importantly, phase closure requires that each visibility measurement be made with a good signal-to-noise ratio per baseline, typically larger than 2, otherwise the reconstruction starts producing spurious effects.

Although such methods can correct for large phase errors, the technique only works if instrumental phase errors remain constant during any given visibility measurement. Sub-aperture set-up errors and systematic effects can be

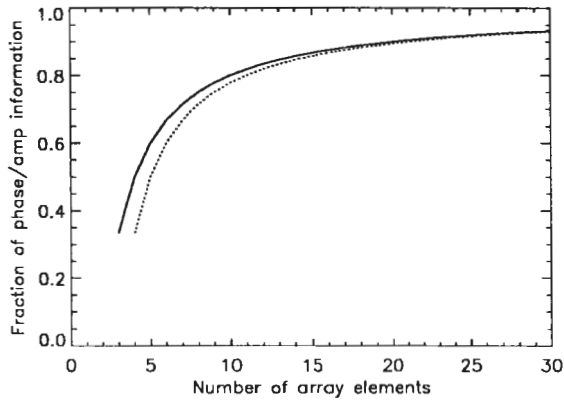


Fig. 6.7 Fraction of amplitude (dotted line) and phase (solid line) information recoverable using closure quantities as a function of the number of sub-apertures in the array. With 6 sub-apertures, 67% of the phase information can be recovered.

compensated for, but only if there are no non-zero-mean fluctuations in optical pathlength during a science integration. Zero-mean fluctuations, such as those due to vibration, will not affect the closure phases per se, but they will reduce their measurement accuracy since they reduce the signal-to-noise of the measurements.

6.3. Optical design

6.3.1 Optical pathlength equalization

In any interferometer, light from a source is collected by separate telescopes or subapertures and transferred to a central hub where it is combined. It will be possible to combine the wavefronts from each sub-aperture coherently only if all the optical pathlengths from the source to the detector are equal to a fraction of a coherence length of the radiation being observed.

A number of generic solutions for equalizing the optical pathlengths are shown in Figure 6.8. In case a) all the subaperture/hub distances are kept identical, but this requires the plane of the array to be oriented perpendicular to the source. This is the solution of choice for the free-flyer, but is clearly not applicable to a moon-based instrument. For a ground-based or moon-based instrument, path equality can be maintained during source tracking either by moving the subapertures (case b), or by using delay lines to compensate for the path differences (case c). In general, for the lunar-based instrument movement of the array elements themselves is expected to be extremely difficult. Not only does it require a prepared surface and adequate power, but it replaces the movement of small optical elements for gross bodily motions of massive structures at the sub-wavelength level. As a result of these general issues, our moon-based concept is designed around fixed telescopes and the use of movable delay lines.

6.3.2 Beam recombination

Beam recombination in an interferometer can be realized by one of two methods, traditionally referred to as the Fizeau and Michelson configurations. The discussion of this subject in the literature can often be confusing since the same Fizeau and Michelson terminology is often extended to cover the methods used for transferring the beams from the array elements to the recombining station (Beckers, 1986, Faucherre, 1989, 1990, Harvey, 1986). The original Fizeau and Michelson designs do indeed represent two extreme configurations, although hybrid configurations can be developed (Figure 6.9). However, the

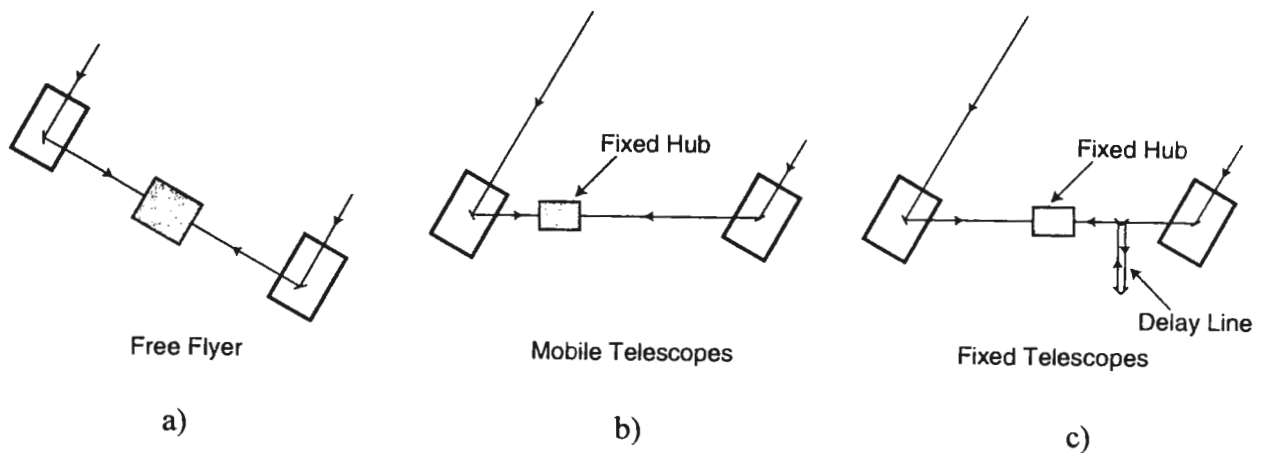


Fig. 6.8 Optical pathlength equalization in an interferometer. Case a) requires that the whole array be oriented perpendicular to the direction of the source, but delay lines and mechanical motion of the relay optics are avoided. This is the best solution for a free-flyer. In case b) the telescopes stay in the same plane (as on the earth or moon surface), but need to be moved when repointing and during target tracking. In case c), the telescopes are fixed, and optical pathlength differences when repointing or tracking are compensated by delay lines. This is the solution we have adopted for the moon-based version.

fundamental difference between the two designs lies not in the beam transfer mode, but in the geometry of the recombining itself.

The criterion distinguishing the two approaches relates to the arrangement of the pupil at the combining telescope. If the pupil is an exact scaled replica of the arrangement of the beams impinging on the telescope array, a condition called "pupil mapping", "pupil scaling", or preservation of the Lagrange invariant is satisfied. This condition is automatically fulfilled in the Fizeau configuration, but in the Michelson scheme one is free to rearrange the beams arriving at the recombining telescope at will. This is indeed usually done for practical reasons so as to minimize the number of fringes over the detector array.

If, in this case, the "magnification" of the recombining telescope (defined as the ratio of the reduced ordinates of the incoming beams to the ordinates of the corresponding subapertures), is not the reciprocal of the "demagnification" of the afocal subaperture telescopes, the wavefronts of the individual beams will not stay parallel to the overall wavefront for off-axis sources. This results in a non stigmatic focus, i.e. an essentially zero field of view. In the extreme case where the recombining telescope satisfies the pupil matching condition, the Michelson becomes functionally equivalent to the Fizeau interferometer with its field of view limited only by traditional aberrations.

For our application, with a sparse interferometer, the Fizeau/Michelson debate is somewhat academic. Due to the limited uv -plane coverage of such an array, images with many more than 100×100 resolution elements will be impractical to produce. For a 1 km baseline at $0.6 \mu\text{m}$ wavelength, this represents a field of view of only 15 milliarcseconds well below the Airy disk size of the assumed 1-meter individual apertures. The notion of a wide field of view

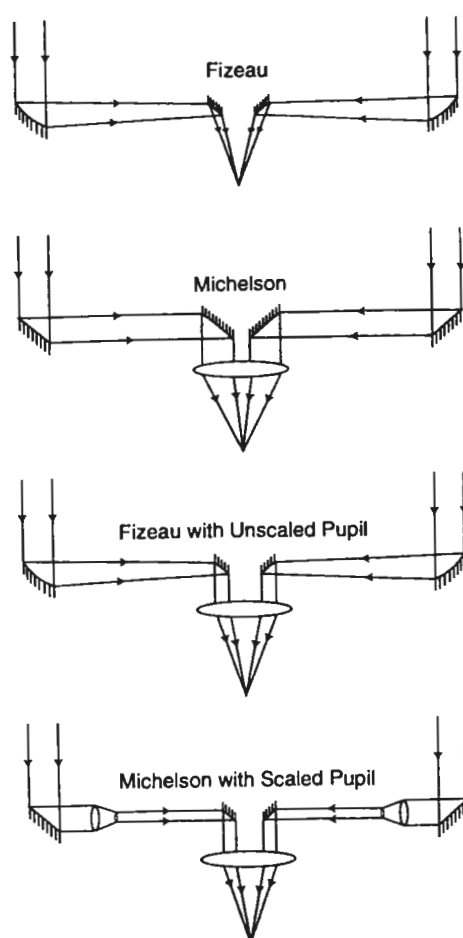


Fig. 6.9 Schematic of the Fizeau and Michelson interferometers designs. In the pure Fizeau design (top) the incoming beams are co-focused and combined, just as in a regular telescope working at full aperture. In the Michelson design the beams are collimated (and possibly demagnified) and then recombined (second from top). Although the two schemes differ as far as the beam transfer is concerned, the true difference arises because the Michelson recombining optics may or may not respect the scaling of the telescope pupil. Other systems include those that use converging (Fizeau) beam transfer but with an unscaled pupil (Michelson) recombination (third from top) or those that use collimated beam transfer and a scaled pupil (Fizeau) recombination (bottom)

is thus of little consequence for our proposed kilometric array, and so the flexibility of the Michelson configuration, where the geometry of the recombined pupil can be adjusted to produce only a few fringes in the image plane, is our preferred solution.

One might argue that the large field of view afforded by a Fizeau or Michelson interferometer with pupil scaling would allow direct access to reference stars over a wide field of view. However the large focal plane scale required for proper sampling makes this physically unrealistic: an $f/25$ f-ratio is typically needed to match the resolution to the pixel size of the science detector, so that a reference star 2 arcminutes distant from the science target would be 15 meters away! The solution to this reference star problem is clearly to use a split field instrument, as will be described later.

In our case, therefore, whether the beam transfer is of the afocal (Michelson) or common focus (Fizeau) type, it is clear that the Michelson (non-scaled pupil) recombination scheme should be adopted.

6.3.3 Telescope optical design

Having decided on a Michelson unscaled pupil recombination scheme, we have found no pressing need to use converging beam transfer from the subapertures to the recombining hub. Although converging beam transport has been proposed for both free-flyers (Kulkarni et al, 1994) and moon-based interferometers, this has been for implementation schemes that we have rejected: i) using three dimensional laser metrology for the free-flyer, and ii) using movable telescopes for the moon-based scheme. In our free-flyer approach, converging beam transport would actually lead to difficulties in the areas of straylight protection and the optical design so as to satisfactorily accommodate the variable hub/telescope distances. Because the free-flyer and moon-based versions were studied by two separate engineering teams, two design approaches naturally emerged for the optical design. These solutions were more or less equivalent in all areas except for the reference star beam transfer scheme. The moon-based version team selected to transfer the target and reference star beams via two separate channels using laser metrology to control equality of pathlengths, while the free-flyer team opted for a completely common path with spectral multiplexing.

6.3.4 Telescope/hub beam transfer

The diameter of receiving optics could be made small by focusing the transfer beam, but this would add complexity and moving parts in order to adjust the focus as a function of baseline. We have therefore selected an afocal transfer.

Using the Fraunhofer approximation and assuming that the central obstruction in the transfer telescopes is negligible, the energy transmitted to the receiving telescope is given by:

$$E = 1 - J_0^2(v) - J_1^2(v), \quad \text{with } v = \frac{\pi D_t D_r}{2\lambda l},$$

where D_t and D_r are the diameters of the transmitting and receiving telescopes respectively, λ is the wavelength and J_0 and J_1 are the Bessel function of zero and first order. Using equal diameters for the receiving and transmitting telescopes, Figure 6.10 gives the transmission efficiency as a function of telescope diameter at 0.6 and 12 microns. We have selected a 40 cm diameter as a good compromise between throughput, packaging convenience and cost.

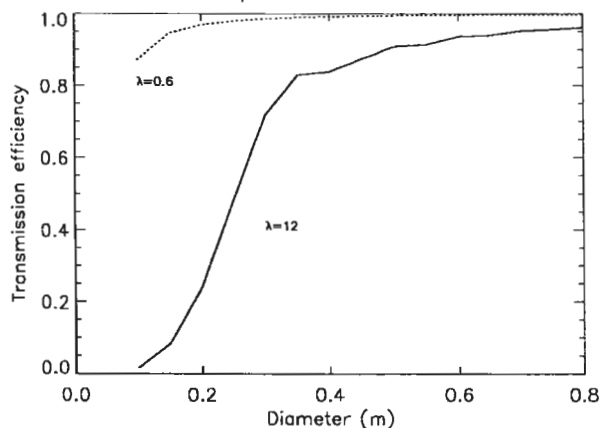


Fig. 6.10 Beam transfer efficiency as a function of telescope size for 12 and 0.6 microns and maximum baseline length (2500 m). Transfer efficiency with 40 cm telescopes is excellent in the visible and is still acceptable (about 80%) at 12 microns.

6.4. Focal plane instrumentation

Our philosophy concerning the focal instrumentation is to extend the reference star and target commonality of path as far as possible, i.e. all the way to the detector itself. This is for two fundamental reasons. The first is operational: a completely common path is the best guarantee for keeping the overall interferometer cophased on the target. The second reason is scientific: using the same beam combiner and detector for fringe tracking and science data confers total flexibility in the selection of wavelength bands for the reference star and the science target.

We describe hereafter a generic design following this philosophy, which is based on the technique of dispersed fringes adapted to a multi-aperture interferometer operated in space (Vakili and Koechlin, 1989).

For fringe tracking, ground-based interferometers primarily use the amplitude modulation technique (Shao et al. 1988) or spectrally dispersed fringes (Koechlin et al. 1996). In principle, both techniques have equivalent limiting magnitudes as long as interference detection is photon noise limited. Although modulation presents an evident simplicity in terms of hardware, the dispersed fringe technique is advantageous in terms of coherence length and flexibility. The main point here is that, since high spectral resolution is one of the prime scientific requirements, one can directly use the spectrograph and its detector for cophasing the interferometric array. The wide spectral coverage confers the extra ability to tune the spectral bands which are best adapted to fringe tracking on the reference star while recording fringes on the science target.

A schematic view of a possible implementation is shown in Figure 6.11.

The philosophy consists of co-aligning the reference and science beams before they enter the spectrograph and focusing their fringe signals on the same detector. In order to avoid the overlap of fringe signals from the reference star and the science target (which would uselessly superimpose uncorrelated photons, hence degrading the SNR), a set of large bandwidth filters is introduced up-stream of the spectrograph to separate them spectrally. This spectral selection depends on the dispersion. But how can one remap the output pupils from the 2D input pupil in order to sample fringe signals without degrading the spectral resolution? Since a Michelson beam-recombination has been adopted for the main interferometer, the trick lies in directing the 6 collimated beams from the telescopes towards the central hub and slightly tilting them so as to deviate the center of the array.

The collimated beams are intercepted before recombination by field telescopes which conjugate the output pupils on 6 flat mirrors. These flat mirrors are equally spaced with twice the linear size of the output pupils. A second relay mirror which 'sees' this linearly remapped pupil then forms the corresponding white-light interferogram on the entrance slit of a spectrograph. The dispersed fringes at the output image plane of the spectrograph are then recorded by a 2D detector with X-axis along the wavelength dispersion and Y-axis along the sky direction (Figure 6.12).

The equal spacing of output pupils results, however, in equal fringe periods. But the problem of spatial frequency confusion in the power spectrum of dispersed interferograms is avoided by maintaining arbitrarily fixed optical pathlength differences between pairs of telescopes. Details of this pupil/optical pathlength difference resampling can be found in Vakili & Koechlin (1989). Finally, if we assume 6 pixels for correctly sampling the fringes with the shortest period, we need roughly 150 pixels along the Y-axis to cover the central

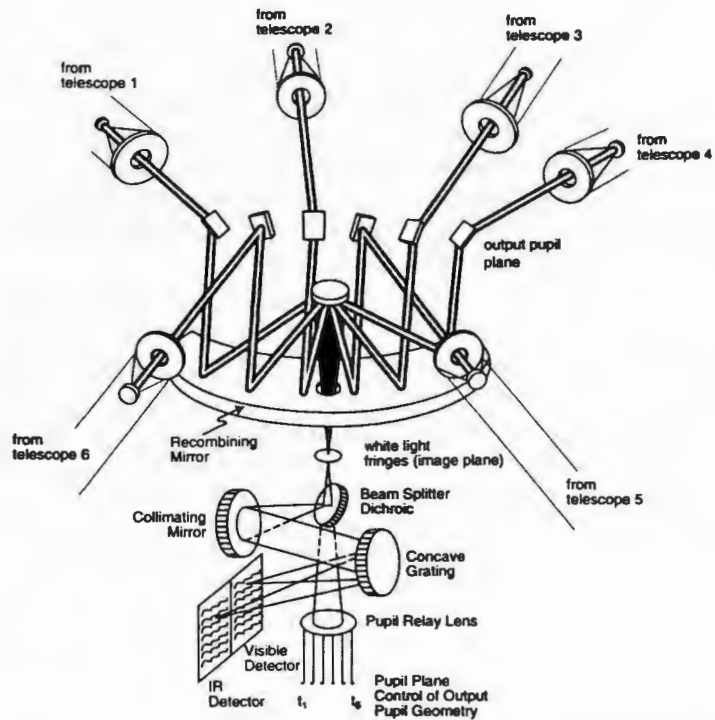


Fig. 6.11 Schematic view of the focal plane instrument used for both reference star fringe tracking and target spectral visibility measurement. The 6 output pupils are remapped linearly and maintained in the same plane by the longitudinal displacement of 6 field telescopes. The white-light fringe pattern is focused by the recombining telescope at the entrance slit of a spectrometer which forms spatio-spectral fringes on two-dimensional visible and IR detectors.

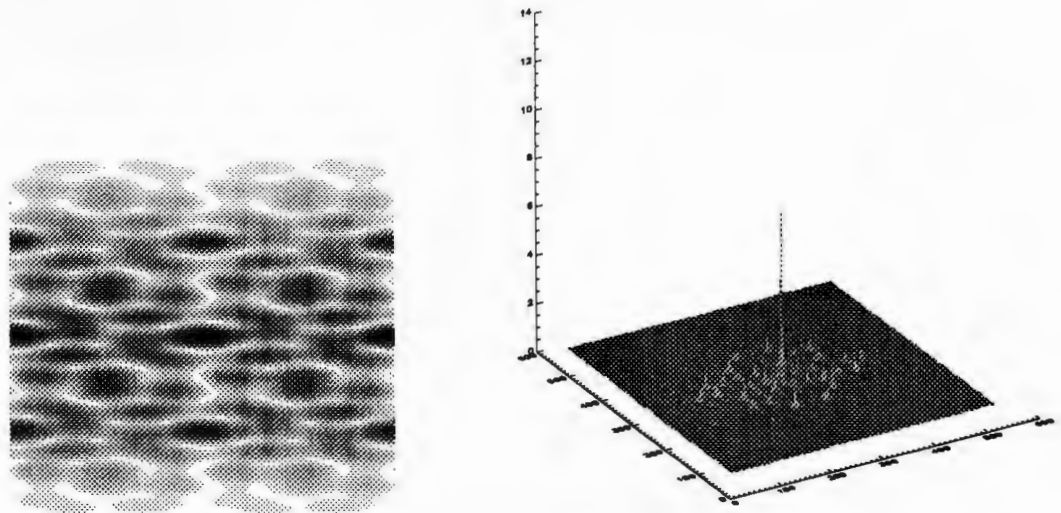


Fig. 6.12 Simulated spatio-spectral interferogram (left) and spatio-spectral MTF (right) for the proposed focal plane instrument where the position of 15 fringe peaks provide the optical path difference for each subaperture in the array,

lobe of the recombined Airy disks from individual telescopes. This requires a large number of pixels (150x20000), but is likely to be attained within the time scale of the program. Alternatively, a mosaic of different detector types adapted to the spectral regions of interest (CCD, NICMOS, APD arrays) could also be envisaged.

6.5. Summary of basic parameters selection

In summary, our selection of the basic instrumental parameters and the key reasons behind it are shown in Table 6.2.

Table 6.2 Summary of main parameter selection

Parameter	Selection	Main reason
Number of subapertures	6	<i>uv</i> coverage phase closure
Subaperture size	1 m	unresolved reference star (18.5 mag) full field (Airy disk) mapping
Optical pathlength control	reference star	
Beam recombining mode	cophased (goal) coherent (backup)	best signal to noise
Beam superposition	with pointing star (FF) with reference star (moon)	control bandpass
Calibratable fringe visibility loss	<20%	signal to noise
Fringe visibility uncertainty	<3%	imaging fidelity
Array configuration	moon: Y (non redundant) FF: circular (non redundant)	<i>uv</i> coverage
Spectral coverage	0.5 μm to 12 μm	Optics quality (visible) Passive cooling to 70K
Beam recombination	Michelson	Detector size limitation
Beam transfer	40 cm dia spectrally multiplexed (FF) dual beam with metrology (moon)	diffraction at longest baseline common path
Field	Airy disk of unit telescopes	source confusion detector size
Optical pathlength equalization	FF: orientable cluster Moon: delay line	optical simplicity moving telescope difficult

References

- Beckers J.M., "Field of view considerations for telescope arrays" SPIE proceedings (1986)
- Faucherre M. et al., "Beam combination in aperture synthesis from space: field of view limitations and (u,v) plane coverage optimization" SPIE proceedings (1989)
- Faucherre M. et al., "Michelson versus Fizeau type beam combination: is there a difference?" SPIE proceedings (1990)
- Harvey J.E. et al., "A parametric study of various synthetic aperture telescope configurations for coherent imaging applications" SPIE proceedings (1986)
- Koechlin L. et al., "Fringe tracking with the GI2T", Appl. Optics, in press, 1996.
- Koechlin L. et al., Applied Optics, under press 1995.
- Kulkarni S.R., P-Y Bély, M. Colavita, A.B. DeCou, D.L. Jones, J.H. Krolik, C.D. Martin, H.A. McAlister, J.P. McGuire, T. Nakajima, X. Pan, S. Phinney, M. Shao, J.W. Yu, *SSI: Separated Spacecraft Interferometry*, Proposal to NASA Res. Ann. 94-15, 1994.
- Pearson and Readhead, Ann Rev Astron Astrophys., 1984.
- Roddier and Lena Journal of Optics (Paris), vol 15, p171-182, p363-374, 1984.
- Shao M. et al., Astron. Astrophys. 193, 357-371, 1988
- Spagna, A., Lattanzi, M.G., et al. 1996, A& A, in press.
- Vakili F., Koechlin L., SPIE Vol. 1130, 1989, page 109

MOON-BASED VERSION

Although a number of optical interferometers have been proposed for the moon, they have never been pushed beyond the conceptual level. This is the first engineering study that has been performed. It shows that the moon is not the ideal site it was thought to be, and that an automatic deployment of such a major facility would be very difficult.

7.1. Introduction

The general arrangement of the six-telescope moon based interferometer is shown in Figure 7.1. In addition to six telescopes, it includes a central hub for the collection and interference of light, five movable carts equipped with mirrors, and ten fixed mirror units which are used to balance the optical path between telescopes for any particular observation. The observatory is arranged in a 'Y' configuration tilted a few degrees away from the North/South direction with two telescopes in each arm. Carts with attached mirrors, which can be moved from one observation to the next, have been selected as a mass efficient way of establishing optical paths between telescopes and the hub.

Independent traction systems for the carts are preferred over railed systems owing to the very large mass penalty that is involved for a 5 km baseline interferometer. The observatory is envisaged deployed between the equator and 45 degree latitude. This provides good uv plane coverage with ease of landing and site selection and the potential for future astronaut support. Candidate sites are: Riccioli (2.5S, 83W), Mare Crisium (18N, 60E), Mare Imbrium (40N, 4.4W), Tycho (45S, 10W). Of these Riccioli appears the most attractive since, in order to minimize the influence of straylight caused by the earth, it is better to be as near to the lunar horizon as possible. The telescopes have been designed to be fixed, but the option exists to equip them with traction systems to allow reconfiguration of the observatory in the future.

The observatory will be operated only during the lunar night. The observation philosophy is to observe a set of about 20 objects over the period of an earth day as they start rising above the horizon, and then again for the next 14 earth days as the moon rotates and the baselines change. The observatory would then be shut down during the lunar day because of heat and high level of straylight. The total time used in target acquisition, cart movement and optical path length control for a typical target measurement period of one hour is estimated to be between 120 seconds and 1000 seconds depending on the initial offset from the desired position.

Studies of the lunar environment have shown that time-varying tides of the lunar surface result in relative vertical movement between telescopes of 2.3 nanometer per second. In addition, the very low attenuation of the lunar ground to seismic vibration and micrometeorite impact shocks results in a significant background level. As a result, the interferometer cannot be operated in a "passive" mode, and the optical pathlengths between each telescope and

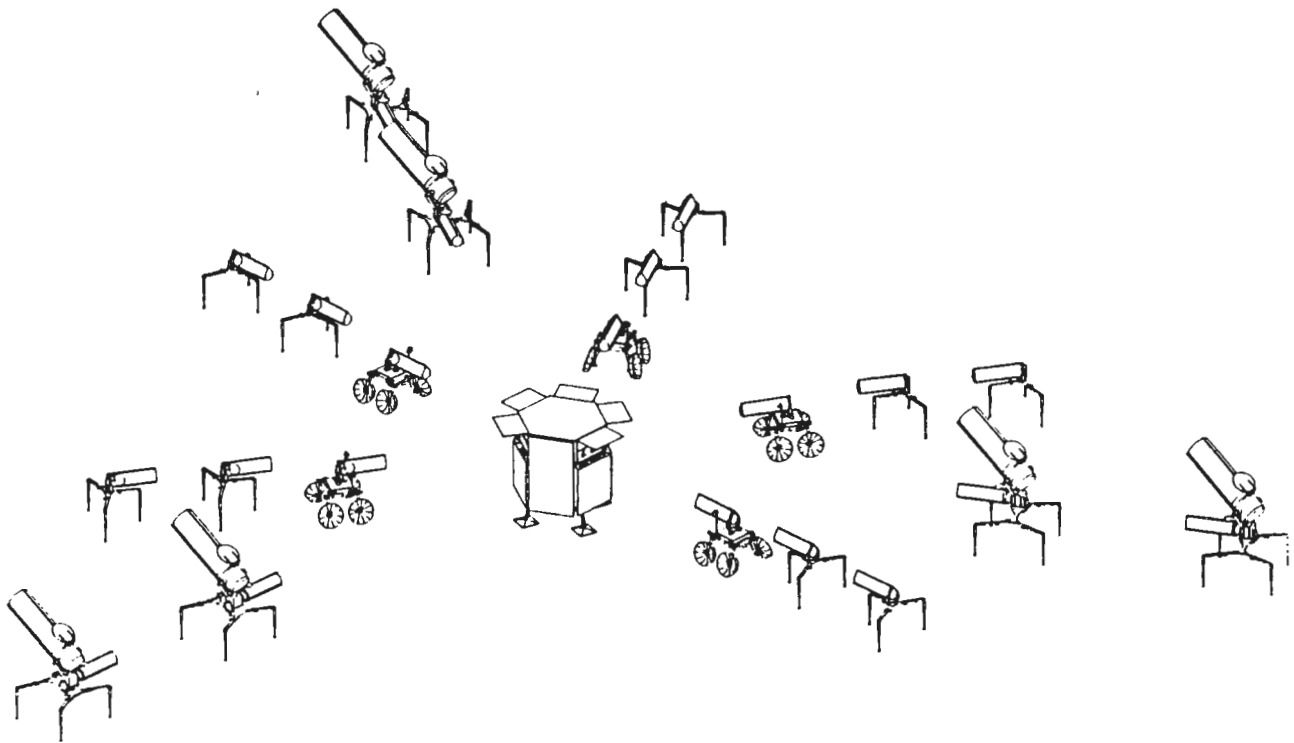


Fig. 7.1 General arrangement of the 6 telescope array (not to scale). The telescopes are the larger elements arranged in a Y configuration and shown with their 2 meter long baffles deployed. The 5 sets of 2 fixed and one mobile smaller telescopes constitute the delay lines systems.

the recombining hub must be actively controlled by means of a reference star and accelerometers.

7.2. Optics

A diagram of the telescope optics is shown in Figure 7.2. Each telescope has a primary mirror ($f/1$) with an aperture of 1m and an $f/30$ secondary mirror which provides a Coudé focus with a field scale of 1 arcmin = 8.7 mm. Two of the coudé train folding mirrors are driven as the telescope in its altitude-azimuth mount is tracking the target. The azimuth and elevation axes are fitted with angle encoders with 0.1 arcsecond accuracy.

A retroreflector with a diameter of 10 mm is positioned at the center of the secondary mirror to return the laser metrology beams back to the hub optics. The distance between the secondary and primary mirrors is not monitored by the laser system, but the telescope tube is constructed from low expansion material and as all telescopes will be subjected to similar temperatures during operation in lunar night the optical pathlengths errors between them will be largely compensated. A deployable baffle of 3m in length and an aperture cover are fitted to minimize stray and scattered light and the entry of dust. Operation of the observatory is limited to lunar night because of the high levels of straylight during lunar day.

The light beams from the target and a reference star are separated at the focal plane and follow distinct paths to the hub. The laser metrology system measures both the target and reference star paths and any difference between

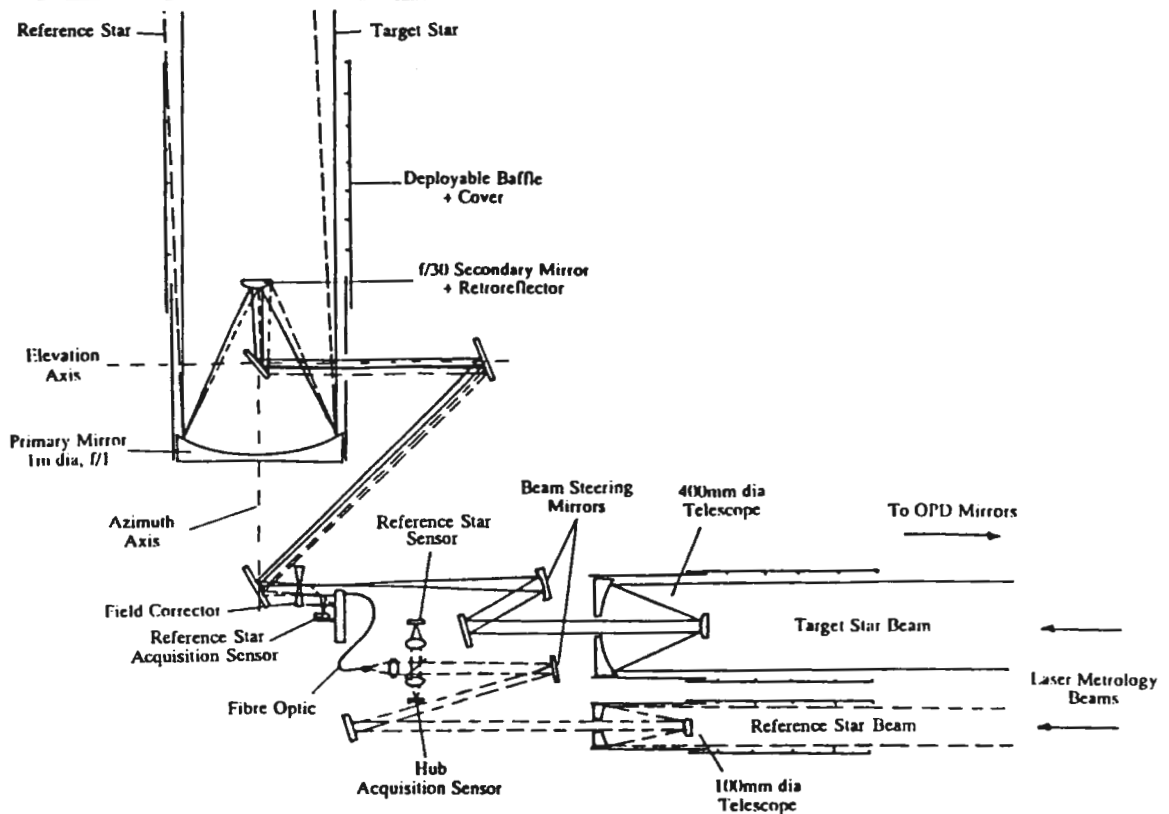


Fig. 7.2 Telescope optics

them will be immediately detected and corrected. Light from the target passes through a hole in the field corrector at the focal plane of the telescope. It is then steered via two mirrors to a 400 mm diameter Cassegrain telescope which collimates the beam towards the hub. The reference star light is off axis and the telescope aberrations are nulled by the field corrector before the light enters a single mode optical fiber positioned by a mechanism. The fiber is about 200 mm long and allows the light to be directed via a collimating lens to a 100 mm diameter Cassegrain telescope. Sensors may be used to check the reference star at the focal plane of the telescope or at the output of the fiber. The hub acquisition sensor detects the light from an LED beacon in the hub optics for the purpose of aligning the transfer telescopes with those of the hub. Similarly there is a beacon on the telescope so that the hub receiving optics may be aligned with the transmitting telescope.

The optical arrangement of the hub optics is shown in Figure 7.3. For clarity, only two incoming beams are shown. Each channel is equipped with a variable delay line, a vernier delay line and a reference star fringe tracker. The target fringe sensor receives all telescope beams simultaneously.

Each set of transfer optics consists of a 400 mm diameter Cassegrain telescope for the target and a 100 mm diameter telescope for the reference star. Fine steering of the beam telescopes is achieved by tilting the fold mirrors. Field stops at the focal planes are employed to minimize straylight and to limit the field of view of the receiving telescope to the aperture of the transmitting telescopes.

The LED beacon and telescope acquisition sensor in each arm are accessed via a flip mirror and are located at the focal plane of the reference star telescope. The sensor may also be used for autoguiding on the star using a beam

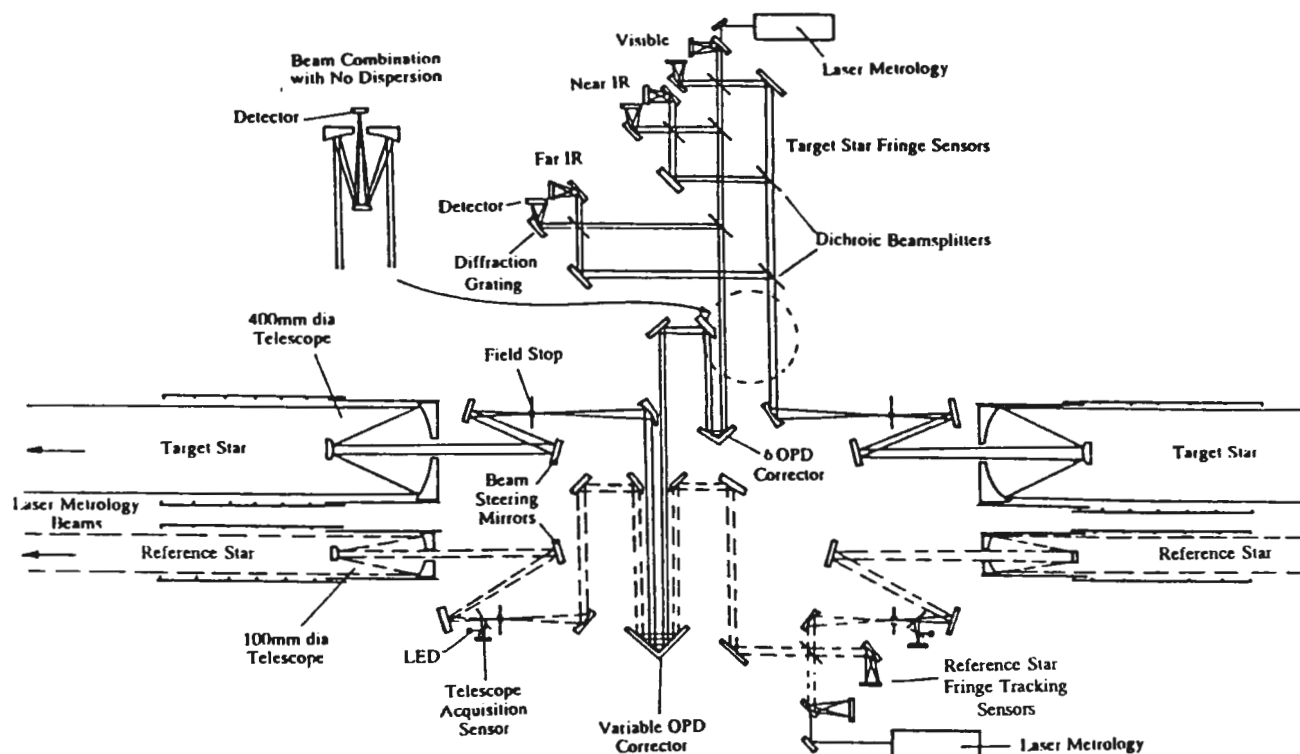


Fig. 7.3 Hub optics

splitter. Separate beams from a pair of telescopes may be combined using a beamsplitter or they may be brought to a common focus using a mirror system. The beamsplitter is more versatile as the beams may be combined at any angle (and hence fringe spacing) rather than at a fixed angle as with the focusing version. The wavebands are separated with dichroic beamsplitters prior to beam combination. The wavebands baselined for engineering analysis of the interferometer are shown in Table 7.1.

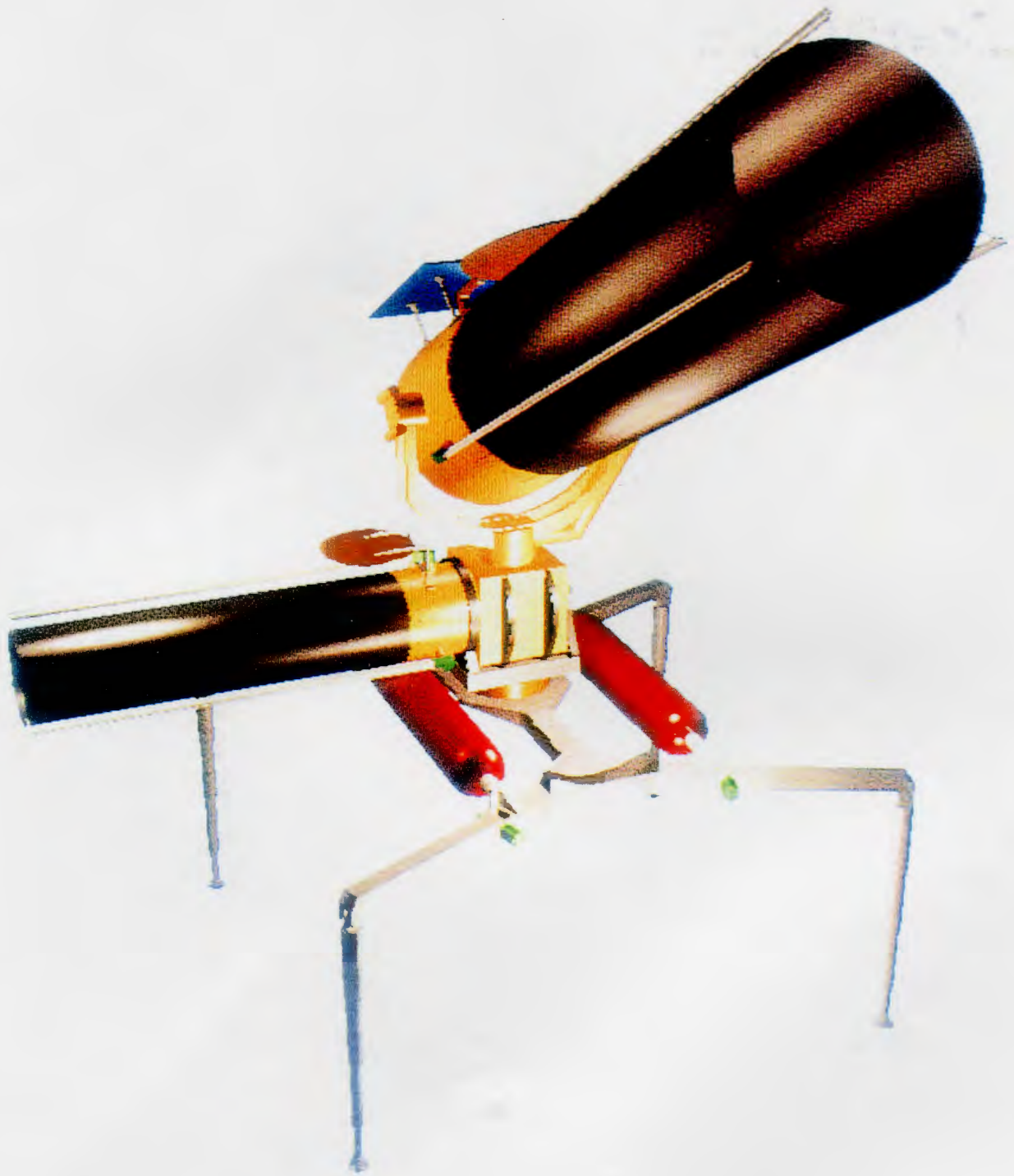
Table 7.1 Waveband allocation

Waveband	Function
400 - 600nm	Reference star
633nm	Laser metrology
1 μm - 12 μm	Target

The transmission achieved by the moon-based interferometer for target and reference stars are shown in Table 7.2.

Table 7.2 System transmittance

Wavelength (μm)	Target			Reference star
	1	5	10	0.5
Telescope transmittance	0.784	0.873	0.954	0.375
Delay line transmittance (average)	0.815	0.877	0.903	0.670
Hub transmittance	0.577	0.672	0.844	0.424
System Transmittance	0.369	0.514	0.727	0.107



View of one of the telescope units of the moon-based interferometer. The main 1-meter diameter telescope is shielded against earth straylight by a 2-meter long baffle. The transfer telescope relaying the beam to the recombining hub is on the left.

7.3. Array configuration

We have investigated the uv -plane coverage obtained with moon rotation for three array configurations: a Cornwell array, a Mills cross and a 'Y' configuration. We studied the effect of source declination and geographic latitude of the site on the moon. The performance of the three configurations are similar, but a 'Y' configuration with one branch slightly tilted with respect to the North-South axis gives better results overall. The array configuration and the uv -plane coverage for an equatorial site are shown in Figure 7.4.

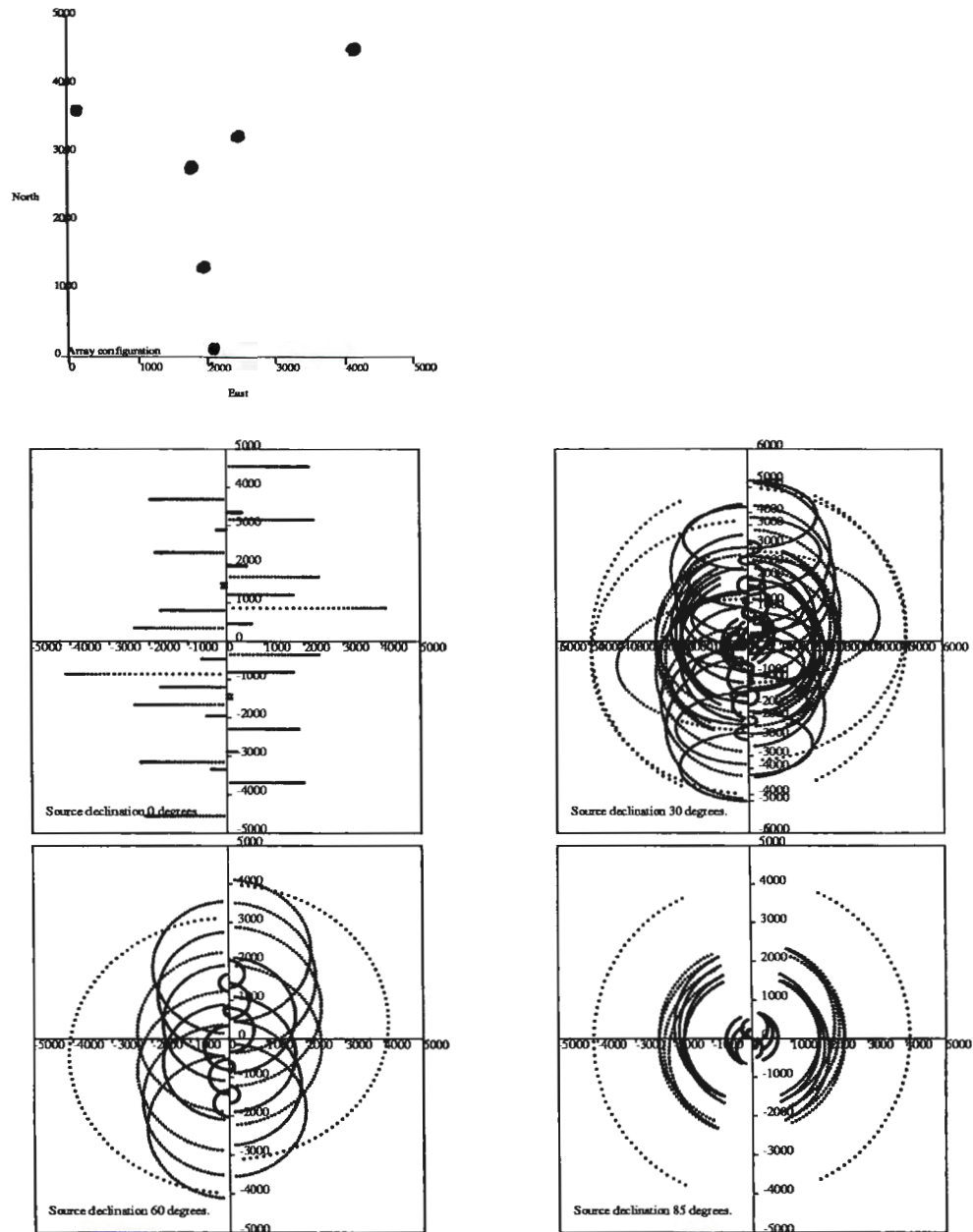


Fig. 7.4 Arrangement of the subapertures (top) and moon-rotational synthesis for sources at 0, 30, 60 and 85 degrees, assuming the observatory is at an equatorial site.

7.4. Optical path control systems

7.4.1 Moon seismicity

Lacking weather and with tectonic activity having largely, but not entirely ceased, the moon is a relatively quiet site seismically in comparison to Earth. Seismic activity on the moon is less than 10^{11} Joules per year, in comparison with about 10^{18} Joules on Earth. However, wave propagation losses are low on the Moon in comparison to the Earth. The average seismic Q is about 200, which is about the same as hard rock on Earth. As a result, seismic events and the resulting elastic "sounds" carry for long distances through the rock and regolith with great clarity.

The Apollo seismic network which was operated over a period of about 8 years identified three major sources of seismic activity: deep moonquakes, probably due to tidal effects, shallow moonquakes, possibly due to tectonic activity and meteor impacts (Lammlein, 1977, Nakamura, 1982).

As indicated in section 6.1.1, the tolerance on the optical path length within the observatory is about 22 nanometers (for observation at 1 micron). Such a level of disturbance can be created by a Richter 1.8 event occurring at 100 km.

Deep moonquakes appear to have Richter magnitudes ranging from 0.5 to 1.3 and should not therefore present a problem.

Shallow moonquakes can reach higher values, and would be a problem if they occurred within a surface distance of about 500 km. Such events occur only once every two years and should not thus be a problem either.

On the other hand, meteor impacts occurring within a few hundred meters are critical. Figure 7.5 shows the frequency (events per hour) per hour of critical (Richter 4) event as a function of distance. The frequency peaks at a radius of about 32 meters. On this basis, the average interval between critical events is about 10 seconds. Direct critical impacts on the instruments are also expected with a similar frequency. Since most exposures are on the order of one hour, one should therefore expect a large number of critical disturbances during observations.

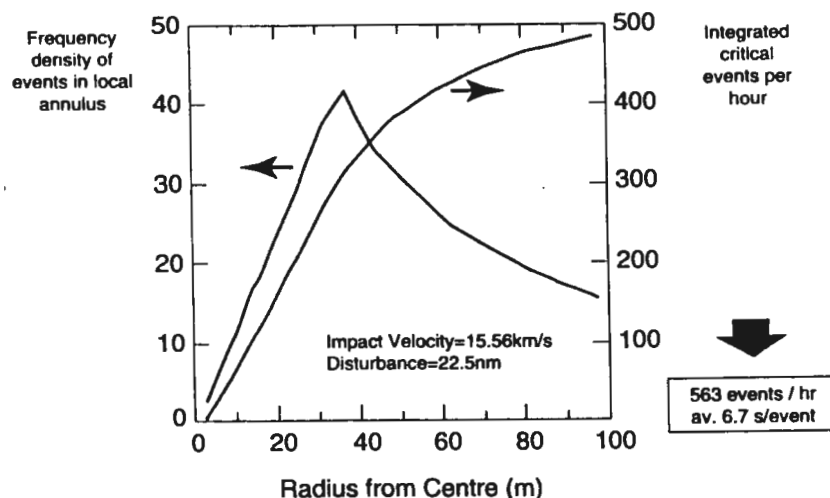


Fig. 7.5 Frequency of critical impact events as a function of distance.

7.4.2 High frequency control of the optical path

In addition to the seismic events described above there are a number of other disturbance sources which vary from completely deterministic to completely random. These include tidal flexure of the lunar surface, thermal creaks due to temperature variations and internal mechanical noise. All these events are likely to perturb the fringe tracking systems which have a fairly low band-pass. It is therefore essential that the optical path control system include a means of rejecting these disturbances.

This is achieved by the combined use of laser metrology, reference star measurements, and accelerometer sensing. Laser metrology is used to measure all line-of-sight disturbances throughout the optical path, while the reference star interferogram is used to control the position of the hub variable delay line. Reference star magnitudes of 18.5 mv are envisaged, and at least one would be expected in a 2.5 arc minute cone about the target. Typically 1000 reference star photons are collected by the interferometer within a 10 second period. Accelerometers are needed to measure all high frequency components not covered by the reference star and laser metrology.

The laser metrology measures the optical path by means of a beam which is introduced at a small port near the beam combiner and which travels all the way to the retroreflectors mounted on the main telescope secondary mirrors and back. Separate lasers are used for the target and reference star paths. The laser metrology system must monitor the 5 km long optical paths to nanometer accuracy at a repetition rate of 1 kHz. Such a laser ranging system detects changes in optical length along the target and reference star beam path, but does not measure vertical or sideways motion of the telescopes which will change the phase of the incoming target. This 'external path length' is measured by the use of a reference star and accelerometers.

7.4.3 Delay lines

As explained in section 6.1, with fixed telescopes, delay lines must be used to adjust the optical path between each telescope and the recombining hub as a function of the initial target coordinates and to compensate for moon rotation. Out of the six telescopes the light from one can be fed directly, but the five others need a delay line. These delay lines are of a length comparable to the baseline in order to permit the observation of targets close to the horizon.

This is accomplished in two layers, a coarse, long throw and step operated, delay line system deployed on the lunar surface, and a fine and continuously operated delay line in the recombining hub. For the long throw delay line, we investigated two schemes, a fixed mirror systems in arithmetic and geometric series, and a system using mobile delay line carts. We have selected the mobile delay line carts solution because of its smaller number of mirrors and the corresponding savings in transport and deployment costs. Five mobile carts and ten fixed mirrors are required with additional access mirrors incorporated into the hub to select optical paths.

Finally, the difference in optical path length between the reference star and the target is compensated by a set of 5 delay lines which are located in the hub.

Each delay line system consists of:

- two fixed range mirrors at 625 m and 1250 m from the hub,
- one mirror on each mobile delay line cart, range 1 to 625m, step size 2.5 m,

one variable delay line inside the hub, stroke 2.5 m, resolution 1 nm,
 one target/reference star delay line inside the hub, stroke 2.5 m, resolution 1 nm,
 a mirror interface assembly in the hub consisting of 4 switching mirrors.

7.4.4 Computer simulation

A computer simulation of the optical path length control system has been carried out in order to evaluate its performance and verify that the specified tolerances on optical path length could be met. The results are shown in Table 7.3. The net 11.4 nm 1- σ error in optical path length is within the requirement of 22.7 nm.

Table 7.3 Control System Error Budget

Parameter	Value	Contribution to optical path error (nm)
Variable delay line noise	10 nm	6.5
Seismic disturbance noise ensemble	22nm at 15 rads/s	1
Telescope mech/thermal noise (psd)	$2.5 \cdot 10^{-17} \text{ (m/s}^2\text{)}^2/\text{Hz}$	1
Laser metrology noise	3 nm	3
Lunar bulge	100 m low frequency sinusoid	2.5
Accelerometer noise (psd)	$7 \cdot 10^{-22} \text{ (m/s}^2\text{)}^2/\text{Hz}$	< 1
Reference star measurement noise	10 nm (1- σ)	10
Total (root square sum)		11.4

7.5. Overall Observatory Design

The baseline design of the various system elements is driven largely by the constraints of launch and delivery and the method of deployment to be adopted on the lunar surface. In order to accommodate sufficient equipment to implement the 6 telescope version of the interferometer, two landers are required. In this way it is also possible to achieve partial mission redundancy such that loss of the second lander will still leave sufficient equipment available on the first lander for a two telescope configuration to be established. The payload split between Lander 1 and 2 is defined in Table 7.4.

Table 7.4 Payload Split between Lander 1 and 2.

Lander 1	Lander 2
2 Fixed Telescope Assemblies	4 Fixed Telescope Assemblies
2 delay line carts	3 delay line carts
2 Fixed range mirrors	8 Fixed range mirrors
1 Movable mirror	4 Movable mirrors
5 Mirror interface assemblies (in hub)	Main power
Hub	Avionics, etc
Avionics, etc.	Payload deployment equipment

A schematic view of Lander 1 is shown in Figure 7.6.

Each telescope is integrated into a single payload suitable for transportation to its dispersal position by the delay line cart. A Regenerative Fuel Cell (RFC) is incorporated into the assembly to provide power to the azimuth/elevation mechanisms. The telescope is mounted on an interface and

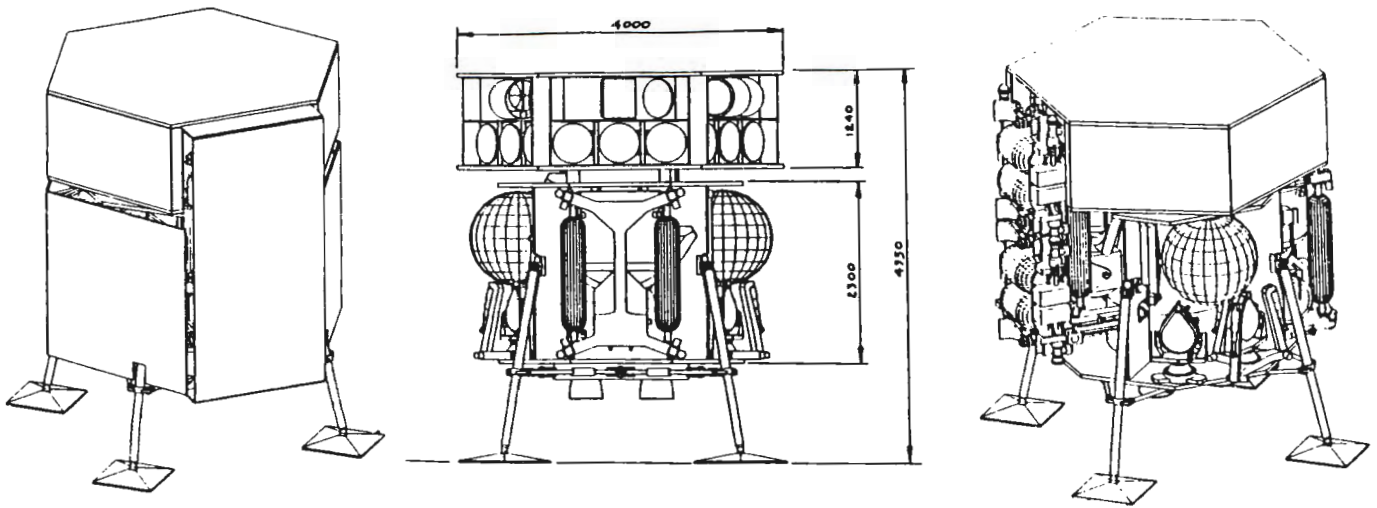


Fig. 7.6 Lander 1 on landing and showing stowed payload.

support platform and is equipped with a set of deployable legs capable of lifting the telescope clear of the delay line cart when the dispersal position has been reached.

The fixed range mirrors system are shown in Figure 7.8. They are put in position by the delay line cart and aligned with power fed via a detachable umbilical.

The movable delay line mirrors are similar to the fixed range mirrors, but do not incorporate any Support Assembly since they are intended to remain latched to the delay line carts during interferometer operation. The delay line cart with mirror in place is shown in Figure 7.8.

Whether the observatory is deployed automatically or with astronaut assistance, the delay line carts are used as a rover for the installation of all of the observatory elements. The basic delay line cart has been sized to carry the fixed range mirrors and cart-mounted mirrors. In order to cope with the much larger telescopes, two of these vehicles are used, joined longitudinally by lock type couplings. Once all the telescopes are deployed, the carts are separated and used in conjunction with the three other vehicles for deployment of the fixed mirrors. This operation finished, the carts are loaded with the movable mirrors and deployed to their operational positions.

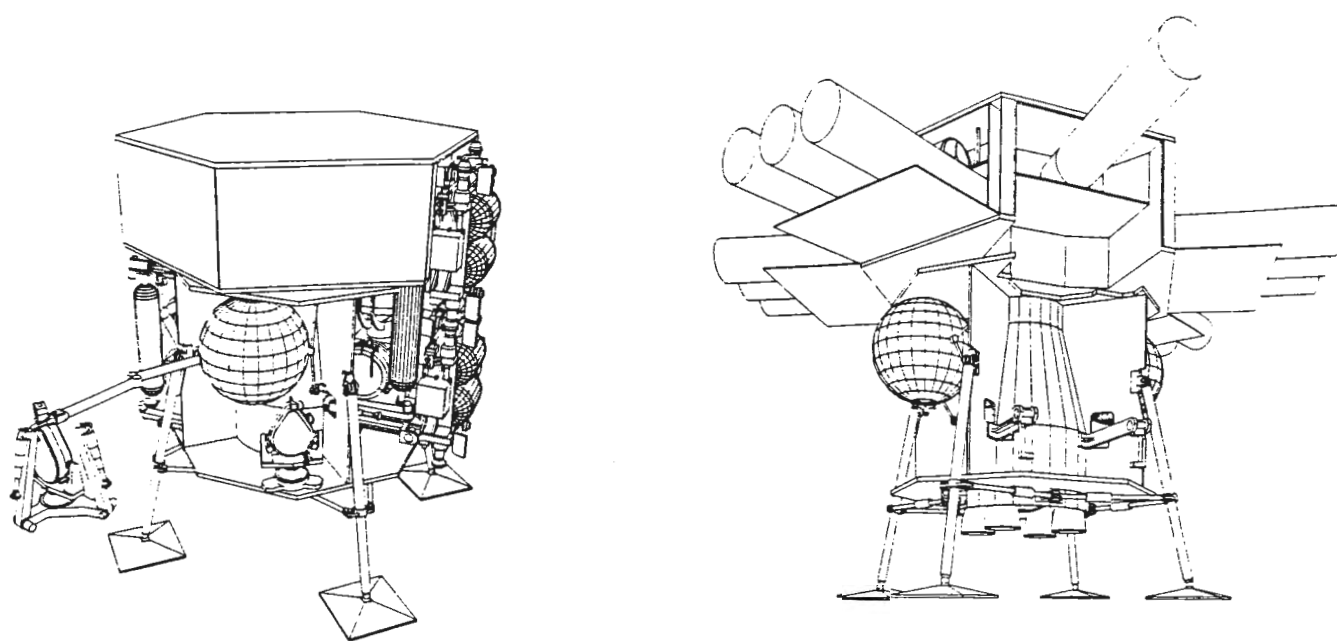


Fig. 7.7 Deployment of range mirror from lander (left) and operational configuration of the lander (right) shown without side panels.

Table 7.5 Lander 1 & 2 mass breakdown

Lander	Mass (kg)	Comment
Lander 1		
dry mass	1223	Dry margin 15%
payload mass	2162	Current Ariane maximum, 1763 kg
landed Mass	3486	
propellant	4064	81 kg residuals
launched mass	7530	
Lander 2		
dry mass	1223	Dry margin 15%
payload mass	2347	Current Ariane maximum, 1763 kg
landed mass	3652	
propellant	4064	81 kg residuals
launched mass	7716	

Table 7.6 Observatory Element Masses
with 20% contingency but excluding Landers).

Observatory element	Basic mass (kg)	Quantity	System mass (kg)
Hub (lander 1)	577.6	1	694
Hub (lander 2).	175.4	1	211
Hub mirror interface	50	5	302
Telescope	204.5	6	1472.4
Fixed Range Mirror	28.5	10	343
Delay line cart	227.7	5	1366
Installation Equipment	50	2	120

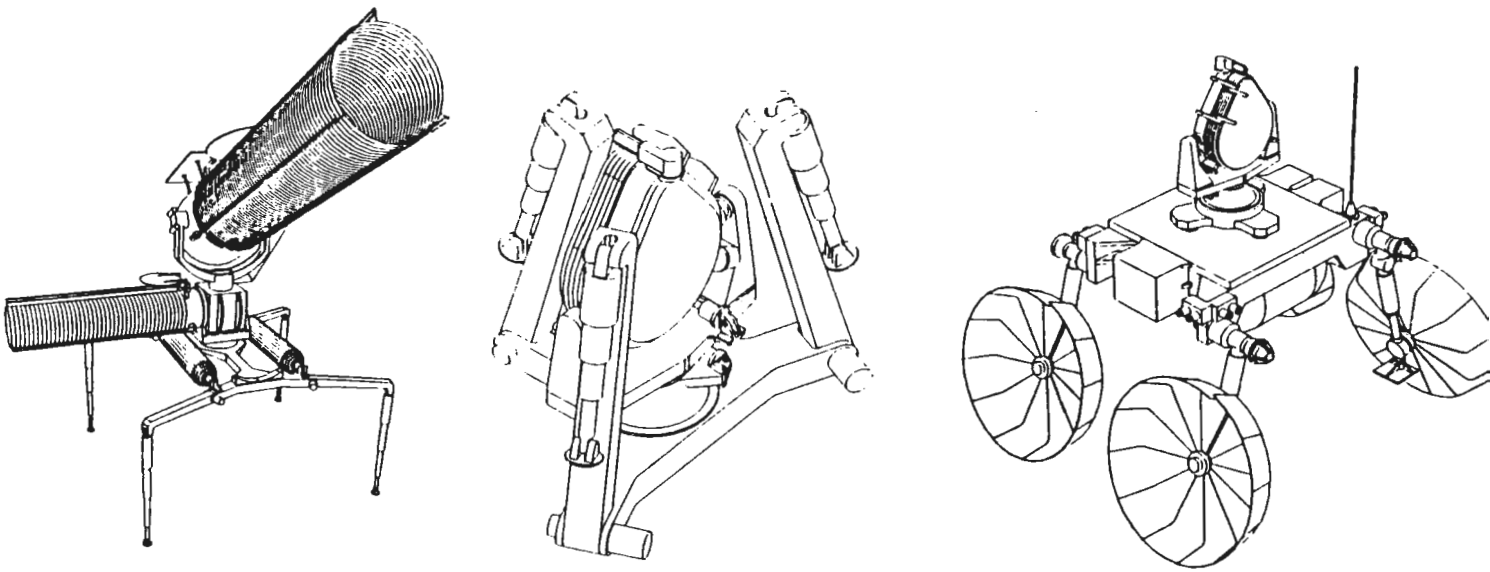


Fig. 7.8 Individual telescope (left), Fixed range mirror (middle) and Delay line cart with mirror in place (right).

7.6. Thermal Subsystem

During lunar night, the observatory is expected to reach temperature below 70K by passive means. Whereas the rate of change of temperature is high at the transition from day (400K) to night (100K), the temperature variation during lunar night is very small, on the order of milliKelvin per minute, which is very favorable for the stability of the optical trains.

The Landers have solar arrays on the sun-facing side which are insulated from the main body using multilayer insulation (MLI) and low conductance stand-offs. The remainder of the sun-side is covered in MLI with an outer layer of electrically conductive ITO Kapton to prevent build up of static charge and minimize dust adhesion. The radiators, avionics and fuel cells are located on the anti-sun side. Side radiators use UV reflective OSRs to minimize the effects of sun illumination at the start and end of the lunar day. Coupling to the lunar surface is also minimized by tilting the radiators and solar arrays. The underside and legs of the Landers are covered with MLI where possible.

The hub optics are decoupled from the Lander using low conductivity struts and stand-offs. The top of the hub has OSRs to provide a radiator for the interferometer optics. The delay line carts have zenith facing radiators to deal with motor and electrical dissipations, and insulation on the underside. Heaters may be required for the wheel motors if there are extended periods of inactivity. The observatory telescopes and fixed range mirrors have low emittance so additional high emittance radiators are required to achieve low temperatures quickly after sunset. This is achieved with zenith facing radiators which also minimize coupling to the lunar surface.

7.7. Power Subsystem

The power system has to supply power to the observatory during the lunar night of 14 earth days. The estimated average power requirements for the observatory are given in Table 7.7. Apart from nuclear power generators, the only mass efficient solution is to use Regenerative Fuel Cells (RFC). NiH batteries would be very heavy, around 4070 kg for the entire observatory while an RFC based power system is estimated at 450 kg.

Table 7.7 Average power requirements

Function/System	Night			Day		
	Load Watts	Duty Cycle %	Mean power Watts	Load Watts	Duty Cycle %	Mean power Watts
Lander/hub						
Common delay line	25	75	18.75	0		0
Ref star delay line	25	75	18.75	0		0
Avionics	55	100	55	45	100	45
Laser metrology	5	100	5	0		0
Communications	15	50	7.5	15	50	7.5
Focal Plane	8	100	7.5	15	50	7.5
Lander/hub reqmt	133		113	60		52.5
Delay line cart						
Electronics & data handling	15	100	15	5	100	5
Communications	15	50	7.5	15	50	7.5
Motor & control	75	67	50	75	0	0
Delay line cart reqmt	105		72.5	95		12.5
Telescope						
Electronics & data handling	15	100	15	5	100	5
Laser metrology	5	100	5	0		0
Communications	15	50	7.5	15	50	7.5
Pointing mechanisms	15	100	15	0		0
Telescope reqmt	50		42.5	20		12.5

The RFC system makes use of the propulsion hydrogen and oxygen tanks of the landers. Using GaAs cell technology the solar array sizes to support the limited lunar day operations and RFC recharging are 3 m² for the Lander/hub, 1.8 m² for the Delay line cart, and 1.1 m² for the telescope units.

The power system also include a discharge regulator to convert the fuel cell output voltage to the bus voltage, a charge regulator to control input to the Electrolyser Cell for regeneration and a solar array power regulator.

7.8. Communications and Data Management System

The Communications and Data Management System (CDMS) computer located in the hub carries out all normal operations of the recombining hub, including reconfiguration to redundant functions after fault detection. It also handles the top level control and monitoring of the telescopes and carts via a local communications net. The CDMS controls and monitors the hub subsystems using the on board data handling bus directly to the power distribution system, and other subsystems. A mass memory unit is used for the storage of interferograms in the absence of a ground link.

An Onboard Mission Control Unit carries out the ground station emulation function. It has direct access to the CDMS computer for monitoring and to the

telemetry / telecommand packets for monitoring and direct reconfiguration of the subsystem after a major fault.

The telescope and cart block systems are similar to that for the hub except that fewer functions are carried out.

The nominal telemetry requirement of the observatory is estimated at 20kbps which is easily managed by an S-band link via a 0.5m parabolic dish working into a 15m ESA ground station.

7.9. Launch and Delivery

The largest present payload mass which can be deliverable to the moon using Ariane 5 and a weak stability boundary transfer orbit is 1780kg. The future projected capability is shown in Figure 7.9, and shows a deliverable payload mass of 2200 kg for an 8500 kg LTO Ariane 5 launch mass in WSB. In the time scale of the mission it is assumed that some upgrades to the launch vehicle will have taken place, in addition to the use of the H-10 stage, resulting in a payload growth of about 330 kg for every 1000 kg increase in launch capability for the Ariane 5. This future capability is then not inconsistent with the current estimates of 2162 kg for Lander 1 and 2347 kg for Lander 2 given some redistribution of equipment between the Landers and future mass reduction exercises.

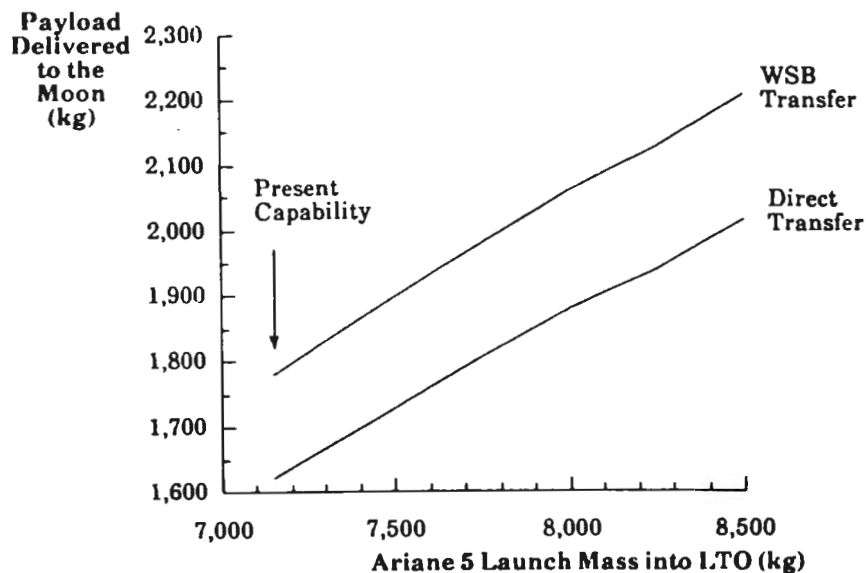


Fig. 7.9 Variation in Delivered Payload with Ariane 5 Launch Mass.

7.9.1 Mission observing program

The observing parameters for the typical targets of our strawman mission are shown in Table 7.8. The observing time and mission completion rate have been determined with the following assumptions:

- . optical throughput based on 15 reflections and 0.9 reflectivity
- . detector quantum efficiency of 0.95
- . main optics at 80 K and emissivity of 0.10
- . interferometric efficiency (ratio of actual fringe visibility to theoretical value) $\eta = 0.8$
- . during of the mission: 12 years
- . scheduling efficiency: 45% (no daytime observing)
- . delay line setup time per reconfiguration: 1/2 hour
- . telescope pointing per configuration: 1/2 hour
- . reference star and target acquisition: 1 hour

Table 7.8 Mission completion

Target	Max baseline (m)	Number config.	Coherence time (hrs)	Observ. duration (hrs)	Number observ.	% mission
Star disc	850	1	11.1	13.1	100	2.8
Supermass binar	5672	0	1.4	0.0	100	0.0
Star surface - active	1443	8	1.9	31.1	100	6.6
Star surface - convec	5672	1	17.5	19.5	30	1.2
Star surface - solar	3609	31	0.6	80.7	50	8.5
Star surface - magnet	825	5	3.9	29.3	50	3.1
Dust Shells	240	4	3.2	20.8	200	8.8
YSO Jet	1602	4	3.8	23.3	200	9.9
YSO disc	3060	4	7.5	38.1	100	8.1
Globular Cluster	60	1	11.6	13.6	100	2.9
Galactic center	655	3	4.7	20.1	40	1.7
Cepheids	5775	5	2.5	22.4	250	11.8
Contact binaries	4812	5	3.9	29.3	100	6.2
Cataclysmic binaries	3781	1	17.4	19.4	100	4.1
Gal Gravit. Lenses	1831	1	1.6	3.6	500	3.8
AGN BLR	2268	2	10.8	25.5	50	2.7
Extr. Gal. SN	2836	1	15.8	17.8	200	7.5
Subst Grav. Lenses	726	1	14.8	16.8	150	5.3
Grav Waves	567	2	6.8	17.6	100	3.7

References

- Lammlein, D.R. "Lunar Seismicity and Tectonics", *Phys. of the Earth and Planetary Interiors*, **14**, p 224, 1977.
- Nakamura Y., G.V. Latham and H.J. Dorman, "Apollo lunar seismic experiment - Final summary", *J. Geophys. Research* **87** (Supplement), p A117, 1982.

FREE-FLYER VERSION

Although free-flying spacecraft interferometers have been proposed since at least the early 1980's, cophasing a large constellation has always been considered problematic. Our study shows that by combining a low disturbance orbit, microlevel thrusters, laser intra-spacecraft metrology and large enough apertures to use distant, unresolved reference stars for array cophasing, a free-flying interferometer can realistically be considered feasible with current technology.

In what follows we describe a possible implementation for the free-flyer version. It does not claim to be a definitive design, but is based on technical know-how and preliminary calculations sufficient to ascertain feasibility. We refer the reader to chapter 6 for justification of the selection of the main parameters and to the Matra Marconi Space study report for further engineering details.

8.1. Orbit

An extremely low disturbance orbit is a key ingredient of the free-flyer solution. Fuel economical array reconfiguration and station keeping during observations require that the cluster be sited on an orbit where the gravity gradient is very small. In addition, the observed sky field must be continuously visible during the full observing time which typically lasts several hours. These two conditions exclude low earth orbits. Among higher orbits such as a high geocentric orbit as selected for LISA orbit or the libration points of the earth-moon or sun-earth systems, a halo orbit close to the second Lagrange point of the sun-earth system offers the most advantage. Such an orbit,

- benefits from a very low gravity gradient (the Lagrange points are quasi equilibrium points in space where the gravity gradient is at a minimum),
- offers continuous visibility of a large portion of the sky,
- is located at a relatively short distance from Earth (0.01 AU or 1 500 000 km), thus minimizing orbit transfer energy and transit time,
- does not suffer from eclipses, which simplifies the power generation system, eliminates thermal shock and favors thermal homogeneity in general,
- minimizes straylight constraints since the sun, earth and moon are always in the same direction.

The best choice is an elliptic, $600\,000 \times 50\,000$ km, halo orbit around the L2 Lagrange point of the Sun-Earth system, symmetric to the SOHO orbit with respect to the Earth (Figure 8.1).

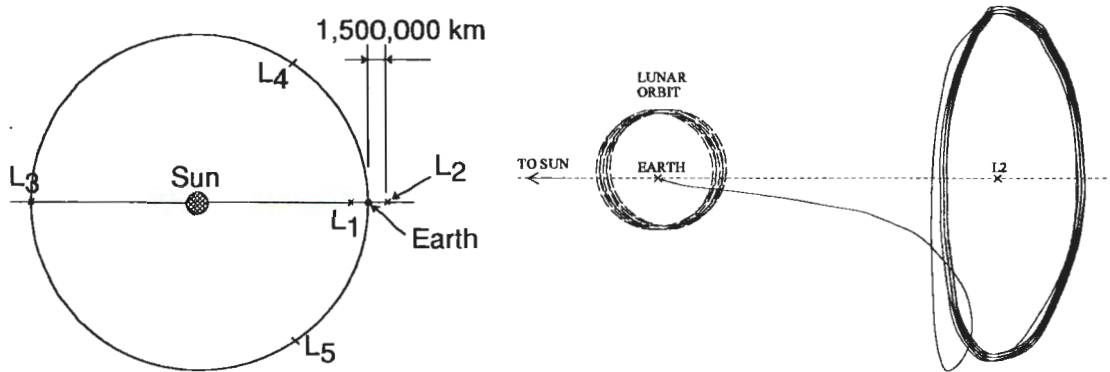


Fig. 8.1 The selected orbit is a halo orbit around the L2 point of the sun-earth system which offers a very low gravity gradient for fuel economy, as well as power generation, straylight and operational advantages

8.2. Array configuration

A powerful feature of the free-flying interferometer is its ability to be reconfigured to best match the mapping requirements of the observed source. It is indeed possible to adjust both the maximum baseline and the number of intermediary measuring points to optimize resolution and distribution of the visibility measurement points in the Fourier plane. This optimization should be done on a case by case basis but, as a rule, our strawman program indicates that the majority of targets requires uniform mapping. The instantaneous distribution of telescopes in the array and the nominal reconfiguration strategy should thus be designed to lead to an approximately uniform uv plane coverage.

The optimal distribution of sub-apertures for instantaneous uniform coverage of the uv-plane has been worked out by T. Cornwell (1988). In the case of a 6 element array, the angles are ± 39.7 , ± 8.2 , and ± 159.7 degrees.

Concerning reconfiguration strategy, fuel economy dictates that the telescopes be displaced continuously rather than in a stop and go fashion. To cover the uv-plane more or less uniformly, the radial expansion or contraction should thus be accomplished with a velocity varying as the inverse distance from the hub. Rotation of the array as a whole is a-priori not desirable technically. Not only is this fuel costly, especially at the longest baseline, but the reference star and pointing star pickoffs then have to be counter-rotated. Still, some rotation is very advantageous for uv-plane coverage in order to compensate for the small number of telescopes in the array. To reduce fuel consumption, the rotation rate should slow down as the expansion radius increases.

The distribution of subapertures and reconfiguration strategy which we have selected follow these principles and are shown in Figure 8.2. The expansion/contraction law is described later.

8.3. Optical design

8.3.1 General concept

The overall optical concept for the interferometric array is shown schematically in Figure 8.3. The six 1-meter telescopes in the array simultaneously observe the science target, a reference star and a pointing star. The reference star is an unresolved field star, typically of magnitude 18.5, which is used to cophase the array. The integration time required for the reference star is on the

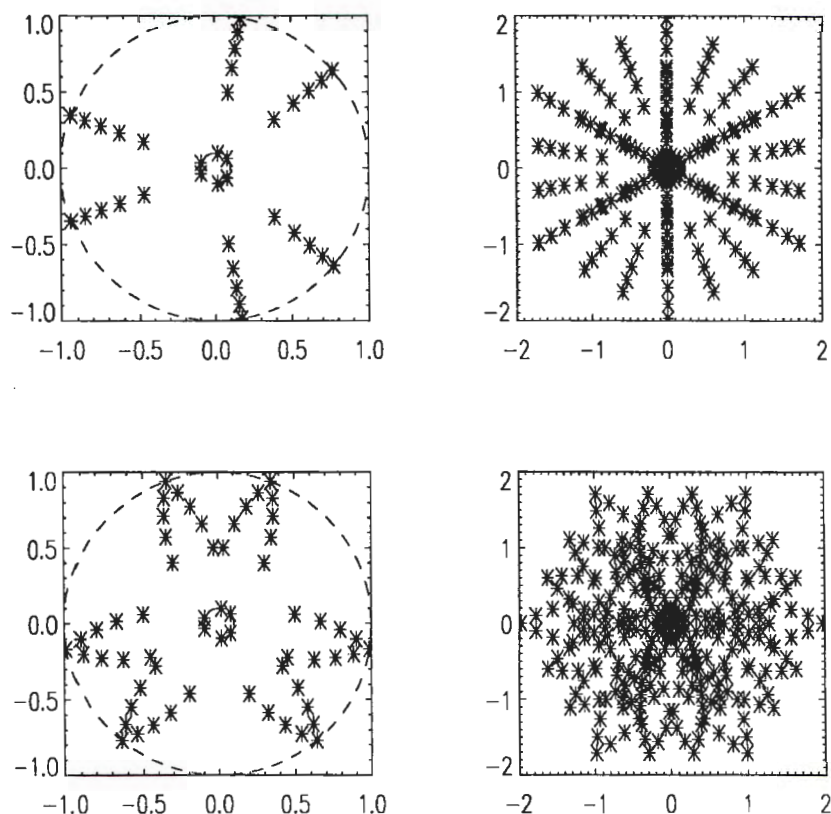


Fig. 8.2 Array configuration. The distribution of subapertures and the reconfiguration law are selected to lead to an approximately uniform Fourier plane coverage. Sub-apertures are distributed as per the Cornwell solution, and expanded and contracted with a velocity varying as the inverse distance to the hub. In the simplest scheme (top), the subapertures are moved only radially. The Fourier plane coverage can be significantly improved by rotating the overall array, for example by 60 degrees, (bottom), but at the expense of additional fuel consumption. This last strategy has been used for the mission baseline.

order of 10 seconds, which is too slow for pointing control. The pointing star is a brighter star, typically of magnitude 12, which will be used at a much higher refreshing rate to maintain the pointing of the telescopes and to coalign the six individual beams in the recombining hub. The reference star and pointing star are collected in the telescope's field of view (to within a 2.5 arcminute radius for the reference star, and a 15 arcminute radius for the pointing star) with movable off-axis pick-off mirrors.

Because any optical pathlength difference between the target and reference star will result in a phase error, both the reference and pointing star beams are made to follow the same path as the target beam as far as possible. The three beams are thus separated spectrally and collimated into a common 40 cm diameter beam for transfer to the recombining hub. Nominally, the reference star will use the 0.4/0.7 μm band, the pointing star the 0.7/0.8 μm band, and the target the 0.8/12 μm band (Figure 8.4). However, these bands are interchangeable (as explained in chapter 6, the reference star and the target are dispersed and analyzed on the same detector) and can be rearranged depending on the

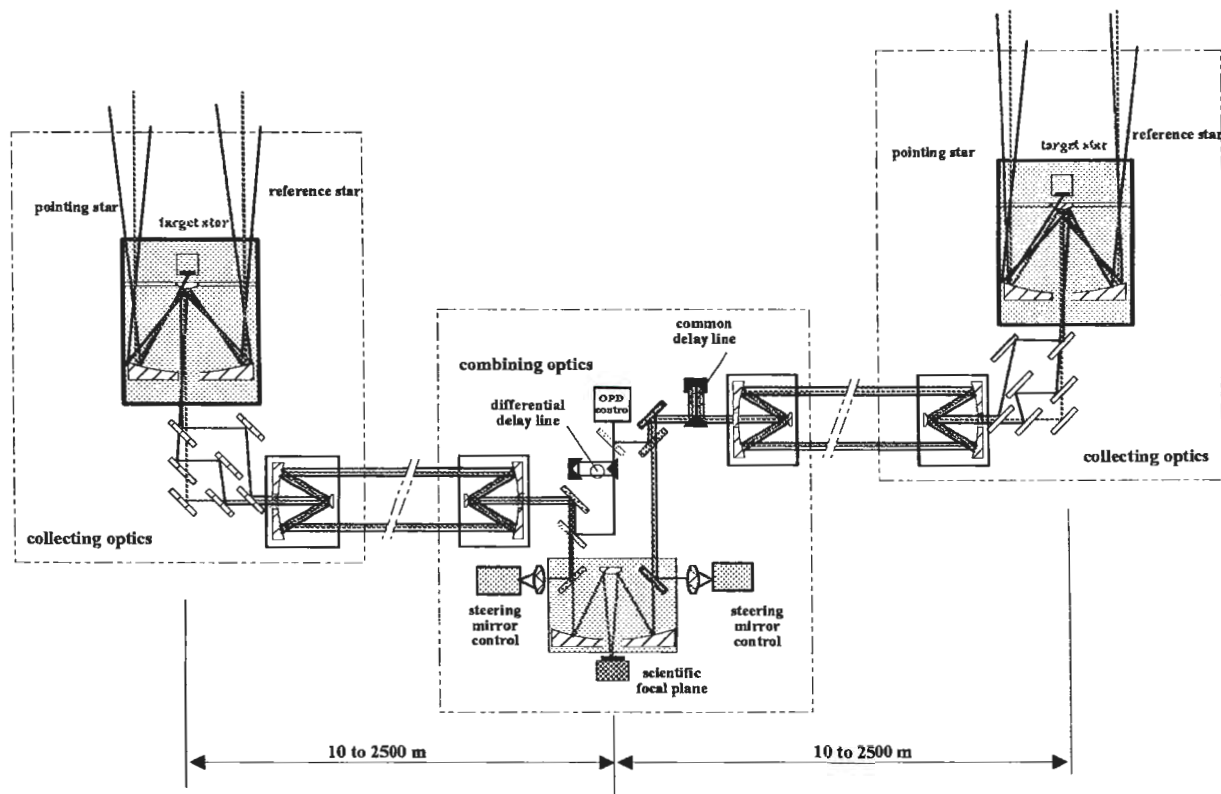


Fig. 8.3 Schematic optical diagram of the telescopes and recombining hub

science program. The beams are then directed towards the recombining hub. The corresponding pointing requirement is on the order of 0.2 arcsecond which is within the range of the attitude control system of the telescope spacecraft.

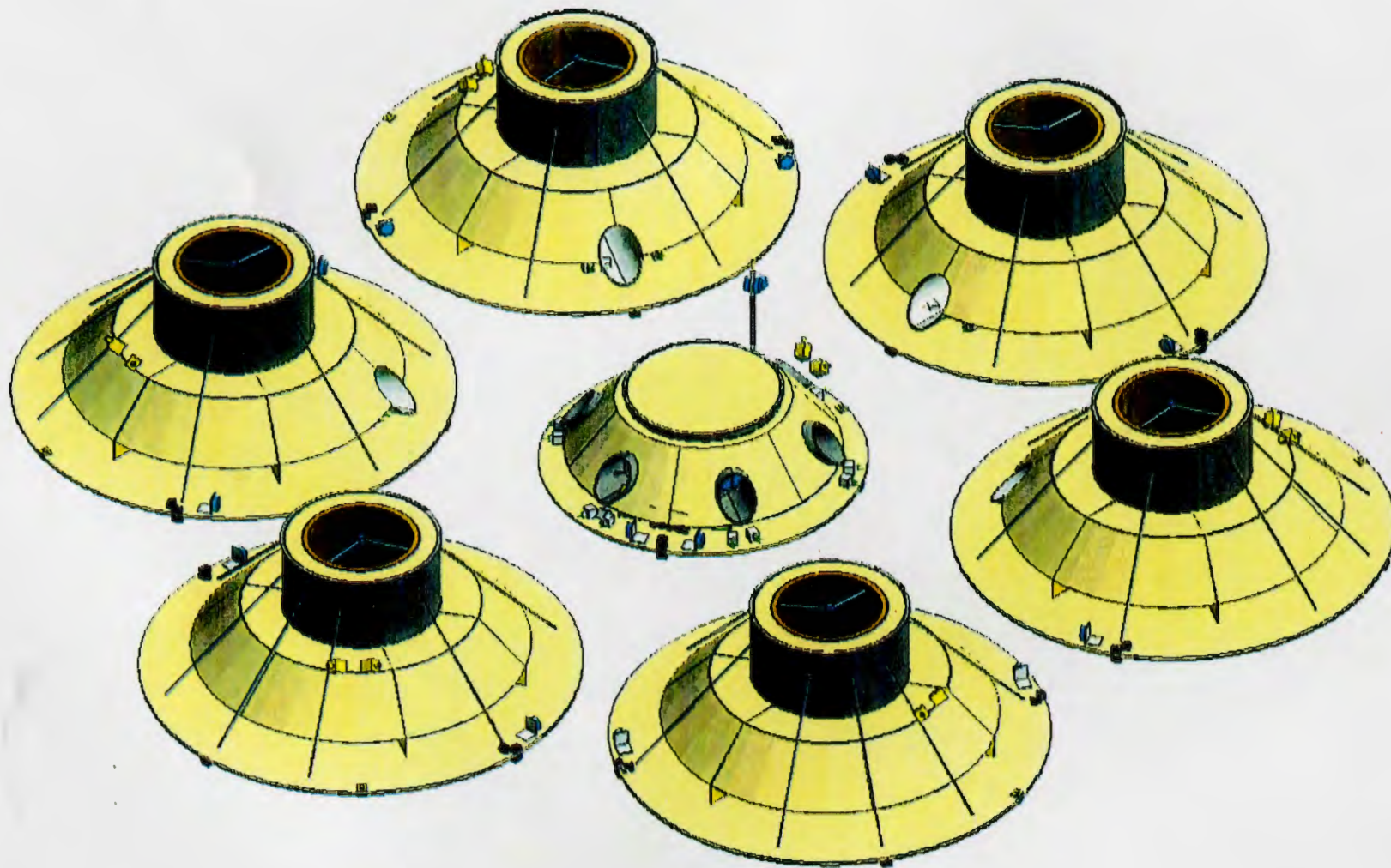
The beams coming from each of the 6 telescopes are collected inside the recombining hub with a 40 cm diameter Cassegrain unit and are demagnified so as to be more manageable. Each composite beam first goes through a common delay line which compensates for small optical pathlength differences that may exist between each of the telescopes in the array and the recombining hub. The three beams are then separated spectrally, with the pointing star beam being sent to a pointing analyzer and the reference star and target beams sent to a focal plane instrument. The reference star beam goes through an additional delay line which corrects for the differential optical pathlength between target and reference star.

The six incoming beams must be coaligned in the focal plane to a fraction (e.g. 1/10th) of the Airy disk size of the individual telescopes, that is to say about 0.01 arcsecond. This is accomplished by the pointing analyzer which is used to control steering mirrors (one for each of the 6 beams) with low frequency drift errors being fed back to the individual telescope attitude control systems.

The reference star beam cophasing errors are analyzed by a fringe tracker and are fed back to the common delay line.

8.3.2 Delay lines

The delay lines are located in the hub, where the beams are small and manageable. There is one common delay line and one reference star delay line for each of the 6 incoming beams.



Free-flying interferometer shown in close formation for clarity. Under normal conditions the distance between the recombining hub and the individual telescopes varies from 50 to 2500 meters.

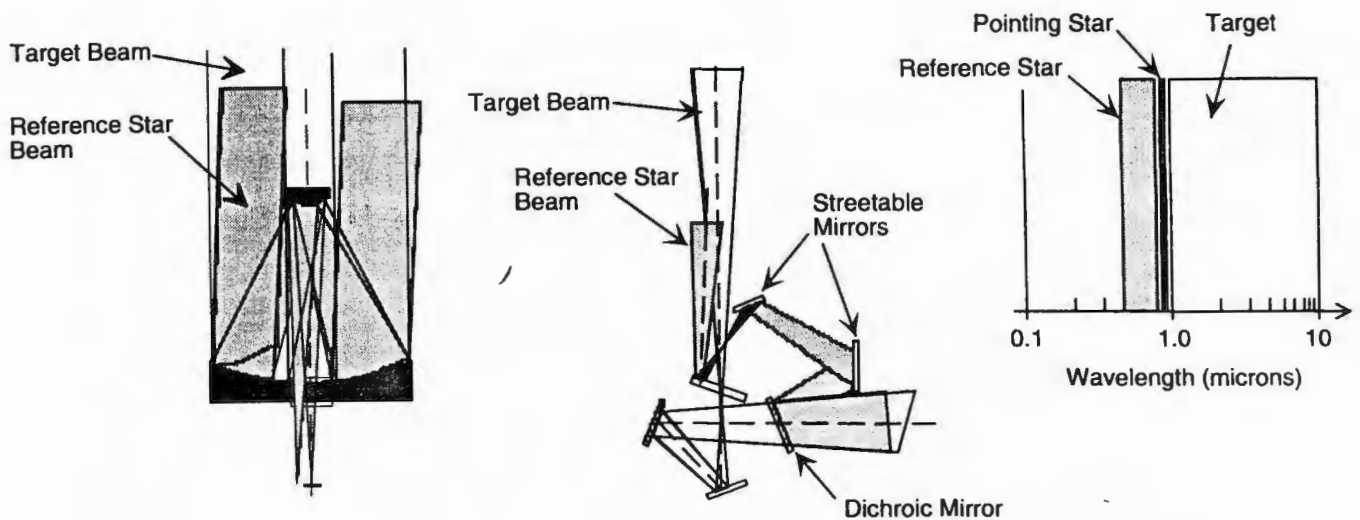


Fig. 8.4 The pointing star, reference star and target beams are spectrally multiplexed in the same transfer beam. This eliminates the need for additional transfer optics and guarantees that both target and reference star have the same optical pathlength. The bandpass of the target and reference star can be interchanged. When the scientific program requires the visible part of the spectrum, the reference star is sampled in the near infrared

The delay line common to the target and reference star beams compensates for small, temporary errors in the positioning of the telescope spacecraft. It is mainly used during the fringe acquisition phase to avoid physical translation of the telescope spacecraft. Its stroke is about 50 mm.

The reference star delay line compensates for optical pathlength difference between the target and reference star. For a reference star at the maximum field angle of 2.5 arcminutes and the maximum baseline (5000 meters), the delay line must be 3.5 meters in optical length. To reduce the mechanical stroke and overall size of the system, a possible solution is to use a folded system as sketched in Figure 8.5. The resulting system is very compact and requires a stroke of only 300 mm which can be obtained with a mechanical drive. A voice coil system provides the fine adjustment.

The delay line is first set using pre-knowledge of the absolute position of the reference star and target. This set-up is then refined after acquisition of the reference star and target fringes as a function of their actually measured angular separation.

8.3.3 Straylight control

Due to continuous presence of the sun in the selected orbit, it is indispensable that the telescopes and recombining hub be well protected. This is accomplished by keeping in shadow the portions of the spacecraft in the view of all other spacecraft in shadow, and by extensive baffling of the output and input transfer telescopes (Figure 8.6).

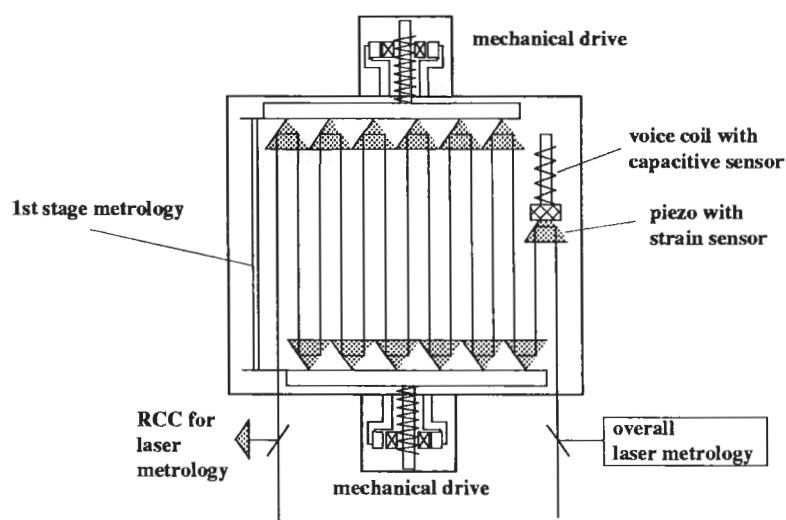


Fig. 8.5 Reference star delay line system providing the 3.5 meter stroke required for reference stars at 2.5 arcminutes from the target and maximum baseline length. The ranges of the mechanical, voice coil and piezo drives are 300 mm, 1 mm, and 0.01 mm. The positioning accuracy are 0.05mm, 1 micron and 1nm respectively. The overall size is 400 mm x 250 mm x 150 mm, the mass is 5 kg and the power requirement about 10 Watts.

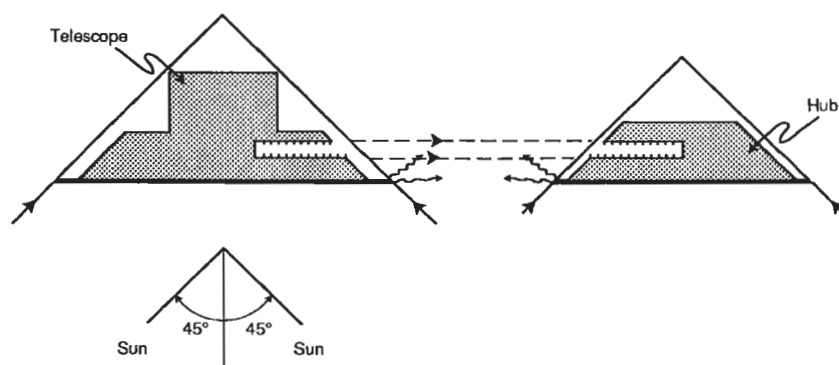


Fig. 8.6 Straylight protection. Straylight control. The main body of each spacecraft is always in shadow and the input transfer telescopes are well baffled. The amount of straylight due to scatter from the edges of the sunshield is lower than the zodiacal level.

The only straylight which can then reach the focal plane is that due to scatter and diffraction from the edge of the illuminated sunshield. At closest approach, say a distance of 50 meters between the hub and individual telescopes, this effect is estimated to be several magnitudes lower than the zodiacal light level and thus negligible. Straylight from the earth and moon will also be generally negligible because of the typically large off-axis angles and can be avoided completely if necessary by scheduling observation pointings accordingly.

8.4. Science operations

8.4.1 Nominal observation scenario

The interferometer is operated in a completely pre-programmed and autonomous mode. Coordinates of the target, reference star and pointing stars are uplinked and stored. At the scheduled start of an observation sequence,

the cluster is slewed to the target under control of the star trackers and laser metrology system. This is done with the cluster in a contracted configuration (baseline of about 50 meters). A minimum baseline is advantageous during slewing in order to minimize both the amount of fuel required and the internal optical pathlength uncertainty for reference star acquisition.

The pointing star is then acquired in each of the telescopes. The steerable mirrors and differential delay line for the reference star are then set to their expected position and the search for the reference star is initiated. Upon reference star acquisition, the incoming beams are co-aligned using the steerable mirrors, and the common delay line is moved step by step until fringes are acquired on the reference star. Assuming a 2 mm uncertainty on the optical path lengths (due to laser metrology measurement, imperfect knowledge of the reference star / target separation, overall pointing error of the cluster etc...), a coherence length of 1 micron ($\lambda^2/\Delta\lambda$ for a bandpass of 350 nanometers centered at 600 nm), and integration time of 1 second, this fringe acquisition can take up to 2000 seconds.

Target fringes can then be searched for by moving the differential delay line step by step. Fringes are first searched for with a narrow bandpass at the longest wavelength, and the detection is progressively refined by increasing the bandpass towards shorter wavelengths. Once fringes are found, the differential delay line is locked and the fine optical pathlength control is performed only with the common delay line. For a typical target of magnitude 20, the target acquisition phase is expected to last half an hour.

The science data take is then started and the array is expanded to cover the uv -plane (Figure 8.7). During expansion, the rate of which depends on target brightness and the number of pixels desired in the map, the differential delay line is displaced in an open loop fashion to compensate for the increasing optical pathlength difference. Upon reaching the desired maximum baseline, motion is reversed and the array is contracted back to its minimal baseline which completes the observation sequence.

According to our strawman mission, there are about 640 targets to be observed per year. so that the average observation will last about 14 hours.

8.4.2 Sky coverage

Because of the 45 degree sun constraint, the portion of the sky that can be observed at any one time is about 14% (Figure 8.8). Over a one year period, however, the band between $\pm 45^\circ$ of ecliptic latitude is observable, which represents about 72% of the entire sky.

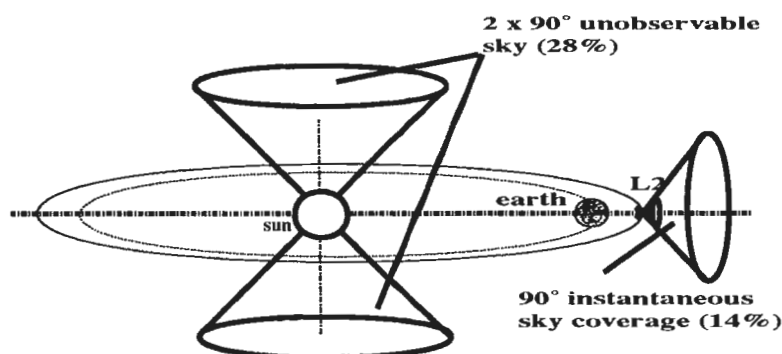


Fig. 8.8 Because of the sun's constraint, instantaneous sky coverage is limited to 14% but, over one year, 72% of the sky can be observed.

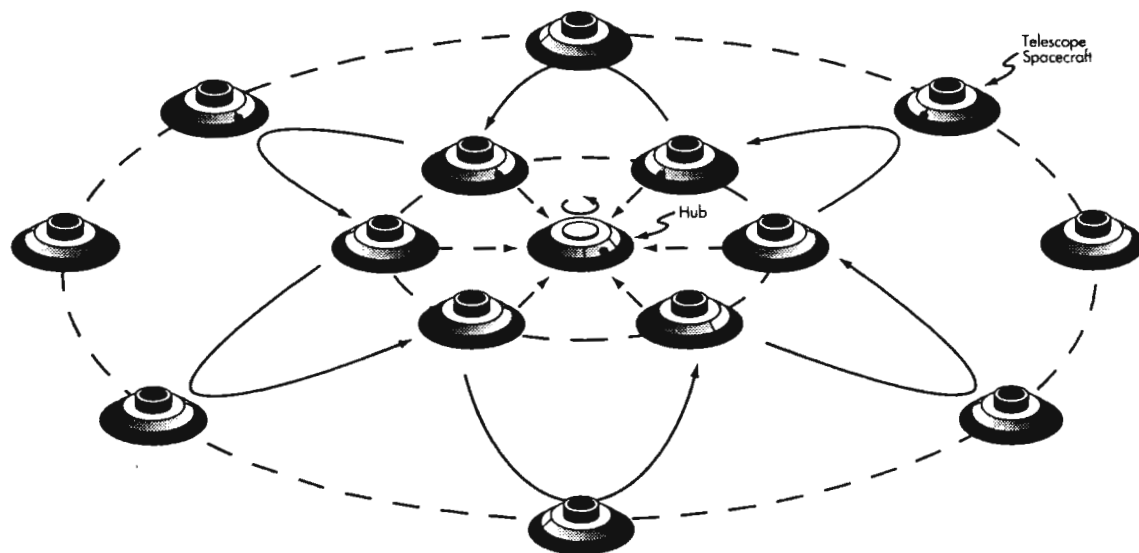


Fig. 8.7 Typical motion of the telescope spacecraft during an observation.

8.4.3 Mission observing program

The observing parameters for the typical targets of our strawman mission are shown in Table 8.1. The observing time and mission completion rate have been determined with the following assumptions:

- . optical throughput based on 15 reflections and 0.9 reflectivity
- . detector quantum efficiency of 0.95
- . main optics at 80 K and emissivity of 0.10
- . interferometric efficiency (ratio of actual fringe visibility to theoretical value) $\eta = 0.8$
- . during of the mission: 5 years
- . scheduling efficiency: 95% (5 % allocated for station keeping)
- . cluster pointing : 1 hour
- . reference star and target acquisition : 1 hour
- . acceleration period: 1 hour
- . deceleration period: 1 hour

Table 8.1 Mission completion

Target	Max baseline (m)	Number config.	Coherence time (hrs)	Observ. duration (hrs)	Number observ.	% mission
Star disc	850	1	11.1	15.1	100	3.6
Supermass binar	5672	0	1.4	4.0	100	1.0
Star surface - active	1443	8	1.9	19.1	100	4.6
Star surface - convec	5672	1	17.5	21.5	30	1.6
Star surface - solar	3609	31	0.6	22.7	50	2.7
Star surface - magnet	825	5	3.9	23.3	50	2.8
Dust Shells	240	4	3.2	16.8	200	8.1
YSO Jet	1602	4	3.8	19.3	200	9.3
YSO disc	3060	4	7.5	34.1	100	8.2
Globular Cluster	60	1	11.6	15.6	100	3.7
Galactic center	655	3	4.7	18.1	40	1.7
Cepheids	5775	5	2.5	16.4	250	9.8
Contact binaries	4812	5	3.9	23.3	100	5.6
Cataclysmic binaries	3781	1	17.4	21.4	100	5.1
Gal Gravit. Lenses	1831	1	1.6	5.6	500	6.8
AGN BLR	2268	2	10.8	25.5	50	3.1
Extr. Gal. SN	2836	1	15.8	19.8	200	9.5
Subst Grav. Lenses	726	1	14.8	18.8	150	6.8
Grav Waves	567	2	6.8	17.6	100	4.2

8.5. General spacecraft design

The general spacecraft design takes full advantage of the Ariane 5's voluminous fairing. The large diameter (4.80 m) allows the spacecraft to be launched with a fixed sun shield. Such a shield shadows the entire spacecraft at all times, thus suppressing sun generated straylight and easing thermal control. This shield is big enough to support a large fixed solar panel working at all incidences up to 45 degrees from the sunline. Non-deployable, non-orientable appendages are preferable to minimize structural vibrations which are detrimental to optical pathlength stability.

The spacecraft structural backbone is a 1.66 m diameter cylinder housing the optical payload. This cylinder supports the sun shield and is also used to connect the spacecraft to adjacent spacecraft during launch and orbit transfer. In order to minimize overall height, the spacecraft support modules are mounted at the periphery of the main cylinder (Figure 8.9).

8.6. Attitude control and station keeping

This is the central problem of the interferometer free-flying version. In addition to the demanding attitude control traditionally required of single astronomical space telescopes, a free-flying interferometer necessitates accurate control of the telescopes flying in formation. This is made possible by the a combination of

- radio beacons and traditional star trackers for wide acceptance but coarse ranging and angular measurements during cluster initialization,
- use of a pointing star for absolute attitude sensing
- laser metrology for the *relative* determination of the spacecraft's positions (by ranging and triangulation)

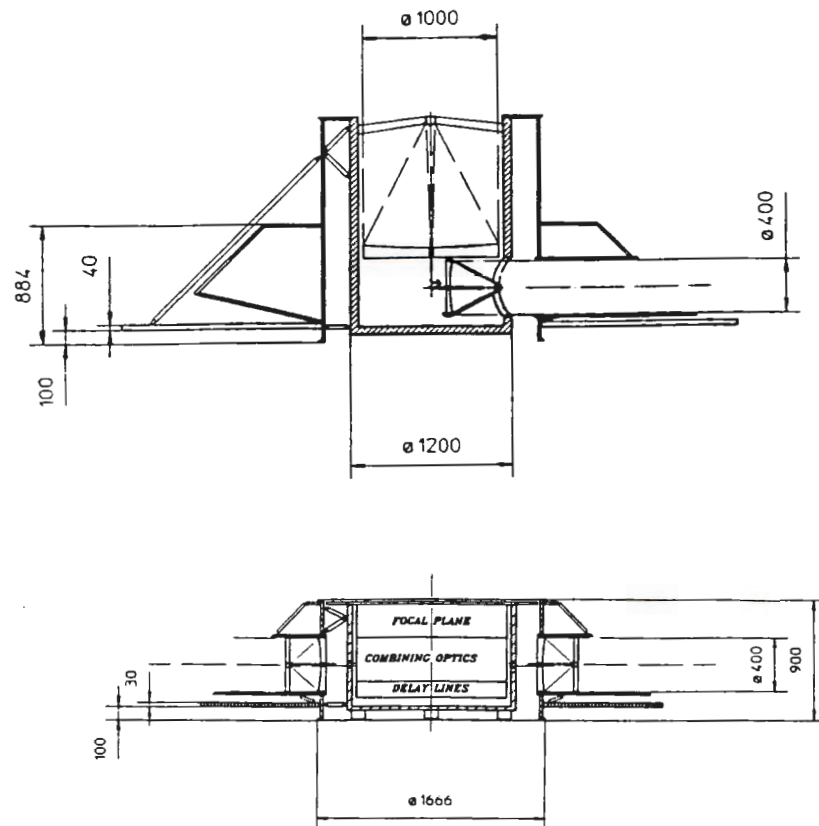


Fig. 8.9 Section of the telescope (top) and hub (bottom) spacecraft

- use of an unresolved reference star (low control frequency) augmented by ultra accurate accelerometers (high control frequency), for the *absolute* determination of optical pathlengths,
- ultra low level thrusters for precise attitude control and station keeping of the individual spacecraft,
- and active optics for beam recombination (steering optics) and optical pathlength error compensation (delay line).

The pointing star, reference star and active optics systems have been described above. The complementary systems are as follows:

8.6.1 Coarse attitude and position determination

The coarse attitude and position system is used during initialization and as a check during normal operation. Coarse attitude determination is accomplished by conventional means using star trackers. This brings knowledge of the spacecraft attitudes to within the range of the pointing star acquisition system (arcminute level). In addition, a radio beacon ranging system is used to determine and control the respective position of each of the spacecraft to within the acceptance angle of the laser metrology.

8.6.2 Laser metrology

The main purpose of the laser metrology is to determine the respective position of the telescopes and hub so as to ensure that they stay within the common reference-star/target cophasing range (section 6.1.1). For this function, the laser metrology must measure the position of the individual telescopes with respect to the hub to within $18\text{ }\mu\text{m}$ radially and to 20 mm in the transversal direction. The laser metrology is also used during cluster initialization and reference star acquisition to place the array within the coherence length of the reference star path which is about $1\text{ }\mu\text{m}$ radially (corresponding to bandpass of $0.35\text{ }\mu\text{m}$ at $0.6\text{ }\mu\text{m}$).

The distance between the hub and each of the telescopes is measured with a multiple wavelength laser system capable of an accuracy of 1 nanometer ($18\text{ }\mu\text{m}$ required) over the maximum baseline length (2500 meters). The transverse position of each telescope spacecraft is measured by triangulation using retroreflectors mounted on the central hub (Figure 8.10). These retroreflectors are at the extremities of 2.5 meter-long deployable booms in order to provide a transverse measurement of the position of the telescope spacecraft with an accuracy on the order of $1\text{ }\mu\text{m}$ (20 mm required).

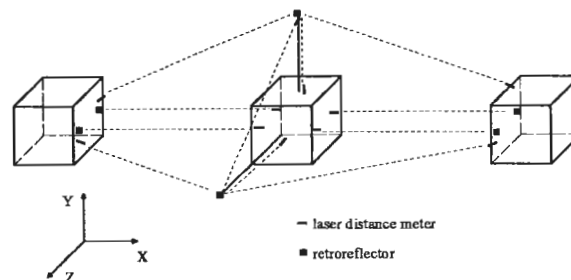


Fig. 8.10 The position of the telescope spacecraft relative to the recombining hub is measured using multi-wavelength laser metrology for ranging and laser triangulation for transverse directions.

8.6.3 Accelerometers

As explained in chapter 6, determination of absolute optical pathlength errors in the cluster relies on fringe tracking on a reference star in the field. Unfortunately, since this star must be unresolved at the maximum baseline envisaged, such stars are very distant and thus necessarily faint. With 1 meter apertures, the integration time required to track the interferometric fringes is on the order of 10 seconds . During that time, the telescope spacecraft must not move by more than the optical pathlength tolerable error, i.e. about 10 nanometers .

This is accomplished by use of accelerometers which sense the inertial position of each spacecraft. We based our analysis on the ultra-sensitive accelerometers developed by ONERA for drag free control of the Aristoteles mission. The measurement error (random walk) of these accelerometers as a function of time is shown in Figure 8.11. In the same figure is shown the measurement error of the reference star fringe tracker as a function of sampling time (as per Chapter 5). The reference star tracking error is calculated for an 18.5 magnitude star at 600 nm wavelength with a 350 nm bandpass, a telescope aperture of 1 meter , 50% optics throughput, and 80% detector efficiency.

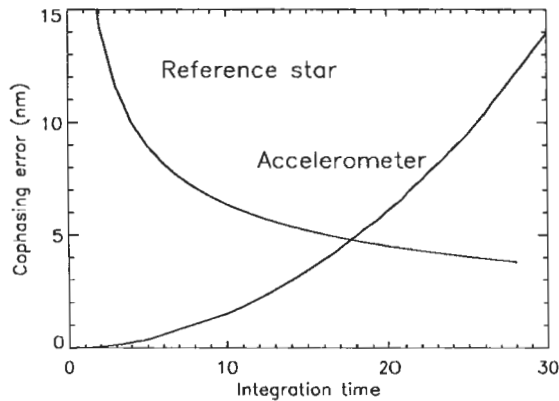


Fig. 8.11 Measurement error of the ONERA (Gradio) accelerometer as a function of time based on laboratory psd data. Also shown is the fringe tracking error as a function of time for an 18.5 magnitude reference star. The cross-over time is around 20 seconds. Blending the high rate accelerometer signal with a 20-second running update from the reference star tracking will control the optical pathlength to about 6nm.

If the resulting error is to be less than 10 nanometer rms, this graph shows that the combination of high rate accelerometer data with absolute update from the reference star can provide the required positional data with an ample margin of safety.

An implicit condition for the use of these accelerometers is that the gravity field be uniform enough. This is because these accelerometers, the principle of which is to measure the motion of a proof mass, can only detect acceleration relative to the pre-existing gravity field. This condition is, however, easily met at the halo orbit around the second Lagrange point where the gravity gradient is of order 0.02s^{-2} .

8.6.4 Control actuators

The actuators used to control the attitude and position of each spacecraft must exhibit the following characteristics:

- smooth and accurate force and torque capability on the three axes of each spacecraft, with a quantization step on the order of $1\mu\text{N}$,
- continuous operation during the entire mission, over a wide range if necessary,
- high specific impulse (ratio of the thrust supplied over a given time to the weight (earth weight) of the propellant used) to reduce the overall mass of the spacecraft,

On the other hand, the requirements on control authority and bandwidth are not demanding:

- the control authority does not need to be high, only on the order of 10 milli-Newtons thanks to the low disturbance orbit selected
- bandwidth of operation in 0.1 Hz range resulting in an actuation rate of a few Hz,

These requirements, together with the very high accuracy pointing and positioning objectives of the mission, indicate that the free-flying interferometer mission can benefit from the technology developments and design approach of currently studied drag-free missions. Indeed, the need for simultaneous attitude/translation control makes the use of the micro-thrusters foreseen on drag-free platforms quite attractive. This has the major advantage of a unified actuation system and also avoids the stringent micro-vibration problems associated with the use of reaction wheels on high-accuracy platforms. Both control force and torque are then generated by the firing of thrusters, which implementation (position and thrust orientation) can be optimized according to

the spatial distribution of the disturbance force and torque and of the required control authority for maneuvers.

We have therefore investigated two candidate propulsion systems currently under study for an application on drag-free platforms, namely proportional cold gas thrusters and FEEP (Field Emission Electric Propulsion). Indeed, other conventional thrusters are not accurate enough because of their high thrust rating and their on/off mode of operation, and are definitely not compatible with high accuracy pointing and station keeping. Other electric propulsion systems such as ion propulsion and thermal arcjets cannot be controlled accurately enough to serve as propulsion system during the operational mode.

A detailed analysis of the two retained actuation systems appears in Appendix A. We conclude that the proportional cold gas thrusters are not adequate in our application because of their low fuel efficiency. On the other hand, except for their large power requirement, FEEPs constitute an ideal solution, being very compact and providing extremely smooth actuation over a wide range of thrust, from a few μN to a few mN. Their specific impulse is very high (6000 s) and their maximum thrust is limited only by their large power consumption (600 Watts peak).

8.6.5 Optical path control computer simulation

The control of the optical path to nanometer level using a faint reference star is vital to the success of the proposed free-flyer concept. In order to verify that performance in the presence of environmental disturbances and with actual sensor and actuator characteristics would approach the predictions made with first order analysis, we have performed a computer simulation of the entire optical path control system including sensor, actuators and body dynamics.

The simulation was developed with the Matrix-X/System Build package and covers the control of the optical path from a single telescope unit with respect to the recombining hub. The optical path control system was designed as two nested loops, one for the control of the telescope position and the other for the vernier delay line inside the hub. The disturbances included solar pressure, gravity gradient and spacecraft body dynamics. Sensor (accelerometer and reference star) and thruster noise were also included. The moving mass of the vernier delay line was taken as 5 grams.

A typical result of the simulation after optimization of the control parameters is shown in Figure 8.12 and confirms that the position of the telescope with respect to the hub and the optical path can be controlled to better than the required values (position error < 18 microns in the radial direction, $< 20\text{mm}$ in the transverse direction, and optical path < 15 nanometers – ref section 6.1.1).

8.6.6 Fuel consumption

Because of sun constraint, available targets are limited to a band on the sky 90 degrees wide (± 45 degrees in ecliptic latitude). Since there are about 640 targets to be observed per year, the average distance between targets is $\sqrt{360 \times 90/640}$ or about 7 degrees. Observations can be chained in an optimum fashion (typically pointing in the antisun direction and scanning the band up and down), so that the average slew distance will be of the same order (Figure 8.13).

The slew being accomplished at minimum baseline, say with a 50 meter telescope/hub radius, maximum spacecraft translation will be about 6 meters.

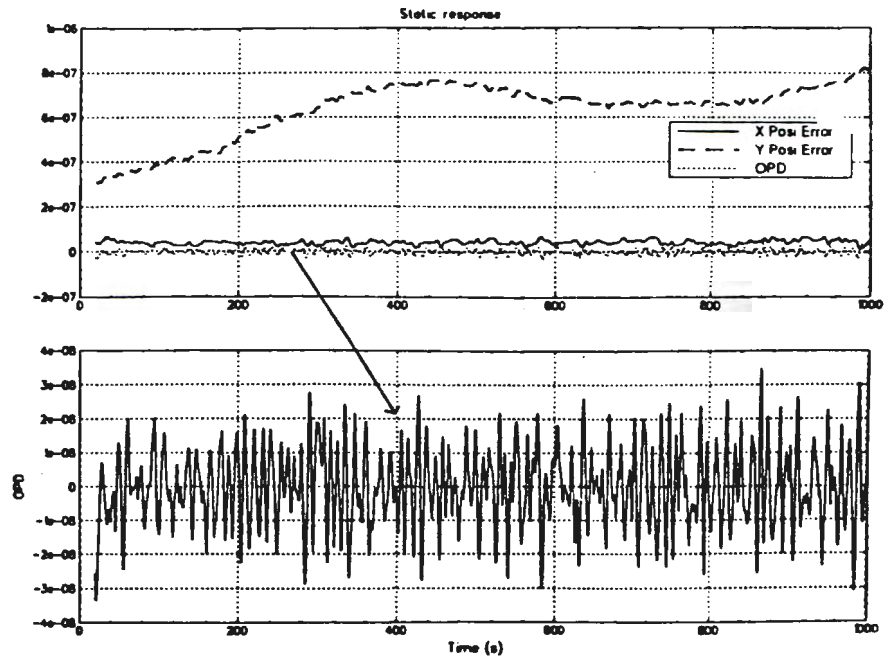


Fig. 8.12 Time simulation of the optical pathlength control. The radial (X - solid line) and transverse (Y - dashed line) position error of the telescope unit with respect to the hub, and the optical path error (dotted line) are shown on the upper plot. The optical path error is shown with a magnified scale in the lower plot.

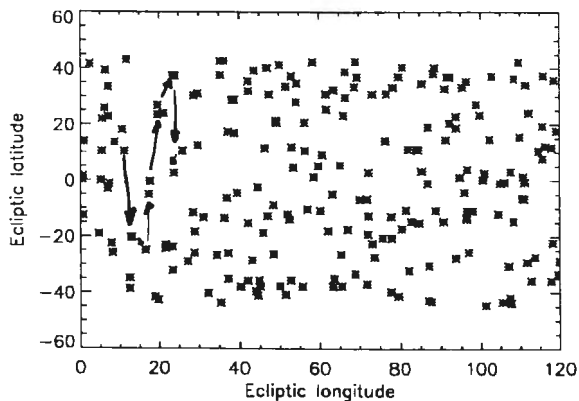


Fig. 8.13 A simulated field of targets observed over one year. Observations are chained with a traveling salesman algorithm in order to minimize target to target slew distance. Typically, the 90 degree wide sky band will be scanned up and down in latitude and drifting at the earth rate in ecliptic longitude. The average slew is about 7 degrees and is accomplished in 20 minutes at minimum cluster baseline.

Assuming a maximum thrust of 10 mN and a bang-bang slewing profile (maximum thrust applied continuously during the first half of the slewing period, followed by a reverse thrust during the second half), this will be accomplished in about 20 minutes.

With the FEPP thrusters sized for a maximum thrust, F , of 10 milliNewtons, and a spacecraft mass, m , of 600 kilograms, the maximum acceleration possible is $F/m = 1.7 \cdot 10^{-5} \text{ m/s}^2$. After the one hour allocated for acceler-

ation, the telescope spacecraft have moved radially by about 100 meters and their radial velocity is about 6 cm/s. The telescope spacecraft are then decelerated radially while following a curved trajectory to improve the *uv*-plane coverage. This requires about 2 milliNewtons including an allowance for optical pathlength control, spacecraft rotation and flight dynamics (solar pressure and gravity gradient compensation). Upon reaching maximum expansion at essentially zero velocity, the motion is reversed and terminates with a fast deceleration phase lasting about one hour.

The orbit maintenance requirement can be estimated at 15 m/s/year from the predictions made for SOHO which is in a similar halo orbit, albeit around the L1 point. At 600 kg per spacecraft this would require an average of 0.03 mN if applied continuously.

Fuel consumption is given by

$$m_{fuel} = \frac{F \delta t}{g I_s}$$

where I_s is the specific impulse of the propulsion system, F the thrust to be supplied and δt the duration of the maneuver. For a specific impulse of 6000 seconds, the fuel consumption for a maximum baseline 24 hour observation is shown in Table 8.2. The estimated total fuel requirement for the strawman 5 year mission is 8 kg per telescope.

Table 8.2 Estimated fuel consumption for a 24 hour observation

Phase	Duration (hours)	Average thrust (milliNewton)	Fuel consumption (grams)
Slewing to target	1	0.1	-
Reference star acquisition	1	0.1	-
Expansion - Acceleration	1	10	0.6
Expansion - Deceleration	10	2	1.2
Contraction - Acceleration	10	2	1.2
Contraction - Deceleration	1	10	0.6
Orbit maintenance	1		0.3
Total per observation			3.9 g

8.7. Thermal design

Operation of the interferometer in the near infrared (up to 12 μm) requires that the optics be cooled to 70 °K or less in order to minimize background emission. A second condition is the minimization of thermal changes on a time scale of individual observations (days) so as to avoid temperature-driven instability in the optical system. Operation of the spacecraft at the sun-earth L2 point, with no eclipse, and slow varying orientation with respect to the sun, provides a very favorable thermal environment from these two points of view. The spacecraft thermal system has been designed accordingly.

All heat-dissipating electronics are located outside the primary structure and are mounted on the sunshield. The optical payloads have triple stage passive cooling. The payload is isolated inside a thermal closure and has its own radiator. This enclosure is itself nested inside a thermal shroud with its own radiator and is interfaced with minimal conduction and radiation losses to the primary spacecraft cylindrical structure. Finally, the primary spacecraft

structure is itself thermally decoupled from the sunshield and heat dissipating equipment. A schematic view of the thermal design of the hub is shown in Figure 8.14.

Cryogenic cooling of the detectors could make use of active cryo-coolers, but they would be turned off during observations so as to avoid transmission of vibrations to the optical system.

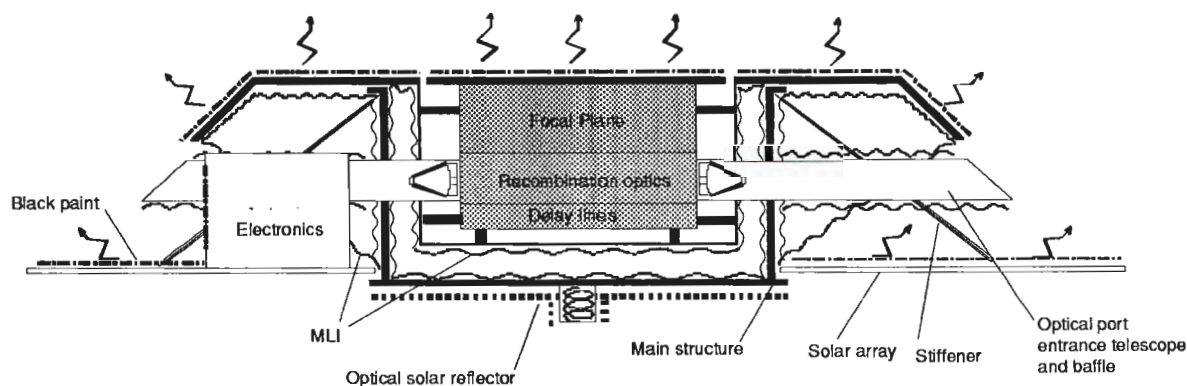


Fig. 8.14 Schematic view of the hub spacecraft thermal design

8.8. Data handling and communications

Most of the communication needs are concentrated in the recombining hub. It is therefore most efficient to centralize all communications at the hub spacecraft. Communications between the individual telescope spacecraft and the hub are estimated at 20 kb/s (health and safety and attitude commands) and are well within the capability of a simple omnidirectional UHF system.

For communications between the hub spacecraft and earth, we have assumed the use of a single earth station, e.g. the Wilhelm station in Germany equipped with a 30 meter antenna, with a maximum visibility of 8 hours per day.

The earth-hub data transmission rate is driven by the need to downlink the interferometric frames. Assuming no on-board processing, a detector array of $150 \times 20\,000$ pixels (150 for the spatial axis and 20 000 for the dispersion axis), a dynamic range of 8 bits, a minimal integration time of 1000 seconds, a time on target efficiency of 80%, and a downlink period of 6 hours per day, the data rate is 26 kb/s. Adding a few kb/s for housekeeping telemetry, the system should be capable of about 30 kb/s. Although not demanding, this data rate prohibits the use of an omnidirectional antenna, and a medium gain antenna (60 degrees FWHM) is necessary. Since, in the selected halo orbit, the earth to target angle can vary by as much as 67 degrees, 5 fixed antennae are required to cover all cluster pointing orientations (Figure 8.15).

The uplink communication is much less demanding, and is estimated at a few kb/s during the remaining 2 hours of visibility per day. This is well within the capability of the provided antennae.

On-board data storage requirement is about 300 Mbytes which can be handled by solid state recorders.

During the transfer flight, all individual spacecraft antennae are hidden in the substacked configuration and are unusable. Communications rely on an omnidirectional antenna mounted on the transfer stage.

During safe mode events, all spacecraft will be forced to face the anti-sun direction to get maximum power; the nominal antenna is thus well suited for telecommunications.

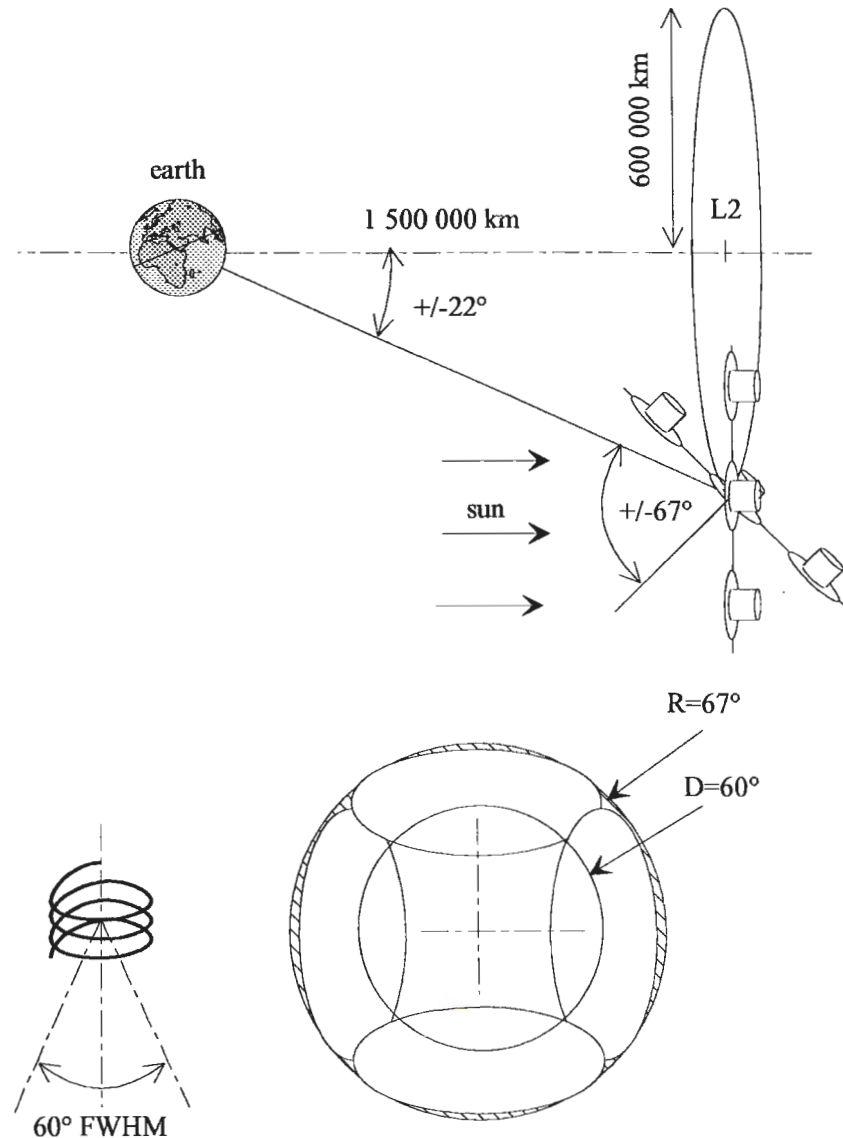


Fig. 8.15 Principle of the telecommunication system. The hub to earth communication antenna consists of a set of 5 medium gain antennae. The antenna to be used is selected by an RF switch, depending on the orientation of the cluster with respect to the Earth.

8.9. Power system

The power requirement for each spacecraft (telescope or recombiner) is estimated at 600 Watts for hub and 1100 Watts for each telescope unit (Table 8.3). This power is easily supplied by fixed solar panels mounted on the large sunshield. The panels are arranged in a ring of 4.7 meter outer diameter

and 1.8 meter inner diameter (the diameter of the launcher/spacecraft interface). This results in an active area of about 17 m^2 . Allowing for a 45 degree worst case inclination between the solar panels and the sunline and taking into account a poor filling factor because of the circular shape (typically 0.75), and a reduction of 0.864 for end of life condition and high operating temperature, the total available power end of life will be 800 W with Si cells and 1160 W with AsGa cells giving a comfortable safety margin.

The bus is fully regulated to cope with the large voltage excursion due to the large variation in sun angle (0 to 45 degrees). Since the selected orbit has no eclipse, no battery power is required for normal operation. However, a 40Ah battery is provided in each spacecraft for survival power during transfer orbit maneuvers and for increasing the safety margin for peak loading periods during operations.

During orbital transfer all the spacecraft power system (solar panels and batteries) resources may be combined to compensate for intra-spacecraft shadowing.

8.10. Mass and power

The mass and power of each spacecraft is estimated as shown in Table 8.3. The aggregate mass of the interferometer is about 4260 kg when is station, i.e. excluding the transfer stage and associated propellant.

Table 8.3 Estimated mass and power

Subsystem	Mass (kg)		Power(W)	
	Telescope	hub	Telescope	hub
Telescope	120	-	60	-
Recombiner	-	100	-	100
Structure	100	110	-	-
Thermal	80	90	80	80
Data handling & communications	40	90	40	60
Power	130	140	10	10
ACS and laser ranging	40	40	80	90
Propulsion	30	40	600	200
Contingency	60	50	180	100
TOTAL	600	660	1060	600

8.11. Launch and deployment

The six telescope units, hub and transfer stage can be accommodated in a single Ariane 5 launch (Figure 8.16). Total mass of the cluster and transfer stage is estimated at about 5 metric tons (4260 kg for the interferometer and 800 kg for the wet mass of the transfer stage). This is beyond the capability of the current Ariane 5, but well within the expected capability of Ariane 5-E (5200 kg on the liberation orbit for $V_{\infty} = 0$).

The launcher would place the stacked satellites onto a liberation orbit, leaving only corrections and injection maneuvers to be handled by the transfer stage. The required impulse for these maneuvers is estimated at about 175

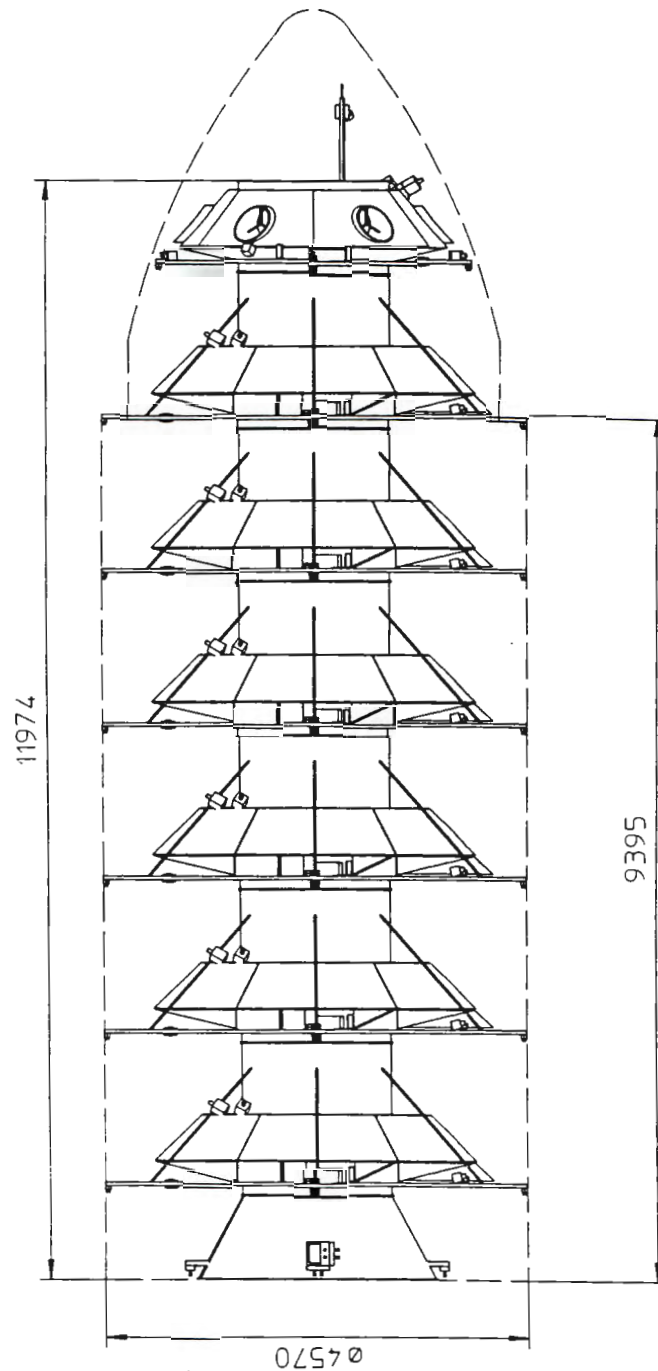


Fig. 8.16 Launch configuration. The 7 spacecraft (6 telescope units and hub) can fit into a single Ariane 5E launch.

m/s. Depending on the exact Ariane 5E capability, some additional impulse could be provided by the transfer stage.

After injection on the halo orbit, the transfer stage maneuvers to permit

separation of the individual spacecraft, one after the other. After separation is complete, the transfer stage is jettisoned and each spacecraft becomes autonomous and relies on its own attitude control and electric propulsion system. The first operation is the 3-axis stabilization of each satellite, which is executed using star trackers. The second operation is the clustering of the interferometer telescope units in a close formation around the central hub: since the successive separation of the 7 spacecraft may last several hours, they could end up several tens of kilometers away from each other. This is gradually accomplished with increasing accuracy as the spacecraft approach each other. Radio direction-finding systems located on each spacecraft are first used and allow the direction of each spacecraft to be determined to a few degrees. The metrology laser transmitters are then used in a defocussed mode to create a large diameter beacon by the position detectors in the metrology receivers. This improves the initial inter-spacecraft angles to the arcminute level which is enough for the normal mode laser metrology to take over.

With the cluster of telescope at short range (50 meters) to minimize optical uncertainty, the nominal acquisitions of the pointing star, of the reference star, and finally of a science target may be initiated as described above for normal observations.

References

- Cornwell, T.J., 1988, "A novel principle for optimization of the instantaneous Fourier plane coverage of correlation arrays", IEEE Tr., AP-8,1165.

COMPARISON OF THE TWO VERSIONS

The study of the two versions of the interferometer indicate that they are both feasible, do not exhibit major show stoppers and can essentially meet the scientific requirements we had established. Clearly, nonetheless, there are differences.

Perhaps the main point is that locating an interferometer on the moon does not bring any obvious simplification in construction or operation. One could argue, on the contrary, that the moon-based system has to cope with a much more severe environment than its space-based counterpart: large temperature swings (day/night), ground disturbances, the impossibility of observing during the lunar day, dust, and lack of solar-generated power during the lunar night.

From the observational point of view, too, the space-based system has the advantage. There is no real limit to its baseline length. Its efficiency is about twice as much because of the impossibility of the moon-based counterpart to observe during the lunar day. Its array can always be configured optimally, while the lunar-based has to contend with whatever source declination and geographic latitude provide. And for some scientific programs, the moon simply rotates too slowly: super synthesis mapping requires half a lunar day or about 14 earth days, which is too long compared to the rotation or time scale of physical processes of many sources.

On the logistical side, our analysis has also shown how difficult the automatic deployment of a major facility on the moon would be. Although not strictly necessary, astronaut supervision and site preparation would be highly desirable.

Finally, with regard to cost, although only rough orders of magnitude were estimated it is clear that the moon-based scheme would be more expensive. The moon-based system, which requires two launches and a sophisticated landing module, is estimated at 1.7 times the cost of the free flyer, although some savings would be possible if the lunar lander can be simplified thanks to astronaut assisted deployment.

Table 9.1 summarizes the comparison of the two versions.

Table 9.1 Free-flyer vs Moon-based comparison.

Characteristic	Free-flyer	Moon-based
Science related		
Maximum practical baseline	>5 km	5 km
uv coverage	Good	adequate
Minimum time required for uv coverage	1 day	14 days
Wavelength coverage	0.4 to 12 μm	0.4 to 12 μm
Optical throughput (in V)	0.75	0.50
Need for reference star	Yes	Yes
Optics temperature	60 K	60 K
Yearly sky coverage	72%	86%
Instantaneous sky coverage	14%	45%
Observing efficiency	80 %	45%
Engineering aspects		
Complexity of optical path control	-	long throw delay line
Thermal stability	excellent	adequate (night)
Radiation environment	-	slightly better
Micrometeoroids flux	-	slightly less
Maintenance & upgrading	unit level	module level
Lifetime	10 years	indefinite
Power generation	solar	solar + fuel cells
Communications	adequate	same
Payload mass	4200	4400
Wet launch mass	5000 kg	15200
Launch requirement	1 Ariane 5E launch	2 Ariane 5E+H10

TECHNOLOGY DEVELOPMENT PROGRAM

Since the moon solution should not be envisaged before plans for a manned base are more definite, no technology development is necessary at this time. The free-flying scheme, on the other hand, could well be considered on a shorter time scale, but will require more studies and technology development to ensure its readiness.

The main areas requiring a strong technological development and validation program are as follows:

- . FEEP actuators in the micro to milliNewton range,
- . dual wavelength (absolute) laser metrology over the 10 to 5000 meter range at the micron level
- . reliable low-noise accelerometer system
- . high performance delay line: long throw (2.5 m), ultra smooth (1 nanometer), compact, high throughput and reactionless

Precursor missions with the goal of validating the optical path length control and free-flyer spacecraft concepts also appear essential. As far as the interferometry validation goes, a possible low cost solution could be to fly a prototype interferometer piggy back on a scientific mission or on the space station. This precursor could consist of 2 small telescopes (10 cm diameter) attached to a non rigid structure with a differential delay line and a simplified laser metrology. This would serve as a demonstration of the optical path control in a noisy environment. A schematic view of such a precursor is shown in Figure 10.1.

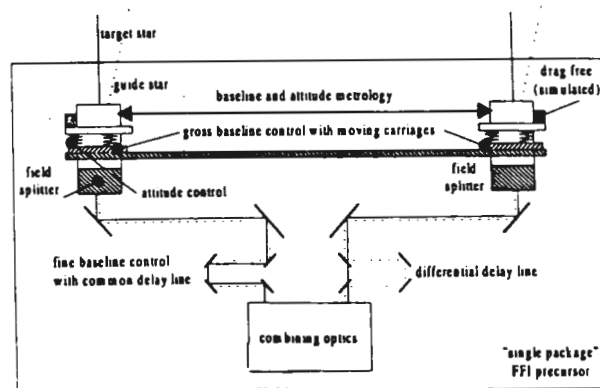


Fig. 10.1 Schematic view of a possible precursor mission for the validation of delay line and metrology control.

CONCLUSIONS

This study has shown that, due to tidal and meteoroid-induced seismic disturbances, the moon is not as stable a space platform as has been thought, and that both moon-based and free-flying interferometers would require essentially the same type of metrology control. Although both versions can reach the required scientific performance, the free-flyer offers intrinsic advantages such as shorter time required for image synthesis, reconfiguration flexibility and a quasi unlimited baseline length. Furthermore, the observational efficiency of the free-flyer is greater by approximately a factor of two, since the moon-based version cannot be operated during the lunar day.

On the logistic side, the study has also shown that automatic deployment of the moon-based version would be extremely difficult. Prior site preparation and man-assisted deployment appear to be essential. The lunar version would thus have to wait for a manned base. On the other hand, the availability of man at a lunar base means that maintenance and upgrading would be possible. The higher investment in a moon-based interferometer would thus result in a longer lifetime facility with continuous performance enhancement possible.

We conclude that the free-flyer is better suited for implementation in the near or mid-term future, but that the moon-based version could be considered in the long term in conjunction with a manned lunar base.

In view of the extraordinary scientific potential of long baseline space interferometry and the attractiveness and technical feasibility of the free-flying concept based on independent spacecraft, we recommend that this approach be included in the preparatory studies of the IR option of the *Interferometry Cornerstone mission* identified in the Horizon 2000+ program.

We also recommend that the free-flying scheme be considered as an implementation possibility for the shorter baseline near infrared of the type defined for the search for exo-planets (e.g. *Darwin*). Placed in a heliocentric 1×5 AU orbit to reduce the background due to zodiacal dust, such a smaller baseline free-flying interferometer could constitute a very efficient observatory to detect and analyze earth-like planets around nearby stars in addition to performing a suite of outstanding galactic and extragalactic observations in the near infrared.

Interferometric imaging missions, whether medium or long baseline, will require considerable development and validation, especially regarding high accuracy delay lines, fringe tracking system, multi-aperture synthesized imaging and focal plane instrumentation. Since the European Southern Observatory (ESO) is engaged in a similar interferometric imaging program on the ground, we finally recommend that the two organizations coordinate their activities in this domain in order to capitalize on their respective technological development efforts.

Appendix A

LOW THRUST LEVEL PROPULSION

The key technology which enables the free-flyer scheme is the availability of very low level thrusters to control the respective positions of the interferometer array elements to micrometer accuracy. Here we compare possible candidates for actuation systems and conclude that the FEEP thrusters are the most suitable.

The free-flyer scheme does not require a high level of thrust. A thrust level as low as 10 mN would be adequate. This low control authority is enough to cover all operational modes, i.e. observation position control as well as array reconfiguration, initial acquisitions and orbit maintenance. But the thrusting system must have very high resolution, of order 1 μ N.

We compare here two candidate propulsion systems: proportional cold gas thrusters (used with nitrogen) and FEEP (Field Emission Electric Propulsion). These technologies, foreseen for future drag-free missions such as LISA and STEP, are the only ones meeting the above accuracy requirement, with the additional advantage of providing a unified actuation system for attitude and translation control.

Comparison of the performances of the two candidate actuators demonstrates that proportional cold gas thrusters are not applicable because of their low fuel efficiency, resulting in an excessive nitrogen consumption to realize the reconfiguration maneuvers. Therefore, the proposed baseline design implements FEEP thrusters in clusters to achieve a 3-axis force authority of 10 mN, strongly limited by the large power consumption (600 W peak required to operate the FEEP thrusters). A two-stage propulsion system implementing high authority thrusters to complement the FEEP during the maneuvers has been evaluated but not retained as baseline because of significant system impact (mass, complexity and cost) and the associated increase of fuel consumption. FEEP thrusters are currently under development and testing at Centropazio (Italy) under ESA funding and should be space-qualified by the time of the mission. The critical technological areas are:

- the cesium feeding system for long-time operation requiring several kg of propellant,
- the power conditioning system to provide the required high voltage signals with a high conversion efficiency and a high accuracy,
- and the reliability of the emitter unit, very sensitive to pollution by water and other solvents. These points are currently investigated in the frame of on-going studies, which results should benefit to the present study.

A.1 FEEP thrusters

Operation principles

Field Emission Electric Propulsion (FEEP) is an electrostatic propulsion concept which originated at ESA/ESTEC in the 70's. Unlike other ion engines, FEEP thrusters do not require propellant vaporization in order to obtain ionization; ions are directly extracted from the liquid phase. FEEP thrusters can accelerate a large number of different liquid metals or alloys. Cesium proved to be the best choice, due to its high molecular weight and its low ionization

potential. As cesium liquefies at 28.4 degree C, the thruster's thermal power requirement is much lower than in conventional ion thrusters, and the emitter thermal control is quite simple. The efficiency of conversion of electric power to propulsive power reaches values as high as 98% as opposed to maximum values of about 80% met in other ion engines. Specific impulse is in the range of 6000 to 10000 s, and may be easily adjusted to meet specific mission requirements. Thrust level is finely tunable, and instantaneous switching capability allows pulsed mode operation. Clusters of emitters have been successfully tested.

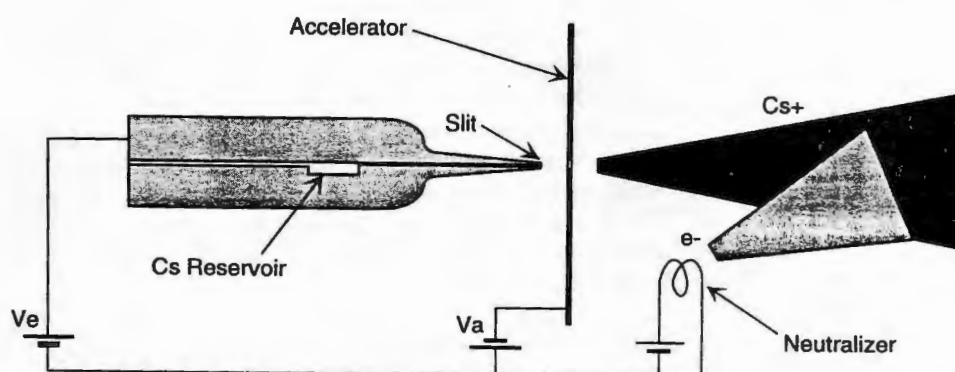


Fig. A.1 FEED thruster principle of operation.

Thrust is obtained by exhausting a beam, mainly composed of singly-ionized cesium atoms, produced by field emission. The emitter module consists of two plates in Inconel (a Nickel alloy with 14 to 17 % Chromium), with a small propellant reservoir (figure A.1). A sharp blade is accurately machined on one side of each plate. A thin layer of Nickel is sputter-deposited on the other three sides; when the two emitter halves are tightly clamped together, a $1\text{ }\mu\text{m}$ gap is left between the blades. Cesium flows through this tiny channel, forming a cylindrical free surface at the exit of the slit, with a radius of curvature of about $1\text{ }\mu\text{m}$. Under a strong electric field, generated by the application of a voltage difference of about 10 kV between the emitter and an accelerator electrode located in front of it, the free surface of the liquid metal approaches a situation of local instability, due to the combined effects of the electrostatic force and the surface tension, and creates a series of protruding cusps (Taylor cones); the local electric field at the tip increases as the radius of curvature of the cusps decreases. When the electric field reaches a value of about 10^9 V/m the atoms at the tip spontaneously ionize and an ion jet is extracted by the same electric field, while the electrons are rejected in the bulk of the liquid. Mass flow rate is extremely small and requires no control, as the particles extracted are replaced by the capillary actions from the propellant reservoir in the amount necessary to maintain dynamic equilibrium at the emitter tip. When voltage is removed, the capillary force prevents the propellant from pouring out of the

slit. Emission rise time ranges from 10 to 30 millisecond, depending upon the ion current; the minimum impulse bit is as small as 10^{-8} Newton-second.

Thruster performances

By varying the height of the slit and the width of the blades, FEED thrusters can be easily rated to a wide range of thrust, from a few N to a few mN. Moreover, owing to the very compact design of the emitter (figure A.2), several units can be assembled in a cluster to achieve higher thrust levels (up to a few 10 mN), as it is planned on the LISA platform. The implementation of FEED with different rating in clusters is certainly attractive for the free-flyer. Indeed, the high accuracy thrust capability required during the measurements can be realized with micro-thrusters rated to a few μN while the higher control authority necessary for reorientation maneuvers is achieved with several mini-thrusters scaled at a few mN, these thrusters being off during the operational mode. There is no theoretical limitation to FEED thrusters resolution, even if it certainly depends on the rating of the thrust. Practical resolution as low as $0.001 \mu\text{N}$ are expected, which makes FEED thruster the most accurate thruster ever developed. Obviously, direct measurement of such very low force levels is not possible, so that experimental validation of the FEED performance is a key issue.

The specific power is in the range of 60 W/mN, which is quite high as compared to conventional ion thrusters. This is the major restriction for the use of FEED thrusters, since the power available on-board the S/C rapidly limits the thrust authority. On the free-flyer satellites, a preliminary power budget indicates that the maximum power available for the propulsion system is about 600 W, resulting in a control authority of about 10 mN. Owing to the very high specific impulse of the FEED thruster, the propellant consumption is not a major constraint. Actually, with the 15 mN thrust required for reorientation maneuvers, the mass flow rate is only 0.25 mg/s, which results for the maneuver schedule considered in the previous section, in an average cesium consumption of about 3 grams per day.

Feeding System

The amount of propellant required for the fine control with μN thrusters in operational mode is typically of a few grams over the mission. Therefore, it is possible to manufacture for micro-thrusters a self-contained, integral emitter-reservoir unit, thus limiting the feeding system control to the thermal conditioning and reducing the interface with the spacecraft to the electrical connections only. For the mN range thrusters to be used for maneuvers, the larger amount of cesium requires a specific storage and feeding system. The initial concept, developed for application to telecommunication satellites, consisted of a tank containing Cs_2CrO_4 powder, an inert compound which is both easy to handle and store. When heated up to 660 degrees Celsius, the powder decomposes and pure cesium is released. This system, recently tested at Centropazio, is sturdy and reliable and has the advantage to store the propellant in a solid state, preventing the disturbances associated with liquid sloshing in the tanks. Nevertheless, this concept is not adequate for an application to the free-flyer interferometer, as it requires heating power (about 12 W) and introduces a high temperature spot which might be incompatible with the low temperature operation of the observatory. A new system, based on the use of capillary forces for cesium feeding, is being studied at Centropazio and should be compatible with an implementation on a high-accuracy platform. The development of a

space-qualified power supply for the FEEP thruster is not to be neglected. Indeed, the Power Conditioning and Control Unit (PCCU) shall transform the low voltage continuous power supply of the spacecraft into variable high voltage signals used to drive the FEEP thruster. The conversion efficiency must be high to minimize the already high power demand and the mass of each PCCU must be low enough to allow the implementation of the 6 thrusters (at least) required for 6-DOF control of the spacecraft. The manufacturing and testing of a breadboard and of a flight-identical engineering unit is currently being performed by Centrospazio and Bradford Engineering (NL).

Reliability and validation status

The most likely cause of malfunctioning in the operation of FEEP thrusters is the emitter contamination during the early wetting of the emitter inner surfaces by the liquid propellant. The emitter performance is very sensitive to the presence of water vapor or other impurities on the channel and slit surfaces, as cesium reacts with water forming a solid hydroxide, that can obstruct the propellant duct and severely reduce the effective emitting length. This problem can be overcome by adopting a correct pre-flight procedure, i.e. performing a careful outgassing of the emitter in ultra-high vacuum before the introduction of the propellant. If started correctly, the ion emission characteristics become stable and can be reproduced precisely. No other failure mode has been reported. Although design improvements are still possible, the emitter technology can be considered as fully assessed. An "extended endurance" (or a "reduced lifetime") test, lasting about one year, is planned to be carried out in the near future at ESTEC in order to evaluate the emitter performance deterioration in time (if any). Moreover, detailed characterization of the emitter performance will be conducted in the frame of the FEEP development at Centrospazio (Italy) and of the R&D activities related to the LISA mission. Therefore, even if FEEP are currently not fully characterized, the technology will certainly be space-qualified by the time of the free-flyer mission.

A.2 Proportional cold gas thrusters

Development history

Historically the benefit of using Proportional Thrusters was identified on the Gravity Probe B (GP-B) program. Indeed, with the GP-B cryogenic payload (300 kg of liquid helium used to cool down the ultra-sensitive superconductive gyroscopes of the experiment), if not used for control, the gas jet disturbance caused by Helium boil-off would be the major disturbance on the spacecraft. Investigations in cold gas system performance showed that conventional on-off valves would not be a good solution for GP-B; with a design goal of ± 5 arcsec pointing accuracy, the number of firings over one year would have been 10^7 which would have caused reliability problems. Such restrictions also apply to the free-flyer mission, with even greater emphasis due to the higher pointing accuracy. On this basis, the design of Proportional Thrusters was started in the sixties at Stanford University, and after the investigation of various techniques to modulate the flow through a thruster, a design based on electromagnetic actuation of a poppet was proposed and adapted by both Lockheed and MOOG in the US to provide the needed performance for the GP-B mission. For STEP, the same considerations as for GP-B have led to baseline the use of Proportional Thrusters for drag-free and attitude control. The optimization of the thruster design and thruster system configuration is

even more important on STEP because of the limited supply of Helium (about 10 times less than on GP-B) and also because of the much lower altitude of STEP which induces larger aerodynamic disturbances to counteract.

Principles of a proportional thruster

The principle of operation of a proportional thruster is very simple: the gas flow is modulated through the displacement of a poppet in front of the nozzle aperture in order to produce a thrust proportional to the command delivered by the attitude/translation control algorithm. Each thruster is composed of a mechanical assembly housing:

a gas inlet

an actuation system to move the poppet in order to modulate the thrust by restricting the flow in the nozzle. If necessary for accurate positioning of the poppet, a position sensor could be added.

a nozzle to expand the flow into space

a pressure sensor to compensate for pressure variation effects on the thrust
the electrical connections necessary to actuate the thruster and send back pressure and/or position information

If considered necessary for accurate thrust control, the thruster can also accommodate a temperature sensor. The thruster design is realized in order to provide the spacecraft with an extremely quiet acceleration environment (low noise actuator) and to have a very linear or at least highly repeatable response. In particular, the dynamic disturbance induced on the satellite by the moving mass (reaction force due to poppet motion) must be minimized.

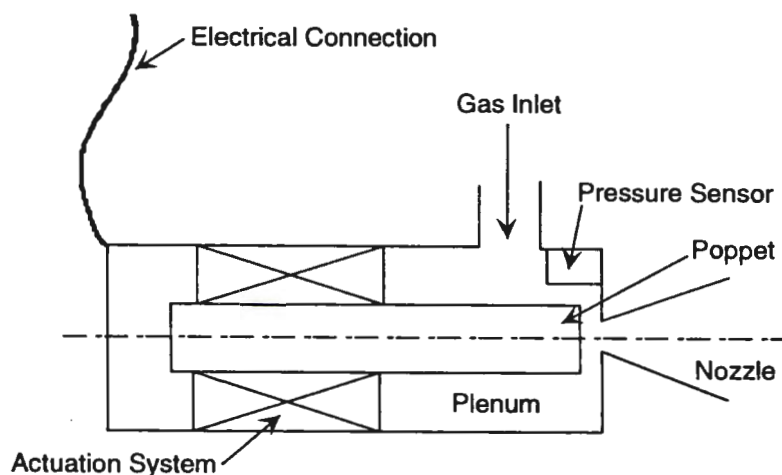


Fig. A.2 - Schematics of a Proportional Thruster.

Use of other gases as propellant

The concept of proportional thrusters is also applicable for the smooth and continuous control of high accuracy platforms which does not incorporate

a cryogenic payload. Nevertheless; the use of Helium as propellant is then not very attractive, because of the storage difficulties of this gas (very low liquefaction temperature). The most appropriate propellant is then nitrogen, much easier to store onboard a satellite, at the price of a significantly reduced efficiency: the achievable specific impulse is about 70 seconds, to be compared to 150 seconds for helium. There is a priori no major technical issue to adapt the helium thrusters developed in the frame of drag-free missions like GP-B or STEP for the use of nitrogen. Because of the reduced specific impulse, higher flow rates are likely to be required with nitrogen, resulting in thrusters with larger throat to accept larger input pressures.

The only currently existing proportional helium thrusters are those developed for GP-B (MOOG design), which main characteristics are listed in Table A.1.

Table A.1. GP-B cold gas thruster characteristics

Fluid	Helium
Pressure	< 20 Torr
Full poppet stroke	+/- 0.4 mm
Voltage	+/- 40 V
Linearity	< 1 %
Hysteresis	< 1 % (0.5 % tested)
Power	5.6 W at max stroke
Thrust	2.6 mN at 10 Torr
Mass	800 g

Moreover, the development of a specific European thruster for STEP is also planned, with design activities starting in the frame of the M3 phase A activities. The STEP thruster will be smaller than the GP-B one and is specified to accept other gases like nitrogen or argon as propellant.

A.3 Performance comparison

The objective of this section is to compare the characteristics and the performances of the two investigated propulsion for an application to the free-flyer mission. Table A.2 compares the characteristics of the two candidate propulsion systems. These figures demonstrate that both technologies can meet the requirements for the free-flyer interferometer. They also highlight the almost opposite characteristics of these thrusters in terms of power and fuel consumption.

Table A.2 Thruster performance comparison

	FEED	Prop. cold gas thruster
Thrust resolution (1 μN req.)	< 0.01 μN	1 to 10 μN
Response time	a few msec	20 msec
Thrust authority	1 μN to 15 mN (cluster)	1 to 20 mN
Efficiency (specific impulse)	6000 s	70 s (Nitrogen)
Power consumption	60 W/mN	5 to 10 W per thruster

The key parameters for the selection of the actuator technology impacts are then the mass and power consumptions. Preliminary mass and power

budgets are evaluated in table A.3. A 10 mN thrust level is considered for the realization of the maneuvers. The orbit maintenance can be evaluated from the detailed calculations made for the SOHO mission which is in a similar orbit. It is estimated at 10 m/sec/year. The cumulated maneuver duration with 10 mN available thrust is about 2200 hours over the mission, resulting in a daily orbit maintenance duration of 90 min. These results clearly demonstrate that the proportional cold gas thrusters are not adequate for baseline monitoring because of their low fuel efficiency. FEEP thrusters are the only sensible choice.

Table A.3. Fuel and power consumption over the 4-year mission

	FEEP	Prop. cold gas thruster
Fuel	Caesium	Nitrogen
baseline variation (two-ways)	3.8 kg	320 kg
90 deg rotation of the 20 m baseline	0.4 kg	37 kg
45 deg rotation around the baseline	< 0.1 kg	8.5 kg
orbit maintenance (40 m/sec)	0.34 kg	29 kg
Total fuel mass over the mission	4.5 kg	395 kg
Power supply	600 W	80 W
	(10 mN x 60 W/mN)	(8 operating thrusters)

A.4. Recommended propulsion system

It is clear from the previous analyses that proportional cold gas thrusters are not suitable for baseline monitoring, since they would imply an excessive fuel (nitrogen assumed) consumption.

One-stage vs. two-stage propulsion

As opposed to proportional cold gas thrusters, the fuel consumption of FEEP thrusters is almost negligible, but the available thrust level is strongly limited by the power demand, resulting in an availability of the interferometer limited to 73 % (about 6.5 hours of maneuver each day to reconfigure the baseline). If this operational constraint is found excessive, the interferometer availability can be improved by the implementation of additional thrusters which achieve a better balance between fuel and power consumption. The best candidate propulsion systems have been identified in the frame of the analyses for drag-free missions on LEO (Low Earth Orbits):

- thermal arcjets, i.e. hydrazine thrusters with propellant pre-heating to increase the thrust efficiency
- low specific impulse ion thrusters, developed in Russia for station-keeping on very low altitude orbits

These thrusters are far from being accurate enough for the operational mode, but can be used in complement to FEEPs to reduce the maneuver duration. The potential gain allowed by these technology is evaluated in table A.4. This table demonstrates that the increase of the available thrust results in an augmentation of the impulse to be applied to the telescope spacecraft, (faster maneuvers). When cumulated with the associated reduction of the specific impulse, this results in a rapidly increasing fuel consumption. Therefore, only the low specific impulse ion propulsion can significantly increase the interferometer availability with a reasonable augmentation of the fuel consumption. It must

be noted that at least three additional ion thrusters must be implemented to perform the baseline monitoring, the fine thrusters being in charge of correcting the thrust errors (especially in direction). Therefore, the system cost of a two stage actuation system is not negligible both in terms of mass and complexity (additional tanks, pipes and power conditioning units, ...). For this reason, a two-stage system is not baselined, since the availability of the interferometer allowed by FEEP thrusters alone seems satisfactory. Therefore, FEEP thrusters are proposed as baseline propulsion system for both baseline monitoring and fine operational control of the free-flyer interferometer.

Table A.4. Fuel consumption comparison

	FEEP	Ion thrusters	Thermal arcjets
Efficiency (specific impulse)	6000 sec	1700 sec	500 sec
Power consumption	60 W/mN	15 W/mN	5 W/mN
Thrust range (1 unit)	0.001 to 1 mN	40 to 80 mN	100 to 400 mN
Available thrust authority for 600 W	10 mN	40 mN	120 mN
Daily maneuver duration	5 h 30	1 h 25	0 h 32
Interferometer availability	78 %	94 %	98 %
Required daily impulse	192 N.sec	203 N.sec	235 N.sec
Fuel consumption (4 years)	4.5 kg	18 kg	70 kg

Thruster configuration

As already pointed out, the FEEP thrusters must be implemented in clusters to achieve the required 10 mN thrust (current prototypes deliver about 1 mN full thrust). It is also possible to implement in each cluster FEEP units with different thrust rating:

- micro-thrusters (1 μ N max. thrust typically) similar to those foreseen for LISA to realize the accurate positioning during the measurements
- mini-thrusters (1 mN max. thrust typically) to realize the orbit maintenance and the interferometer reconfiguration maneuvers.

The minimum number of thrusters (or more precisely the number of clusters of thrusters with the same orientation) is 6 in order to control the 6 DOFs of the satellite. In order to achieve a full redundancy and provide a simple and efficient failure isolation, two redundant branches of 6 thrusters are generally considered. The proposed implementation is therefore to have the FEEP thrusters arranged in six clusters incorporating a redundant branch. The position and orientation of the clusters can be optimized according to the desired spatial distribution of the control authority using the algorithms developed for drag-free missions, taking into account the implementation constraints on the satellite. An a priori thruster configuration is to have three clusters at the edge of the solar array to have a large torque authority for the acquisition (despin phase). In order to be able to generate pure forces, the other three clusters must be implemented on the opposite side of the S/C, with the constraint to avoid plume impingement on the telescope optics.

References

- Ciucci, A., G. Genuini, M. Andrenucci, Experimental investigation of field emission electrostatic thrusters AIAA 22nd International Electric Propulsion Conf, IEPC 91-103, 1991

Andrenucci M., S. Marcuccio, L. Spagli, A. Genovese, Experimental study of FEEP emitter starting characteristics, AIAA 22nd International Electric Propulsion Conf, IEPC 91-104, 1991

Gonzales J., G Saccoccia, H. von Rohden, Field emission electric propulsion: experimental investigations on microthrust FEEP thrusters, AIAA 23rd International Electric Propulsion Conf, IEPC 93-157, 1993

Appendix B

PARAMETRIC COST STUDY

We have studied the cost of the mission as a function of the number of telescopes in order to determine the optimal configuration for accomplishing the reference science program.

We have used the parametric cost estimation process developed by the US Air Force (Fong, 1981, Larson and Wertz, 1992). In this model, the spacecraft subsystem estimates are weight-based, and the payload estimates are a function of the aperture.

The USAF cost model for payloads is based on a complete system including focal plane instrumentation. We have assumed a cost of a reference 1 meter diameter telescope to be 100 MECU, of which 50 MECU is for the Research and Development Test and Evaluation (RDT&E) phase, and 50 MECU is production cost. According to the USAF model, these two cost components vary as the 0.562 power of the aperture diameter.

In the model, spacecraft bus cost is based on mass and is equal to $16 + 0.110 m_{sc}$ MECU for the RDT&E phase and $0.185 \times m_{sc}^{0.77}$ MECU for the production of a single unit. The mass of the telescope unit s/c bus has been estimated at 250 kg in the case of the 1 meter telescope payload. Half of the mass is assumed to be a function of the supported telescope mass which approximately varies as the square of the aperture. The mass of the spacecraft bus can then be estimated as $m_{sc} = 250(0.5 + 0.5 \times d^2)$, where d is the telescope aperture diameter.

Production cost reduction for multiple units is modeled as the 0.926 power of the number of units when the number of units is less than 10.

The cost of n telescopes of diameter d (in meters) is therefore:

$$\text{Cost}_{tel} = 50 d^{0.562} + 16 + 0.11 \times m_{sc} + (50 d^{0.562} + 0.185 m_{sc}^{0.77}) \times n^{0.926}.$$

Assuming the cost of the recombining hub and spacecraft bus to be about 200 MECU for a 6 telescope feed, with half of this cost varying linearly with the number of apertures, the cost of the hub is therefore

$$\text{Cost}_{hub} = 200 (0.5 + 0.5 \frac{n}{6}).$$

Finally, we have based the launch cost on the Ariane 5E launcher. To the first order, the main constraint is mass and not volume. The mass of a 1 meter telescope payload has been estimated at 300 kg and can be assumed to vary as the square of the diameter. The mass of the telescope unit is thus:

$$m_{tel} = m_{sc} + 300 \times d^2$$

We estimate the mass of the hub to be

$$m_{hub} = 200. + 200 \times (n/6)$$

The number of Ariane 5 launches is calculated on the basis of 4400 kg of total payload mass per launch (5200 kg total capability less 800 kg for the transfer stage).

The results of this parametric study are shown in section 6.2. Although, this parametric study was done only for the free-flyer version, results for the moon version are expected to be similar.

References

- Fong, F. et al, *Space Division unmanned cost model*, El Segundo, CA: USAF Space Division, Directorate of Cost Analysis, 1981
- Larson W. and J. Wertz, *Space Mission analysis and design*, Kluwer, 1992.

Appendix C

FREE-FLYER APPLICATION TO EARTH-LIKE PLANET DETECTION

One of the most exciting fields of study in astronomy is the search for extrasolar planets, especially earth-like planets. Any detection would be of major importance for the confirmation of current theories of planet formation and would, of course, be of tremendous philosophical interest. Indirect detection through orbital perturbations have been recently reported for Jupiter-sized planets, but is very unlikely for the much lighter earth-like planets. Direct imaging presents extraordinary challenges because of the required resolution and the faintness of planets compared to their stars.

An alternate solution consists of detecting planets by their thermal emission rather than their reflected light. Although zodiacal radiation background is more prominent than planet flux, the ratio of the star's flux to the planet's is reduced from 10^{10} in the visible to 10^6 at around the planet's flux peak, i.e. $10\text{ }\mu\text{m}$ for earth-like planets, thus facilitating the difficult task of overcoming parent star glare (Fig. C-1). The longer wavelength also makes it much easier to avoid scatter from the microroughness of the optics. An additional advantage of working in the near infrared is that low resolution spectroscopy of the detected planets' atmospheres can be performed in search of CO_2 , water vapor and ozone. Ozone is believed to be a good tracer of the presence of free oxygen, and hence possibly of biological activity on the planet.

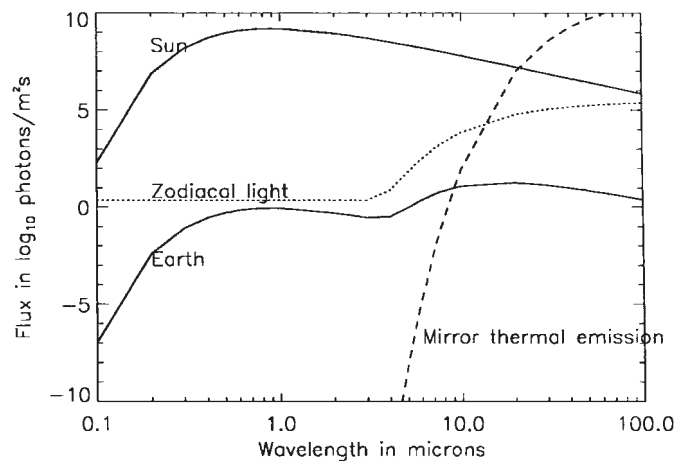


Fig. C-1. Flux of the sun and earth at a distance of 12 parsecs. The bandpass is taken as 20%. The earth's reflected sunlight is computed assuming an albedo of 0.4 and a phase function of 0.25. The earth's thermal radiation is based on a temperature of 300°K and an emissivity of 1. Also shown is the background flux due to the thermal emission of the optics at 70K .

This approach was first proposed by Bracewell (Bracewell 1978, Bracewell and Mac Phie 1979) and further studied by NASA Ames (NASA 1979), and several authors including Angel (1986, 1995), Shao (1989), and A. Léger who proposed a specific mission concept to ESA under the name of *Darwin* (Léger

1994). Very recently a NASA sponsored study performed by a large team of investigators lead by JPL concurred with the soundness and attractiveness of the approach (Elachi 1995).

Detailed technical solutions for this challenging problem are still very much in a state of flux, but a few basic principles have clearly emerged:

- Detection is best accomplished by using a rotating interferometer. With an interferometer, the wavefronts issuing from the individual sub-apertures can be combined out of phase in order to null out the on-axis flux of the parent star but not that of off-axis sources such as potential planets (Bracewell and Mac Phie 1979). Detection is accomplished by rotating the interferometer around its axis, which modulates the planetary signal.
- The influence of thermal emission of the zodiacal cloud around our sun depends on the size of the individual sub-apertures, but is typically prohibitive unless very large apertures are used. This background can be rendered negligible by placing the interferometer at a distance of 3 to 5 astronomical units from the sun (Bracewell 79, Léger 93). Gravity assists using Venus and Earth flybys can be used to place the spacecraft in a 1 x 5 AU heliocentric elliptical orbit.
- Thermal emission of the telescope optics can be made negligible by cooling all optics to below 60 degree Kelvin. This is relatively easy to achieve passively by proper shielding from the sun and insulation of the internal heat sources.
- The planetary signal may be impossible to distinguish from that of the zodiacal light in the planetary system under investigation. This would be the case especially if the zodiacal disk is much brighter than that of our solar system or is seen edge on or very inclined. Discrimination of the planetary signal from that of the exo-zodiacal disk is best achieved by using an uneven number of sub-apertures in order to prevent the modulation of the exo-zodiacal disk from mimicking that of a planet (Mariotti 1995).
- Nulling interferometric systems have the inconvenience of being sensitive only to sources at those field angles which are near the fringe pattern maxima. An interferometer with a fixed baseline will therefore be blind to all planetary systems where the planet-star angle does not fall on these fringe maxima. This can be alleviated by working at a different wavelength, but detected systems could not then be investigated spectroscopically. Another solution is to use an elliptic array, but this is at the expense of efficiency. The right solution is a variable baseline interferometer.

It is for this last problem that the free-flyer offers a unique and very attractive solution. The baseline of near infrared interferometers for exoplanet search need to be several tens of meters long, typically 30 to 100 meters. A variable baseline can in principle be obtained with a "connected" structure using tiltable optics or extendable arms. But these are very awkward solutions. Tiltable optics require substantial mechanisms to continuously repoint the sub aperture telescopes as the array rotates. Continuously moving delay lines are also needed to compensate for the optical path difference during rotation. Expanding and contracting booms have been proposed, but are intrinsically weak structures for the long lengths required, so the relatively massive telescopes located at their extremities would require their own attitude and position controls.

A free-flying cluster offers a clean solution (Fig. C-2). The baseline can be adjusted at will with essentially no limit. There are no moving parts or deployable mechanisms prone to failure. There are no structure vibrations

or control/structure interactions to mar the stability of the interferometric elements. Failed individual spacecraft in the cluster can be replaced by a redundant unit parked nearby or by sending a backup spacecraft.

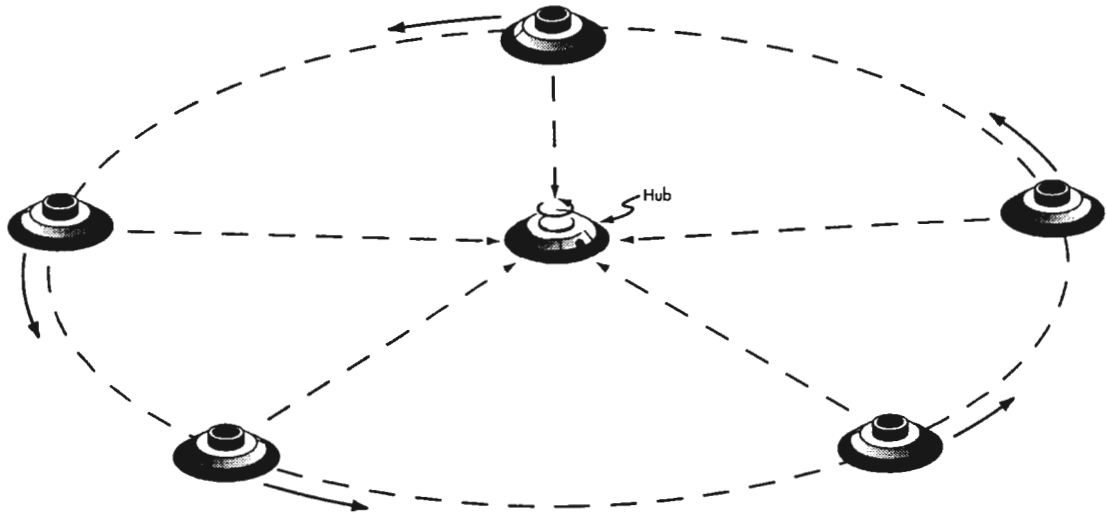


Fig. C-2. Artist's view of a 5-element nulling interferometer for the detection and spectroscopic analysis of exo-planets. Compared to connected structure systems, the free-flying cluster offers the possibility of tuning the baseline length to maximize the planet's flux at any wavelength. This is a key advantage for the spectral analysis of the planetary atmosphere.

Although not a-priori desirable because of the need to compensate the centrifugal force, rotating a free-flyer cluster at sufficiently low speed is certainly feasible thanks to the high specific impulse of FEEPs actuators. A 600 kg telescope unit spacecraft orbiting the hub on a 25 meter radius at 1 turn per 40 hours (i.e. 4 hours to cover a $1/10^{th}$ turn intrafringe) would require only $40 \mu N$ to counterbalance the centrifugal force. This would represent a consumption of less than 0.1 kg of Caesium over a 5 year mission. Alternate ways of examining the Fourier plane other than by rotation could also be explored.

A nulling interferometer composed of five 1.5 meter telescopes with baselines varying from 10 to 40 meters would permit the detection of terrestrial exo-planets around all non binary F, G and K stars within 20 parsecs of the sun. This represents a sample of about 400 stars. A computer simulation of the type of observation possible is shown in Fig. C-3. Thanks to the variable baseline, low resolution spectroscopy of the detected planet atmospheres could be optimally performed.

Launching and operating a free-flying cluster at more than 3 AU with the attendant power and communication problems is certainly a challenge. But the "connected" truss or inflatable schemes proposed so far may be no less challenging. The free-flyer scheme with its intrinsic advantages certainly merits consideration and should be studied further.

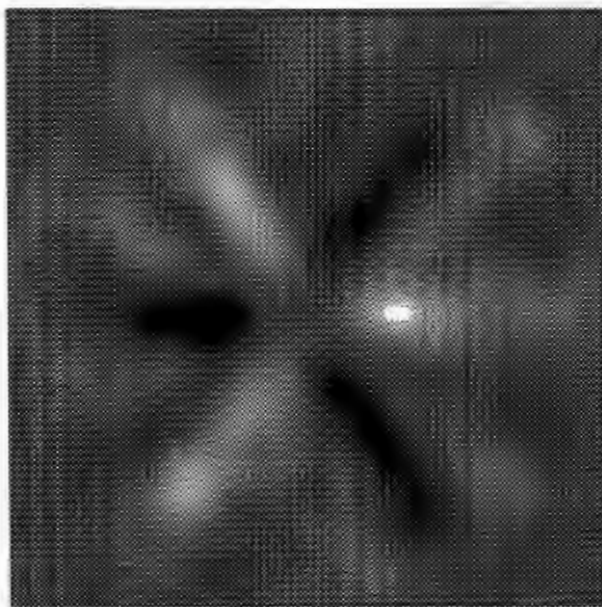


Fig. C-3 Image recovery of simulated Venus, Earth and Mars orbiting a sun-like star located at 10pc, as obtained with an elliptical array of five 1.5m class telescopes in a 30 hour integration. The reconstructed planets are the bright spots. The black and white pattern is an artifact of the image reconstruction process (B. Mennesson and J.M. Mariotti, 1995).

References

- Angel J.R.P., A.Y.S. Cheng, and N.J. Woolf, A space telescope for infrared spectroscopy of earth-like planets, *Nature*, Vol 322, 341, 1986.
- Angel R. and N. Woolf, 1995, OASES - JPL Roadmap study report
- Bracewell R., Detecting nonsolar planets by spinning infrared interferometer, *Nature*, 274:780, 1978.
- Bracewell R. and R. Mac Phie, 1979, *Icarus* 38, 136
- Elachi C., 1995, EXNPS Roadmap study report, JPL (to be published)
- Leger A. 1994, Darwin Proposal to ESA 2000
- NASA - Systems level feasibility study for the detection of extra-solar planets, *NASA-Ames Technical Report LMSC-D676424*, Lockheed Palo Alto Lab, June 1979.
- Mariotti J.M., 1995, EXNPS Roadmap JPL internal study report.
- Mennesson B. and J.M. Mariotti, 1995, (to be published)
- Shao M., Direct IR interferometric detection of extra solar planets *Proc. of a NASA/STScI Workshop on the Next Generation Space Telescope*, Baltimore, 1989.

Appendix D

STUDY PARTICIPANTS

Pierre Y. Bély

Space Telescope Science Institute
3700 San Martin Drive
Baltimore, MD 21218, USA
Tel: 410 338 4780
Fax: 410 338 1592
e-mail: bely@stsci.edu

Bertrand Calvel

Matra Marconi Space
ZI du Palays
rue des Cosmonautes
31077 Toulouse Cedex
Tel: (33) 61 39 63 83
Fax: (33) 62 24 77 85
e-mail: calvel-bertrand@
mms.matra-espace.fr

Alan Greenaway

Defence Research Agency
St Andrews Rd
Great Malvern WR14 3PS
United Kingdom
e-mail:
AHG%CCF.dnet@hermes.dra.hmg.gb
Phone: (44) 1 684 89 53 90
Fax: (44) 1 684 89 44 98

Chris Haniff

Cavendish Laboratory
Madingley Road
Cambridge CB3 0HE
England
Tel: (44) 1223 33 73 63
Fax: (44) 1223 354599
e-mail: cah@mrao.cam.ac.uk

Herve Lambert

Matra Marconi Space
ZI du Palays
rue des Cosmonautes
31077 Toulouse Cedex
Tel: (33) 62 24 79 61
Fax: (33) 62 24 79 60
e-mail: lambert-@mms.matra-espace.fr

Mario G. Lattanzi

Osservatorio Astronomico di Torino
Strada Osservatorio 20
10025 Pino Torinese
Torino, Italy
Tel: (39) 11 4619023
Fax (39) 11 461 9030
email: lattanzi@otoax2.to.astro.it

Robin Laurance

Future Science Projects Office
ESA/ESTEC
Postbus 299
2200 AG Noordwijk zh
The Netherlands
Tel: (31) 7165 3516
FAX: (31) 7165 5417
e-mail: RLAURANC@estec.esa.nl

Jean-Marie Mariotti

Observatoire de Paris-Meudon
92195 Meudon
France
Tel: (33) 1 45 07 75 46
Fax: (33) 1 45 07 28 06
e-mail: mariotti@obspm.fr

Jan E. Noordam

National Foundation for
Research in Astronomy
Postbus 2
7990 AA Dwingeloo
The Netherlands
Phone: (31)-5219-7244
FAX: (31)-5219-7332
e-mail: noordam@nfra.nl

Richard Scaddan

Matra Marconi Space Systems Ltd
FPC 320
PO Box 16
Filton
Bristol UK BS12 7YB
Tel: (44) 117 900 6467
Fax: (44) 117 900 6849

Farrokh Vakili

Observatoire de la Côte d'Azur
2130 Route de l'Observatoire
Caussols
06460 Saint Vallier de Thiey
France
Tel: (33) 93 40 54 91
Fax: (33) 93 40 44 31
e-mail: vakili@rossini.obs-nice.fr

Paul Vangasse

Matra Marconi Space Systems Ltd
FPC 320
PO Box 16
Filton
Bristol UK BS12 7YB
Tel: (44) 117 900 6455
Fax: (44) 117 900 6849

Sergio Volonte

ESA Headquarters
8 rue Mario Nikkis
75738 Paris Cedex 15
France
Tel: (33) 1 53 69 71 03
FAX: (33) 1 53 69 72 36
e-mail: svolonte@esa.bitnet

Oskar von der Lühe

European Southern Observatory
Karl Schwarzschild Strasse 2
85748 Garching bei Munchen
Germany
Tel: (49) 89 320 06519
Fax: (49) 89 320 2362
e-mail: ovdluhe@eso.org